Nonreciprocal Acoustic Metamaterials based on Time-Varying Media

Sheng Wan

To cite this version:

Sheng Wan. Nonreciprocal Acoustic Metamaterials based on Time-Varying Media. Physics [physics]. Université de Lorraine, 2022. English. NNT : 2022LORR0230 . tel-04127655

HAL Id: tel-04127655
https://hal.univ-lorraine.fr/tel-04127655

Submitted on 14 Jun 2023

HAL is a multi-disciplinary open access archive for the deposit and dissemination of scientific research documents, whether they are published or not. The documents may come from teaching and research institutions in France or abroad, or from public or private research centers.

L'archive ouverte pluridisciplinaire **HAL**, est destinée au dépôt et à la diffusion de documents scientifiques de niveau recherche, publiés ou non, émanant des établissements d'enseignement et de recherche français ou étrangers, des laboratoires publics ou privés.

UNIVERSITÉ DE LORRAINE | BIBLIOTHÈQUES UNIVERSITAIRES

AVERTISSEMENT

Ce document est le fruit d'un long travail approuvé par le jury de soutenance et mis à disposition de l'ensemble de la communauté universitaire élargie.

Il est soumis à la propriété intellectuelle de l'auteur. Ceci implique une obligation de citation et de référencement lors de l'utilisation de ce document.

D'autre part, toute contrefaçon, plagiat, reproduction illicite encourt une poursuite pénale.

Contact bibliothèque : ddoc-theses-contact@univ-lorraine.fr
(Cette adresse ne permet pas de contacter les auteurs)

LIENS

Code de la Propriété Intellectuelle. articles L 122. 4
Code de la Propriété Intellectuelle. articles L 335.2- L 335.10
http://www.cfcopies.com/V2/leg/leg_droi.php
http://www.culture.gouv.fr/culture/infos-pratiques/droits/protection.htm

Doctoral School: **Chemistry-Mechanics-Materials-Physics**
University Department: **Institut Jean Lamour**

Thesis defended by **Sheng Wan**
in **12th December 2022**
In order to become Doctor from Université de Lorraine
Academic field: **Physics**

Nonreciprocal Acoustic Metamaterials based on Time-Varying Media

Committee Members

Referees

Prof. Abdelkrim Khelif	Directeur de Recherche CNRS, Université de Franche-Comté
Prof. Vincent Tournat	Directeur de Recherche, Le Mans Université

Examiners

Prof. Bahram Djafari-Rouhani	Professeur Emérite, Université de Lille *(Président du jury)*
Dr. Julia Mainka	Maitre de Conférences, Université de Lorraine

Supervisors

Prof. Badreddine Assouar	Directeur de Recherche CNRS, Université de Lorraine
Dr. Mourad Oudich	Maitre de Conférences, Université de Lorraine

Keywords: Acoustic and elastic metamaterials, Nonreciprocity, Time-varying medium.

Mots clés : Métamatériaux acoustiques, Nonreciprocité, Milieu variant dans le temps.

Contents

List of Figures

General introduction

The reciprocity principle in acoustics and elastodynamics establishes a relation of symmetry between the excitation and the response in fluids and solids. A comprehensive description of reciprocity is that after the source and the receiver being interchanged, the frequency response function between any two points remains unchanged, despite the existence of inhomogeneities and losses within the medium. For hundreds of years, reciprocity has always been considered acquiescent as a basic law in the study of classical wave phenomena. Recent progress in theoretical research and the advance in fabrication techniques have prompted us to consider reciprocity in a new perspective: broken reciprocity could enable new possibilities for wave manipulation. Guided by such perception, researchers designed and fabricated practical devices with unprecedented directional wave control. For example, a device that let the wave travels through in one direction with large transmission coefficient while it blocks backscattered waves, namely, the isolator, was designed to protect sources from backscattering. Further, bulk structures that are internally insulating medias but where wave can propagate unidirectionally at the boundaries where constructed, namely, acoustic topological insulators.

Nonlinear media, which irreversibly generates harmonics, used to be a popular way to break reciprocity. However, knowing that the mechanism breaking reciprocity using nonlinear materials largely depends on the input intensity, some limitations lie on nonlinear nonreciprocal systems: once the nonlinear state in the system is enabled by an intensive input, small waves can travel through the system in all directions. In the last decade, the interest on nonreciprocity has been directed to the time-varying media, including kinetic media and spatiotemporally modulated media (STM). Kinetic media is media with moving parts or with circulating flows, and STM media have their mechanical properties vary both in space and time. Researchers have observed that the frequency shift found in the Doppler effect is fundamentally nonreciprocal. In a typical scenario of Doppler effect, a source communicates to a receiver through a moving barrier. In such scenario that contradicts reciprocity, the Doppler frequency shift changes it sign when the source and receiver are interchanged. Therefore, the reciprocity is expected to fail in waveguides with air flow or ring resonators with circulating fluid-flow, all of which breaks the time-reversal symmetry. When looking at the kinetic media, researchers have observed an asymmetry dispersion diagram in a spatially periodic structures with a uniform moving velocity. That is to say, the relationship between the frequency and the wave number is not the same in the propagation directions along or against the media motion. So, the STM, which share the similar behavior with the moving spatially periodic structures, are expected to break time-symmetry symmetry and lead to nonreciprocity. However, since STM is actually stationary while the moving spatially periodic structures is not, their differences root in the governing equations and appear on their dispersion diagrams. The main subject of this doctoral study is specifically centered on nonreciprocity in acoustics using time-varying media.

It should be mentioned that time reversibility and reciprocity are not completely equivalent, although they are physically similar at a certain level. Typical time-irreversible mechanisms include both external biasing such as time-varying media and energy-dissipation effects such as viscosity and friction. Both external biasing and energy-dissipation effects fail time reversibility, but physically in different ways. Particularly, reciprocity is kept with viscous damping in linear acoustics.

With the rapid advance of computing capabilities in recent years, numerical approaches were constructed and widely adopted in the analysis of nonreciprocal system with time-varying media, namely, finite element method (FEM) and finite-difference time-domain method (FDTD). Semi-analytical approaches were equally developed in need of rapid parameter tuning and physical exploitation, including the temporal coupled-mode theory (TCMT), the transfer matrix method (TMM) and the quadratic eigenvalue problem (QEP) solving, covering various application scenarios. These analytical approaches solve the time-invariant quantities, while in presence of time-varying parameters in nonreciprocal system, Fourier decomposition and perturbation method are widely utilized as internal methods to solve the problem with time-variant perturbations.

The aim of the present doctoral project is to introduce a new family of compact nonreciprocal devices in acoustics and elastodynamics. As we will show throughout the chapters of this manuscript, we were able to design and build a cascaded time-modulated Fabry-Perot (FP) air resonator system, a time-modulated mechanical bi-resonators system, and an acoustic multifunctional meta-lens using air flow, all of which display non-reciprocal wave manifestations. TMM and FEM are utilized for analytical and numerical demonstrations in this doctoral project. An experimental realization was successfully conducted using active resonators that combine coupled magnets and electromagnetic to control their effective stiffness in time.

This present manuscript is organized in five chapters. The state of the art and literature review on serval methods to break reciprocity are provided in Chapter1. Chapter 2 presents a description of the numerical and analytical approaches developed and utilized to solve acoustic equations with time-varying parameters to study nonreciprocal systems. Particularly, detailed descriptions are made for TCMT, TMM and QEP, involving Fourier decomposition, with the corresponding application scenarios. The design and demonstrations of our time-varying nonreciprocal systems are the subject of three chapters, i.e., Chapter 3, Chapter 4 and Chapter 5. A theoretical demonstration of acoustic nonreciprocity via cascaded time-modulated FP resonators is introduced in Chapter 3. An experimental realization of elastic flexural wave nonreciprocity via cascaded time-modulated bi-resonator system is introduced in Chapter 4, with a physical realization based on coupling between magnets and well-tailored electromagnets. More specifically, the design of these two structures profits from the coupling between the resonators and the FP resonance created between the two resonators. In Chapter 5, we provide a new approach using air flow to bring in nonreciprocal multifunctional meta-lens with a numerical demonstration. We split a sound waveguide into multiple channels, and directionally manipulate the phases of each channel to achieve nonreciprocal metasurface with unidirectional focusing. Finally, the designs and results on acoustic nonreciprocal device based on time-varying media are reviewed and summarized, and related perspectives are discussed with an outlook on future research and applications.

Chapter 1

Nonreciprocal acoustics: State of the art

Contents

I. Reciprocity in wave propagation

The reciprocity theorem is a fundamental principle in classical waves which states that the relationship between a source in one position and the response in another position is symmetric when the source and measurement positions are interchanged.

The reciprocity theorem finds its roots in the theory of elasticity of solid materials in 19th century, which emanated from the work of Hermann von Helmholtz[1], Horace Lamb[2], Alfred Clebsch[3], James Clerk Maxwell[4], Enrico Betti[5], and Lord Rayleigh[6]. Helmholtz first dealt with it on sound in tubes[1]. In the study of rod systems, Clebsch noted that the dynamical matrix relating nodal displacements to external loads is generally transpose symmetric[3]. The above property was later formulated as a naive statement of reciprocity by Maxwell[4], considering four arbitrary points (B, C, D, E) in a continuous medium:

> “The extension in BC, due to unity of tension along DE, is always equal to the tension in DE due to unity of tension in BC.”

In 1872, Betti generalized the concept of reciprocity to static distributed loads on elastic body[5]. In 1878, Rayleigh stated and proved the following reciprocal theorem[6]:

> “On his extension of Green’s theorem Helmholtz founds his proof of the important theorem contained in the following statement:
>
> If in a space filled with air, which is partly bounded by finitely extended fixed bodies and is partly unbounded, sound waves be excited at any point A, the resulting velocity potential at a second point B is the same both in magnitude and phase, as it would have been at A, had B been the source of sound.”

Lord Rayleigh stated the reciprocal theorem also in the language of circuit theory. Being developed through early stages, this theorem was generalized to optics[7,8] and electromagnetism[9] (known as Lorentz reciprocity). In 2003, Jan D. Achenbach revealed a specific mathematical formulation of reciprocity[10] in elastodynamics. An accurate definition is simultaneously given in his literature:

> "A reciprocity theorem relates, in a specific manner, two admissible elastodynamics states that can occur in the same time-invariant linearly elastic body. Each of two states can be associated with its own set of time-invariant material parameters and its own set of loading conditions. The domain to which the reciprocity theorem applies may be bounder or unbounded."

Reciprocity is a powerful tool during analyzing, designing, and operating acoustic systems. Reciprocity being obeyed in a system implies that underlying symmetric relationship between bi-directional propagations of waves exists, which is fundamental for many sensing technologies such as b-Scan ultrasound diagnostic and calibration of microphones. Reciprocity can also simplify the analysis of complicated scenarios. A complex measurement of an acoustic system quantity can in many cases be replaced by a simpler one when reciprocity holds. For example, in the acoustic calibration of a multimedia room, the positioning and orienting of the speakers are expected to satisfy a comfortable sound lecture for the audience. Instead of adjusting the positioning and orientation of the speakers then measure the acoustic field around the audience seat, a monopole source can simply be placed at the audience seat. One can just measure the acoustic field around desired position then decide the positioning and orientation of speakers according to the yielding of the acoustic field. For many years, reciprocity has served as a useful concept for derive analytical solutions for diffusion in the presence of a fault and for the estimation of inverse parameters in seismic experiments[11,12].

II. Nonreciprocity in acoustics and elastodynamics

Nonreciprocity enables novel wave guiding phenomena and finds application not only in communication systems[13], but it is also being adopted to explore other phenomena, among which switching and rectification[14], parametric amplification[15], breather arrest and localization[16], mode conversion[17], topological edge-to-edge pumping[18], etc., which are found in all typical acoustic wave domains: air-borne[19], water-borne[20], biological tissues[21], and solids[22,23].

As for nonreciprocity itself, it is frequently associated with the realization of acoustic diodes, unidirectional wave propagations and asymmetrical wave control, though these concepts are sometimes mixed up. Nevertheless, as those kinds of device share functionalities that may appear similar, all of them worth being discussed and categorized here.

From the perspective of physical mechanism, the acoustic devices performing non-identical sound transmissions in opposite directions can be graded into serval categories. The first one is the acoustic diode. According to the fundamental definition of a "diode", at a specific frequency, an acoustic isolator must enable high transmission in one direction while blocks the backscattered waves. Such performance can be reached by structures with active elements at a single operating frequency because these active elements usually induce irreversible frequency conversion (nonlinear medium)[20,24], splitting effect (acoustic circulator)[19], etc., which leads to energy transfer into higher order modes. Additionally, the acoustic circulator is considered "acoustic isolator", a further branch of acoustic diode, which enables high transmission in one direction while blocks the backscattered waves. The second working category is the passive linear asymmetric structure such as the one presented[25] in **Fig. 1.2** where the design of the structure is based on a geometrical asymmetry along the direction of propagation to alter the shape of the wave. In this configuration, the time-reversal symmetry is conserved, and the structure is reciprocal. The third category are non-reciprocal systems based on breaking the time reversal symmetry using well designed active elements. At this level, the wave properties are found to be different when the source and the response positions are interchanged, and non-reciprocity theorem is thus satisfied. The difference may lies on the wave amplitude of a specific propagation mode (at a specific frequency), or on the wave phase which is key to enable directional sound shaping[26]. Non-reciprocal acoustic devices realized by space-time modulation of the effective properties of the medium also fall into this category.

Acoustic devices with non-identical transmissions in opposite directions, either non-reciprocal or with an asymmetric design, can enable unidirectional propagation (acoustic diode-like functionality) or non-identical wave transformation. The unidirectionality is satisfied if different waves are observed in different propagation directions for an identical source at corresponding positions. However, further than unidirectionality, nonreciprocity is achieved when "*different output waves are observed when the input port and the output port are interchanged*". As for the time-reversal asymmetry, it requires that if the time is reversed for wave propagation, with the clockwise response acoustic field as incidence in counterclockwise propagation, a different response can be observed from the incidence in clockwise propagation, as explained in **Fig. 1.1** (it should be noted that the counterclockwise time sequence is different from inverse entropy). In most passive systems, since the systems are time-invariant, this time-reversal process can be simply considered as applying the reflection and transmission field as the new incidence. Interestingly, in some nonlinear systems, since specific mechanism in nonlinear medium such as frequency conversion is irreversible[27], the time-reversal symmetry is actually broken, regardless of the system being passive.

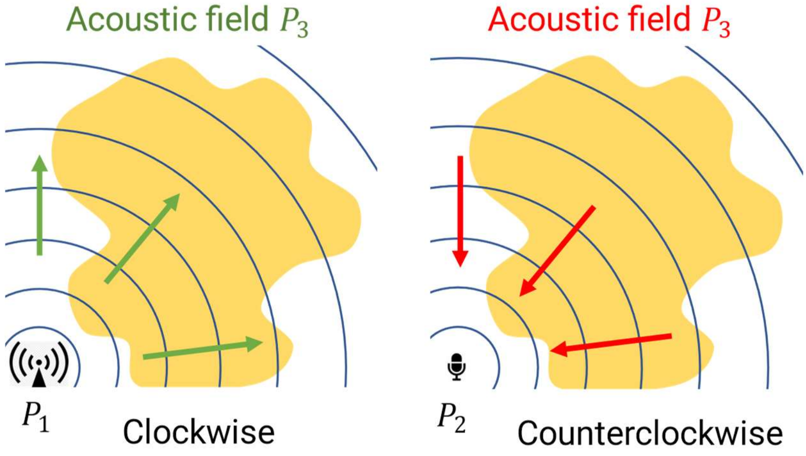

FIG. 1.1. Schematic of time-reversal wave propagation. In clockwise propagation, with an incident P_1, a corresponding response field P_3 can be measured at a further distance from the source, including the transmission and reflections. In counterclockwise propagation, with the same excited acoustic field P_3, a response P_2 can be measured at the source position in clockwise propagation. Time-reversal symmetry is broken in case where P_1 is different from P_2.

Generally, nonreciprocity tends to appear in the absence of linearity, passivity, or time invariance. The absence of the above elements leads to the utilization of nonlinear media, the moving media, the spatiotemporal modulation and the application of active Willis materials, which are several methods to break the nonreciprocity. Before getting into these methods, let us briefly first discuss the passive asymmetric structures while being reciprocal.

II.1. Acoustic wave transmission in linear passive asymmetric structures

The design of acoustic asymmetric passive structures combines wave inter-mode transitions, selective-mode filtering, and cavity resonance for strong wave-structure interactions[25], without integrating any active element. However, the functionalities of this structure highly rely on the normal wave incidence. Some of the devices include coupled phononic crystal[28–32], asymmetric acoustic gratings[33], asymmetric metasurface[34,35], bended waveguide coupled with phononic crystal[36], etc. As an example, let us take the acoustic device proposed by Zhu et al.[25], presented in **Fig. 1.2**. The structure is made of three periodic elements highlighted in different colors in **Fig. 1.2(a)**: an antisymmetric coiling conduit (blue) connecting a symmetric corrugated one (yellow) and periodic bars (light red) in both ends. The symmetric corrugation has a bandgap for waves with odd symmetry while the bars display bandgap for waves with even symmetry. The mechanism of the unidirectional wave propagation is based on the symmetry conversion of the acoustic mode combined with these bandgaps. When sending a plane wave (symmetric mode) from the left, it will pass through the first corrugation and then gets converted into odd waves to pass through the bars, while sending the same plane wave from the right side will have it stopped by the bandgap of the bars (**Fig.1.2(b)**). The transmission coefficient showed high pressure in the forward direction while the pressure is almost zero in the backward propagation (**Fig 1.2(c)**). This system uses mode conversion so that the waveform and pressure field distribution are not conserved in transmission for the forward direction: while the input is a planar wave, the output wave has an antisymmetric pressure distribution with respect to the horizontal plane. The time-reversal symmetry is not broken, and this can be verified by inversing the process in time. In fact, by sending the wave with odd symmetry from the right in the backward direction, it will in fact pass through and a symmetric wave will be measured in the left side. The system remain consequently reciprocal as the time reversal symmetry is conserved.

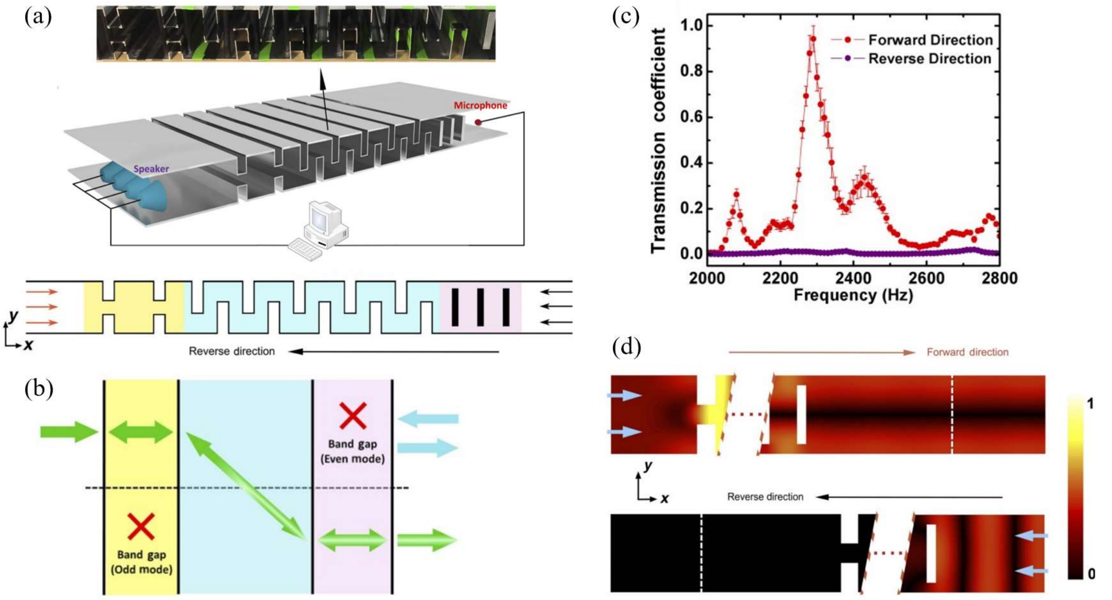

FIG. 1.2. (a) An acoustic asymmetric passive linear structure for uni-directional wave propagation made of three elements: symmetric corrugation (yellow). Coiled path (blue) and bars (light red). (b) The mechanism of one-way propagation based on mode conversion and bandgaps where in the forward direction, the plane wave with even symmetry pass through the first part, gets converted into odd mode in the second part, then pass through the bars with bandgap for even mode, while in the backward direction, the plane wave is stopped by the bars. (c) Transmission coefficient for forward and backward propagations. (d) Wavefield showing the diode functionality of the structure.

II.2. Nonlinearity for non-reciprocal acoustics

In elastic and acoustic media with time-invariant properties, the nonreciprocity is commonly achieved with material nonlinearity. Nonlinearity in acoustics can generate high order harmonics that are observed in time domain as distortions of the waveform, amplitude perturbation, nonlinear resonances, and bifurcation. Bifurcation is when a parameter of the system changes continuously to a certain critical value, so that the mechanical properties (for example, the stiffness) or the topological properties (for example, the Chern number) of the system will suddenly change[37,38]. In principle, strong nonlinear features in acoustics may be observed when the intensity is relatively high, and the effective material properties could vary with the amplitude, which can possibly be directional[39]. A schematic of the relation between the output intensity and the nonlinearity is shown in **Fig. 1.3**. As the output intensity grows, weak nonlinearity occurs; then once bypassing certain thresholds, bifurcation is enabled. The phenomenon could be directional or not. A typical example of nonlinear materials is rubber string, whose section area could change with varying strain forces, then the relationship between its deformation and strain force no longer obeys Hook's Law. However, since nonlinear materials do not always behave in nonreciprocal manner, spatial bias is a necessary ingredient to break nonreciprocity.

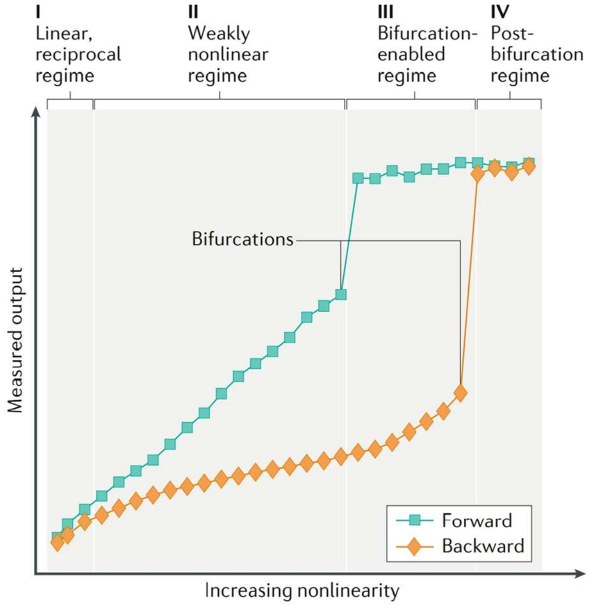

FIG. 1.3. The level of nonlinearity increases along the horizontal axis owing to an increase with the intensity. The monitored output (amplitude of motion) of the nonlinear medium is plotted on the vertical axis. Generally, four different response regimes exist for intensity-dependent nonlinear systems.[40]

The design of a nonlinear nonreciprocal structure usually begins with a spatially symmetrical system with mode-filtering functionality, combined with a nonlinear partition. The symmetrical partition lets waves in a certain frequency range pass in all propagation directions. In several works, these symmetrical partitions are phononic crystal[14,16,20,24,41–50] with bandgaps. Special cases exist such as the application of amplitude gap[39], which lets solitary waves with certain amplitudes pass.

Reciprocity in a nonlinear medium could be broken in various ways, including spatially varying the properties of materials [43–45], incorporating spatial asymmetry with irreversible and unidirectional energy transfer[27], exchanging the sequence of mode filtering and harmonic generation in different propagation directions via asymmetrically incorporating nonlinear defects or interfaces[16,20,24,46–48,50–54], or breaking the symmetry of the functional form of the nonlinear internal forces[40,55–57]. It is worth mentioning that it is possible to take advantage of the gravity as an asymmetrical element to break reciprocity by counteracting gravity with acoustic radiation pressure in the opposite direction to the gravitational acceleration[58]. An example is presented in **Fig. 1.4** where an air layer and a water layer are used in the system. The water layer in forward transmission undergoes nonlinear deformation which realizes direct contact with the aluminum wall and the wave is transmitted, while in the backward propagation, almost no wave is transmitted from aluminum to air because of the high impedance mismatch, and consequently unidirectional wave propagation is achieved.

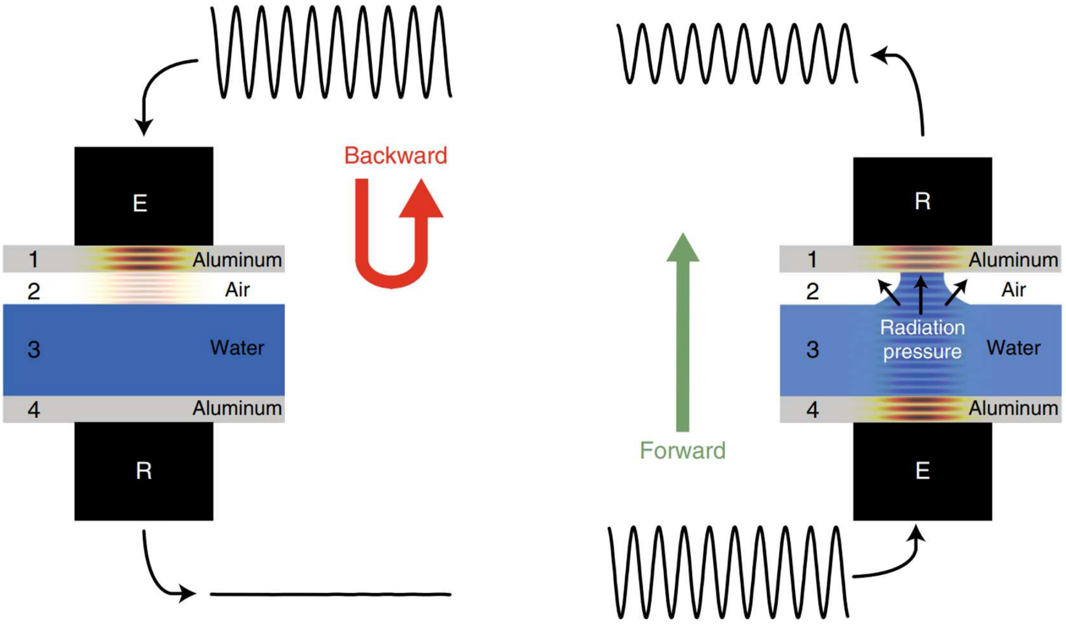

FIG. 1.4. An acoustic diode realized via nonlinear deformation of water[58]. E stands for emitter and R is for the receiver.

When waves travel though a nonlinear medium, super-harmonics or/and sub-harmonics are generated, depending on the nature of the nonlinearity and the incident frequency. With the source and response locations being interchanged, if different harmonics are observed, no matter if they are on the transmission side or the reflection side, reciprocity is broken. Liang et al.[20,24] coupled a nonlinear material to a linear periodic superlattice (**Fig. 1.5**) and tuned the operational frequency so that the incidence was within the superlattice bandgap while the corresponding harmonics fall into the superlattice pass band. By properly choosing the incident wave amplitude, a weak nonlinearity could be generated in the nonlinear medium which is an ultrasound contrast agent (UCA) microbubble suspension. If a harmonic wave is excited from the side of the nonlinear medium, harmonics are generated and travel through the superlattice layer to the other side because these harmonics fall in the passing band region (outside the bandgap) of the superlattice. However, if the wave is excited from the side of the superlattice at the frequency of the bandgap, it is prohibited from propagation in the superlattice, so it does not reach the nonlinear medium. Likewise, Boechler et al.[14] proposed a bifurcation-based solution (**Fig. 1.6**). In a statically compressed one-dimension granular chain, a light mass defect near a boundary is planted. As a result of the defect, at selected frequencies, a slight change of the incident amplitude near a threshold value can lead to a subsequent jump to quasiperiodic and chaotic states of vibrations, namely, typical bifurcations. Harmonic nonlinear modes are generated in the bifurcations, then the reciprocity is broken in similar way as in the work of B. Liang et al.[20,24]. However, this adopted methodology has the disadvantage that the frequencies of the transmitted waves correspond to those of the harmonics instead of the incident frequency. Improved solutions were proposed later. For example, Cui et al.[59] designed a structure whose bandgap is amplitude dependent owing to the nonlinear mechanism in the granular chain (**Fig. 1.7**). With a well-tuned incident amplitude which is below the cutoff passing amplitude, when exciting from the right side, the wave is filtered out before it reaches the left end; but when exciting from the left side at the conical rod (see **Fig. 1.7**), the amplitude gets amplified to surpass the cutoff passing amplitude so that the waves can travel through the granular chain. In this way, the transmitted wave have the same frequency as the incidence one.

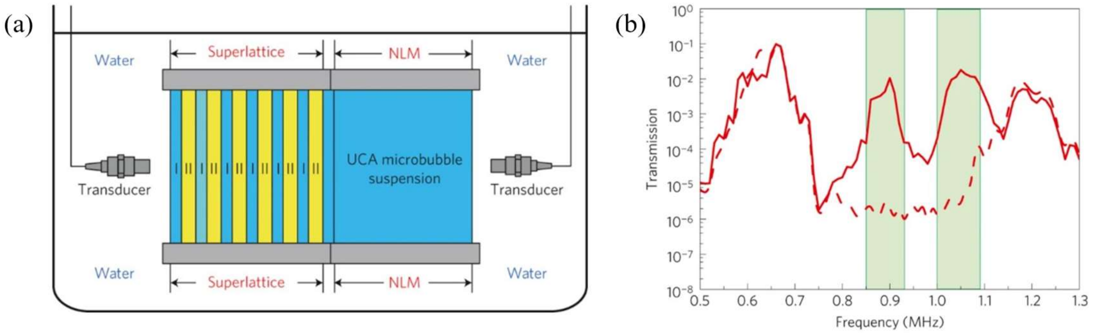

FIG. 1.5. An acoustic diode based on combining a phononic lattice and a non-linear media[20]. (a) Schematic of the experimental system and the cross-section configuration.

The superlattice is fabricated by alternately water layers (denoted as I) and glass layers (denoted as II) periodically. A layer of ultrasound contrast agent (UCA) microbubble suspension serves as the nonlinear material in this system. (b) Transmissions curves for propagations from right to left (solid line) and left to right (dashed line). The green regions denote two effective rectifying bands due to the frequency conversion effect of nonlinear material.

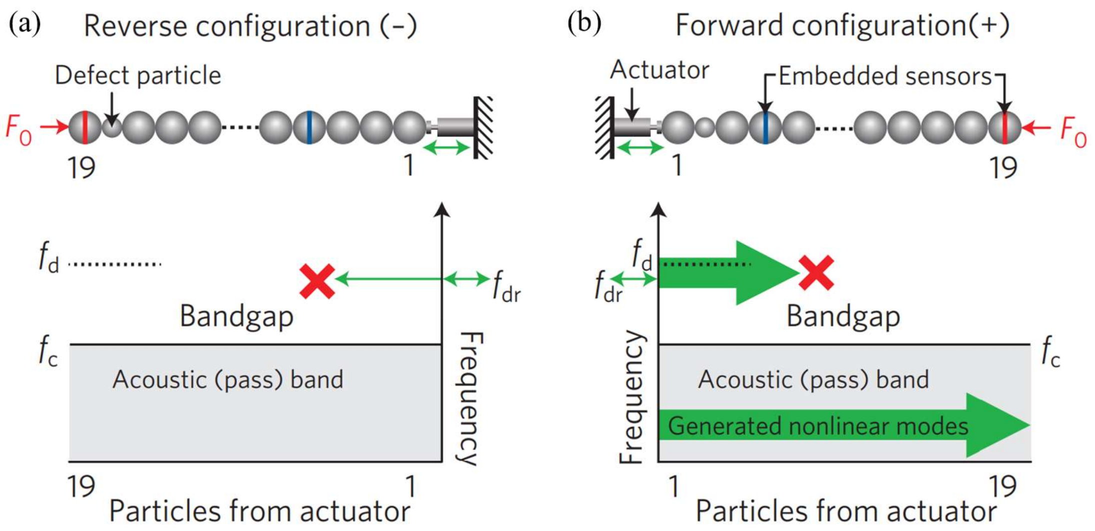

FIG. 1.6. A bifurcation-based acoustic switching and rectification device[14]. (a) Schematic of the rectification mechanism of the reverse-configured granular crystal composed of stainless-steel spherical particles, and a light mass defect. Static load F_0 is applied on the left boundary. f_d is the defect frequency, f_c is the pass band cutoff frequency and f_{dr} is the driving frequency. Incidence is from the left side via the actuator. (b) Schematic of the rectification mechanism of the forward-configured granular crystal. Static load F_0 is applied on the right boundary. Incidence is from the right side close to the defect particle.

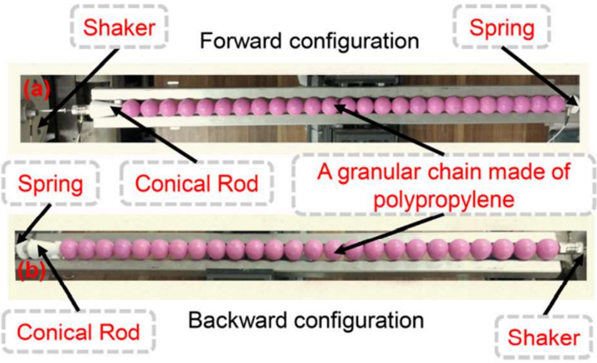

FIG. 1.7. Frequency-preserved non-reciprocal acoustic propagation in a granular chain[59]. The fabricated prototype is composed of a series of identical polypropylene beads (a symmetrical granular chain) and a conical rod. The conical rod serves as an amplitude amplifier in this structure.

Although applying nonlinearity is a practical way to passive nonreciprocity, it is worth stressing that nonlinearity-based nonreciprocal systems hold a limitation[40,60]. Shi et al.[60] reported that an optical nonlinear isolator cannot block a class of small-amplitude noise in the transmission-forbidden direction when a signal is traveling through the isolator in the pass direction. Correspondingly, such phenomenon appears in acoustic nonlinear systems. For many nonlinear mediums, the mechanism of nonlinearity relies on qualitative or/and quantitative changes of medium states under high input intensity. Once the nonlinearity in these mediums is excited, not only the waves with strong intensity can pass, but also those with weak energy can. A vivid example is the work[58] shown in **Fig. 1.4**. When the surface shape of water is changed by the acoustic pressure radiation, waves with small energy from the upwards side can pass through when the contact between the water and the aluminum layer is established. In this sense, this device cannot operate as a conventional isolator to get rid of back reflections or external noises. This is because the superposition principle does not apply to nonlinear systems[40]. In addition, relatively high functional input amplitude and waveform distortion motivate for seeking alternative methodologies to acoustic nonreciprocity[61].

II.3. Acoustic circulator based systems

In 2014, a groundbreaking work in acoustics was introduced by Fleury et al.[19] to achieve an acoustic analog of the optical circulator. They designed a three ports system of a cavity with a circulating flow that induces an effective angular momentum bias which leads to acoustic splitting effect[62], analog to Zeeman effect in electronics[63]. With a relatively small bias velocity flow v, the wave travels in two different effective speed $c + v$ and $c - v$ (c is the speed of sound in air), which leads to two different resonance modes in the circulator's cavity corresponding to the clockwise and counterclockwise propagations (**Fig. 1.8(a)**). As a result of the splitting effect, a wave incident at port 1 couples with both clockwise and counterclockwise modes in an uneven manner. When there is no flow, the system is passive and sending a wave from port 1 leads to identical wave transmissions in ports 2 and 3 (**Fig. 1.8(b)**). When the flow is introduced by selecting a proper velocity that is optimized via a temporal coupled-mode theory, this bias lead to wave transmission only in port 2 as zero transmission is depicted in port 3 **(Fig. 1.8(c))**. Also, if the acoustic waves are incident from the port 3, the energy will fully escape via the port 2 before it reaches the port 1. The fundamental limitations we have seen in nonlinear system[60] are overcome here by bringing an active system where the flow is introduced to control the effective angular momentum. However, this non-reciprocal system has three ports while it will be more appealing to consider only two ports for unidirectional nonreciprocity. An intuitive and simple modification would be to connect a damping medium to the spare port to eliminate the leaked waves. Later, this acoustic circulator brought interest on considering it as a unit cell for building a hexagonal lattice [64–66] and demonstrate an acoustic analog of a Chern insulator[64].

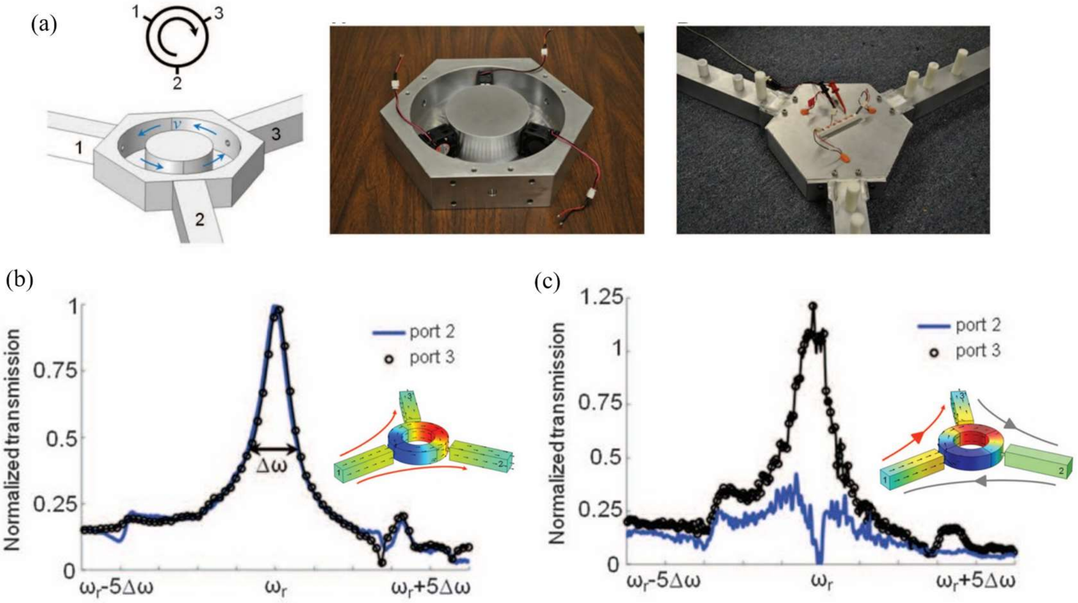

FIG. 1.8. A compact acoustic circulator[19]. (a) The circulator is made of a circular acoustic cavity with three ports where fans were introduced to generate the flow. (b) Transmission for the wave from ports 2 and 3 for the case without flow. (c) Transmission coefficient in the same ports when the flow is introduced.

Another interesting way to take advantage of this circulator system design is to connect the spare port to a phase modulator. In this way, the structure becomes a unidirectional phase modulator which enables multiple functionalities for manipulating acoustic waves. Zhu et al.[26] designed two acoustic circulators connected via one of their ports to realize a Janus phase modulator (**Fig. 1.9(a)**), namely a phase modulator which can unevenly change the wave phase in different propagation directions (**Fig. 1.9(b)**). In **Fig. 1.9(c)**, when the sound wave travels through the structure in forward direction, it is first transmitted to the upper port on the left cavity. After being phase-modulated, the wave is then transmitted to the bottom-right port, which is connected to the right cavity. Since the velocity bias in the right cavity works in opposite direction from that in the left cavity, the sound wave reaches the outlet port instead of the phase modulator port on the left cavity. That is to say, in the forward direction, only the left phase modulator affects the wave. Correspondingly, for the wave propagating in the backward direction, it is the right phase modulator which actually modulates the phase. Both phase modulators on the cavities are replaceable. With this unit cell, the forward wave and backward wave can have independent and adjustable phases. Then multiple unit cells were assembled to form a Janus metascreen. What is represented in **Fig. 1.8(e)** and **(f)** acts beyond the nonreciprocal focusing, instead, it is a Janus focusing. In the forward direction, the plane wave radiation is focused, while in the backward direction, if a monopole source is positioned at the previous focusing point, instead of plane wave radiation towards the left side, a full absorption of the wave is observed. The Janus feature enables personalizing the desired metasurface function on each side of the structure. Apart from this, the authors showed other functionalities such as nonreciprocal refraction, forward focusing with backward refraction, and forward diffusion with backward splitting.

Meanwhile, Mach–Zenhder-interferometer-based nonreciprocal acoustic isolators have also been reported. By coupling an acoustic waveguide with moving media with another static one. Destructive and constructive interference can be then achieved in different propagation directions[67,68].

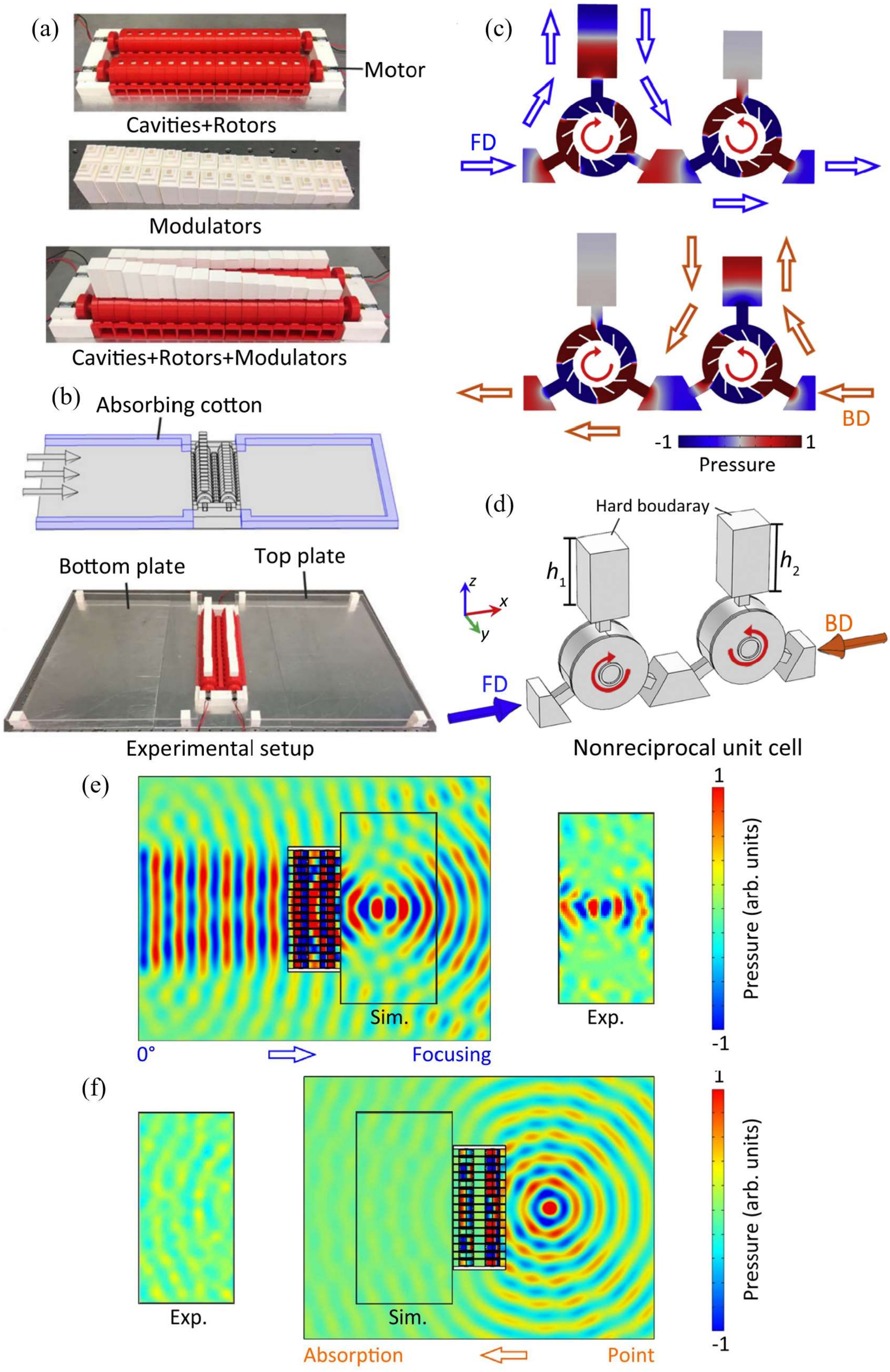

FIG. 1.9. Janus acoustic metascreen[26]. (a) The metascreen prototype composed of multiple unit cells. Two series of coaxial rotors planted in the cavities are driven by 2

motors. The modulators are preconfigured and replaceable. (b) The experiment setup. (c) The acoustic pressure field distributions in the cavities with optimal bias velocity and incidence. The arrows reveal the paths of sound propagation. FD: forward direction. BD: backward direction. (d) Schematic of the unit cell. The rotors in two cavities rotors in inverse directions. Experiment result showing acoustic focusing in the forward direction (e) and sound absorption on the backward direction (f).

II.4. Acoustic spatiotemporal modulation

The application of space-time modulated (STM) medium is an exotic way to realize nonreciprocity which breaks the time reversal symmetry. This methodology was first introduced in 1959 in photonics and electronics, where permittivity, permeability or impedance is harmonically modulated spatiotemporally to create directional bandgaps for waves[69–72]. In special cases as it is discussed in the following part, the STM medium can be seen as medium with its intrinsic properties spatially modulated and moving with a certain velocity. This thus breaks the time reversal symmetry, allowing different dispersion of harmonic waves propagating in different directions. This route, however, faded till this last decade where researchers reinvigorated their interest on the realization of such STM systems, owing to the progress in fabrication and characterization techniques[73–79]. Drawing inspiration from photonics[72,80–83], multiple STM based designs were proposed in acoustics[84–87] and elastodynamics[88–92]. In those designs, certain mechanical properties of the destinated mediums were varied spatiotemporally, or STM resonators are attached on the destinated waveguide to achieve nonreciprocity.

STM in acoustics and elastodynamics[17,62,73,84,88,93,94] has been gaining increasing interest since 2013. In 2016, Trainiti et al.[88] proposed a spatiotemporally modulated elastic waveguide (**Fig. 1.10**), where the Young's modulus of the waveguide is forced to change harmonically in both space and time. When only space modulation is adopted (**Fig. 1.10(a)**), this structure shares the common nature with phononic crystals which features a Bragg bandgap[95,96] in both directions of propagation (**Fig. 1.10(c)**). When the space-time modulation is applied (**Fig. 1.10(b)**), the bandgap experiences a doppler-like shift[40,97] in opposite propagation directions (**Fig. 1.10(d)**). To some extent, this phenomenon is similar to what occurs when moving a space-modulated media in a relatively low constant velocity $v_m = \lambda_m/T_m$, where λ_m and T_m are the spatial period and temporal period of the modulations in corresponding STM[98] , as explained in **Fig. 1.10(e)**. When moving a space-modulated medium (with λ_m as space modulation wavelength) at the speed v_m, what we observe on the structure itself is absolutely the same with STM under Euler coordinate system. In the forward direction, the equivalent group velocity becomes $c + v_m$ where c is original group velocity of longitudinal or transverse motion, while in the backward direction, it becomes $c - v_m$. Then directional bandgaps are formed due to the directional effective group velocity. However, the difference between the STM and the moving time-modulated medium is rooted in the governing equation. When the v_m gets relatively very high, STM and moving space-modulated media differ with each other, since one is stationary then the other is not (**Fig. 1.10(e)**). For the moving space-modulated medium, the whole dispersion relationship is inclined by the v_m, while for the stationary space-time-modulated medium, the dispersion gets complicated as the other propagating modes appear. The dispersion relationship can be obtained by solving quadratic eigenvalue problem (QEP) equations which are discussed in the **Chapter 2**. Additionally, the position where the bandgap appear on the dispersion diagram can be predicted by drawing Floquet-Bloch replicas of the original dispersion curve[89] (translating the original dispersion curves by integer multiples of time-modulation frequency and space-modulation wavelength). At the curve crossings, Bragg's condition[96] is satisfied, and non-reciprocal wave scattering is anticipated. The STM mechanism is also called one-way Bragg mirror[40]. Another important phenomenon along with the STM mechanism is the generation of Floquet-Bloch harmonic modes. Based on this feature, asymmetric frequency conversion is explored on the STM[99].

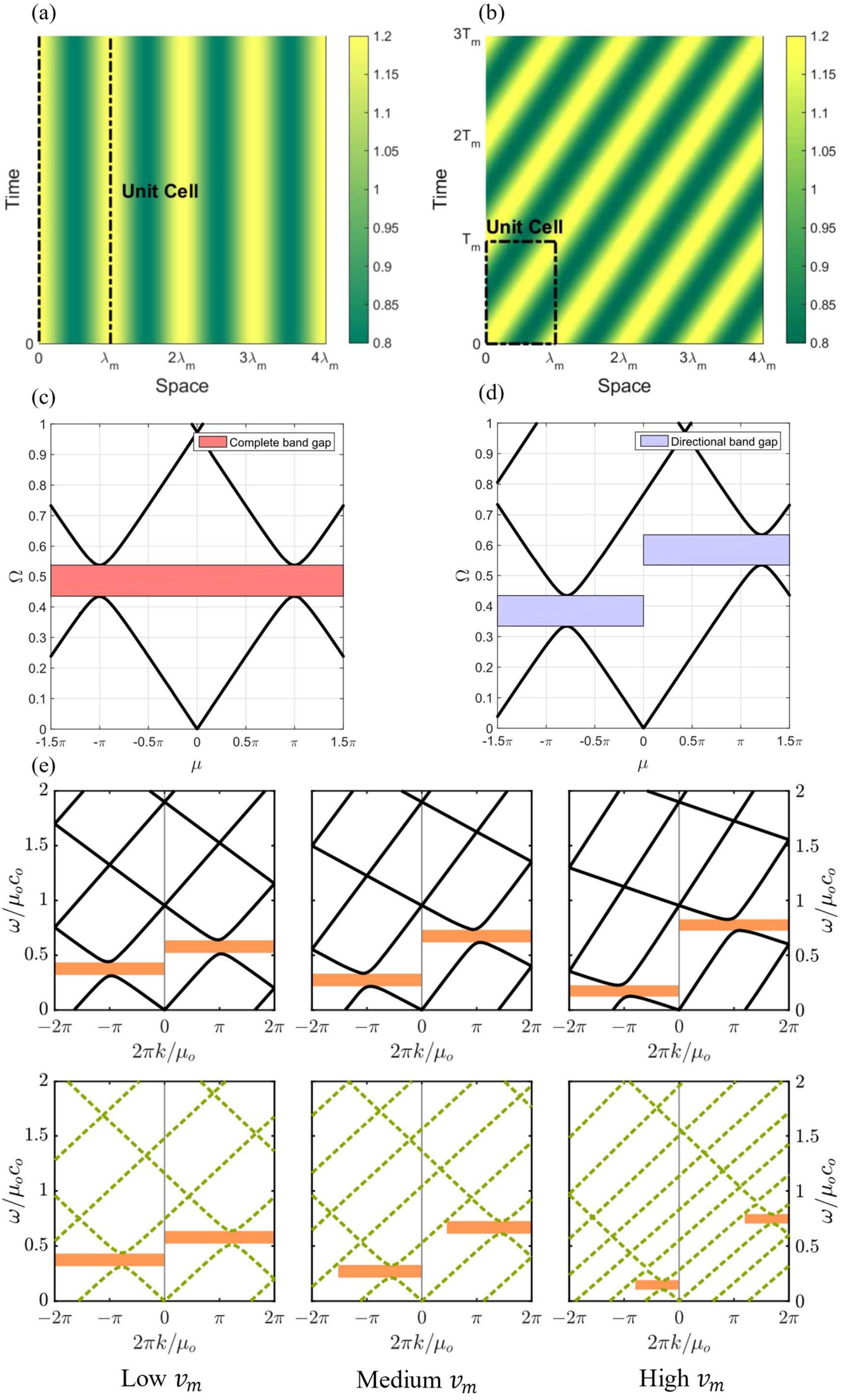
(a)
Unit Cell
Time
Space
0
λ_m
$2\lambda_m$
$3\lambda_m$
$4\lambda_m$
1.2
1.15
1.1
1.05
1
0.95
0.9
0.85
0.8
(b)
Unit Cell
Time
Space
T_m
$2T_m$
$3T_m$
(c)
Complete band gap
Ω
μ
-1.5π
-π
-0.5π
0.5π
π
1.5π
(d)
Directional band gap
Ω
μ
(e)
$\omega/\mu_o c_o$
$2\pi k/\mu_o$
-2π
$-\pi$
π
2π
Low v_m
Medium v_m
High v_m

FIG. 1.10. (a)-(d) The modulations on Young's modulus of an elastic waveguide[88]. λ_m and T_m are the spatial period and temporal period of the modulations. (a) and (c) Spatial-only modulation and the corresponding band diagrams of longitudinal motion. (b) and (d) STM and the corresponding band diagrams of longitudinal motion. (e) Band gap differences between a moving medium with motion velocity v_m and spatially varying Young's modulus (Black solid curves) and a spatiotemporally modulated medium with temporal modulation speed v_m (Green dotted curves)[98]. The bandgaps are marked with orange shaded regions.

Since 2018, several STM systems were proposed later, which are summarized in **Fig. 1.11**. It includes space-time variation of the bulk modulus by attaching modulable Helmholtz resonators on the air waveguide[15] (**Fig. 1.11(a)**), spring-mass resonators (SMR) attached to a waveguide[100] (**Fig. 1.11(b)**), a surface acoustic wave platform with spring-mass chain with modulated stifness[89], a supercell chain with space-time varying pre-strain[101] (**Fig. 1.11(c)**), and space-time varying the effective Young's modulus by adding external stiffness to the host beam[102]. The spring-mass chain proposed by Wang et al. [89] was the first experimental realization of nonreciprocity based on the STM of the effective stiffness. In their experimental setup, several ring magnets are coaxially placed on a cylindrical rail with low-friction sleeve bearings and the same polarization facing each other, as shown in **Fig. 1.11(b)**. The two end magnets are bounded so that the main magnet chain can reach equilibrium with a uniform spacing between neighbors, owing to the magnetic repulsion. When the displacement of ring magnets is relatively small, the repulsion force has a quasi-linear relationship with the displacement, which obeys Hook's Law, so that it could be seen as a basic spring-mass chain. Then, the electrical coils are installed at the concentrated positions of the ring magnets. They are fixed, which can be seen as springs connected to the ground. Equally, under weak displacement condition, Hook's Law is respected on the electromagnetic force between the coils and the magnets. By space-time varying the currents in the coils (alternating currents with phase shift), the effective stiffness of these equivalent external springs is modulated.

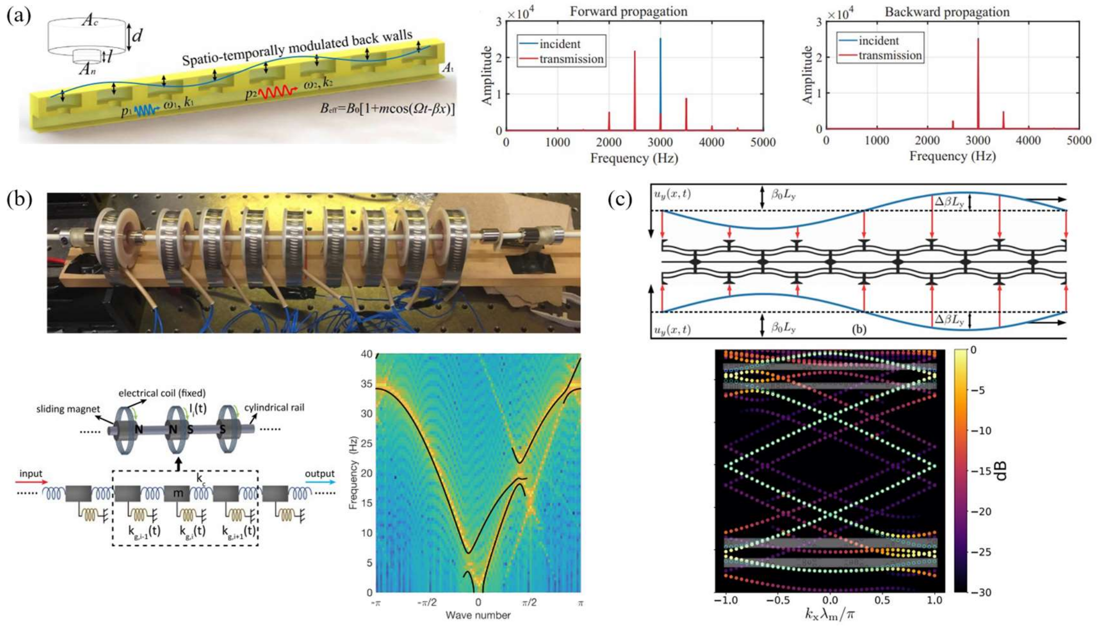

FIG. 1.11. Various approaches for STM acoustic structures. (a) A dynamic air waveguide system[15]. (left) An array of side-loaded Helmholtz resonators with tunable cavity volumes (movable back walls) is attached on the top of air waveguide to modulate the effective bulk modulus in space and time. (Right), frequency spectrum for forward and backward propagations for an incident monochromatic wave at 3000Hz. (b) Space-time modulated dynamic phononic lattice[89]. The phononic lattice is composed of a chain of springs and masses, in which each mass is connected to an external grounded spring whose effective stiffness is space-time modulated via an electromagnetic coupling between sliding magnet and electrical coils. The dispersion characterization shows non-reciprocal dispersion leading to unidirectional bandgap (bottom right panel). (c) An array of deformable supercells[101], which are space-time modulated via nonlinear deformation $u_y = \beta_0 L_y + \Delta\beta L_y \cos(\Omega t - k_m x)$ from an applied external pre-strain. The band structure shows a comparison of spatial modulation (open circles) and STM (filled circles), where the color scale indicates the magnitude of the fundamental component in decibels.

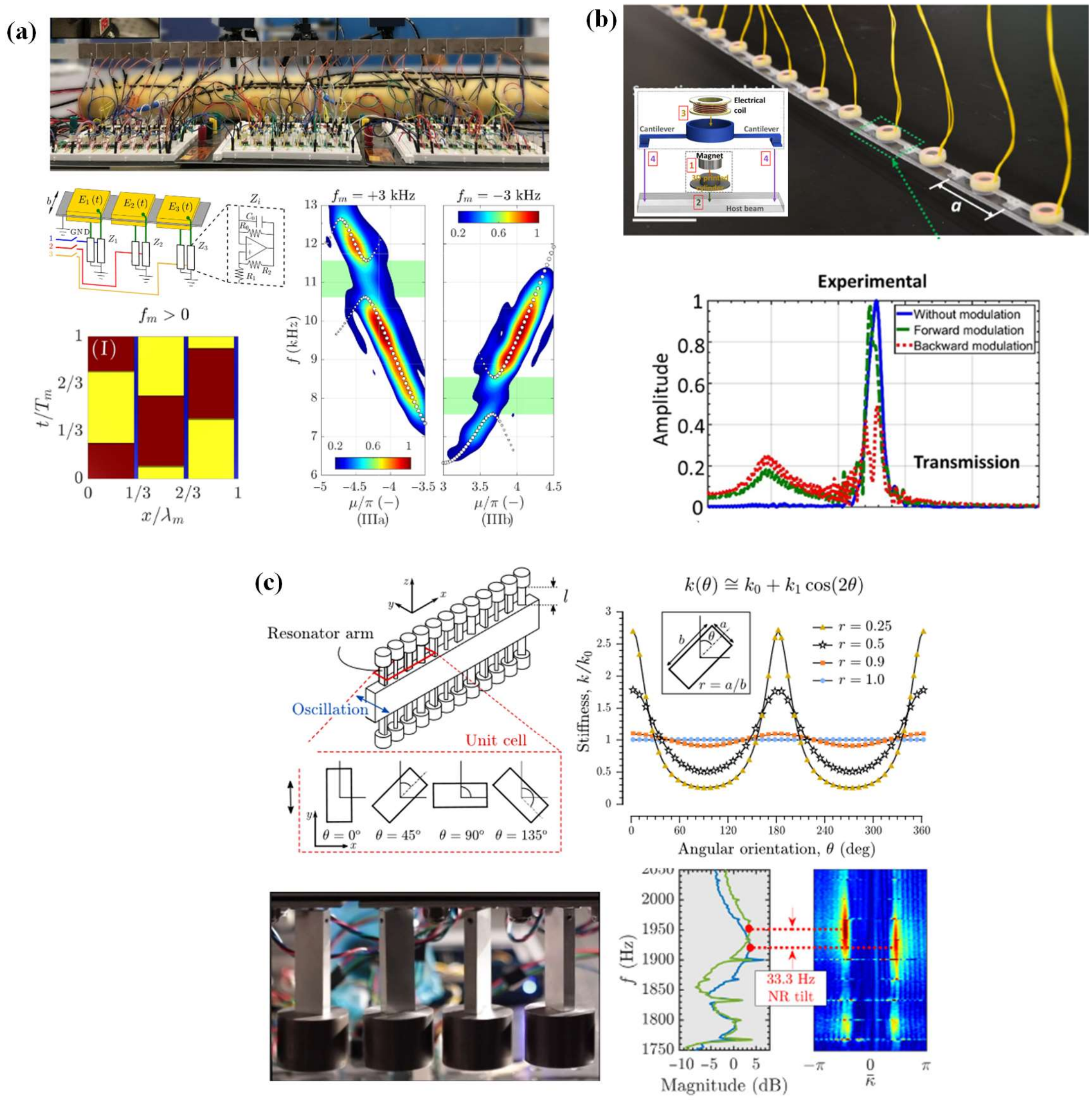

FIG. 1.12. (a) A nonreciprocal phononic plate for flexural waves with spatiotemporally modulated effective bending stiffness via shunted piezoelectric periodic elements[103]. (b) A 1D metamaterial with periodic resonators made of coupled magnets and coils to modulate the local effective stiffness[104]. (c) A 1D metamaterial beam made of a series of resonators where the effective stiffness is modulated via the change in the second area moment of inertia of each resonator's arm through dynamical rotation[103].

However, the solution of Wang et al.[89] only works for longitudinal wave propagation. Other works later performed non-reciprocity for guided waves such as flexural modes in beams. In 2018, the envisaged Young's modulus modulation of Goldsberry et al.[102] is physically realized by Trainiti et al.[105] patching piezoelectric chips connected to negative capacitance circuits on the host beam. In the following year, Marconi et al.[103] added separated switch control for every negative capacitance circuit, complying independent stiffness modulation of each piezoelectric chips to enable STM function (**Fig. 1.12(a)**). However, this STM approach has the drawback that, via switching control, only square-wave style temporal modulation of the Young's modulus can be realized. Unlike the harmonic modulation, the square waveform induces some undesired waves. Subsequently, the attached spring-mass resonator (SMR) solution[100] witnessed a physical realization by Chen et al.[104](**Fig. 1.12(b)**). This work shares a similar concept with the work of Wang et al.[89], both of which utilize the coupling between the electromagnetic field of magnet and coil to modulate the effective spring. The distinction resides in the fact that the coil plays the role of the mass instead of the magnet. The coils are fixed on the cantilevers which provide fundamental stiffness apart from the stiffness from electromagnetic coupling. Another interesting physical realization of SMR is experimentally demonstrated by Attarzadeh et al.[22], where the effective stiffness of the spring varies via the second area moment of inertia of each resonator's arm by dynamically rotating the resonator (**Fig. 1.12(c)**). Conventionally, for flexural waves, the resonators are installed on the lateral sides of the beam, and they vibrate in a flexural motion. The arms of the resonators are of rectangular shape and rotating this arm changes the coupling between the resonator and the flexural waves. When the angle of these arms change by rotation, it induces a variation of the effective stiffness and thus different coupling between the resonators and the flexural wave. With this key feature, Attarzadeh et al.[22] implanted rotating motors in each arm to independently vary the effective stiffness in time, making the system ready for the STM functionality.

Regardless of the achievements in conventional STM, the limitations such as large dimension and synchronization difficulties make these devices cumbersome and challenging to be implemented for practical application. Inspired by the Fabry-Perot (FP) slab structure in optics[82,83], the group of Prof. Steven A. Cummer[85,86,106] introduced the concept of a compact non-reciprocal acoustic device that employs time-modulated bi-resonator structures. This kind of structures couples a waveguide with two cascaded resonators whose mechanical properties are modulated at the identical frequency in time with a temporal phase difference between the modulations of the two resonators (**Fig. 1.13**). Unlike the first proposed STM systems which features directional bandgaps and involves at least ten unit cells to be perfectly synchronized in time, the modulated bi-resonator system only involves two resonant units. Typical examples include cascaded Helmholtz resonators[106] (the bi-resonator version of the envisaged model by J. Li et al.[15]), the cascaded membrane in which the surface tension is time-modulated[86], and the experimentally demonstrated cascaded air cavities whose resonance frequencies are time-modulated[85].

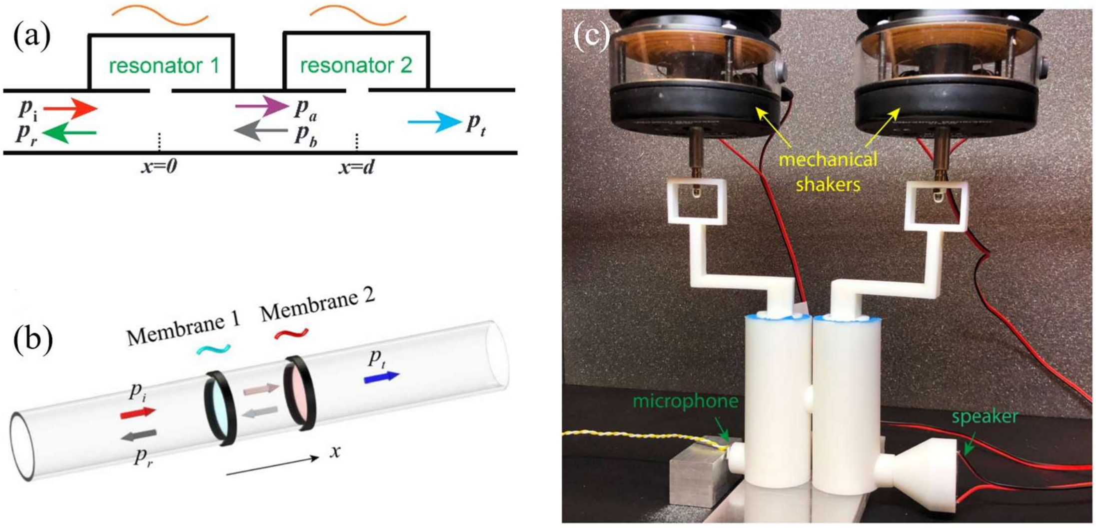

FIG. 1.13. Several compact bi-resonator nonreciprocal structures with temporal modulation. (a) Bi-Helmholtz-resonator coupled air waveguide[106]. (b) Bi-membrane coupled air waveguide[86]. (c) Bi-air-cavity coupled waveguide[85].

II.5. Floquet topological insulators in acoustics and elastodynamics

Nonreciprocity opens new possibilities for wave manipulations. Particularly, topological acoustics, where nonreciprocity is tied to the time-reversal symmetry breaking, has been a flourishing field in the acoustics community for bringing new ways for sound manipulation[61,107]. Topological acoustics is the field of acoustic systems governed by topological invariants, where topological acoustic phenomena remain unperturbed even if the system is distorted by continuous transformations. Topological systems in photonics and acoustics arose from the seminal work on the quantum Hall effect in condensed matter physics. In this effect, in a collection of electrons confined to move in a plane under a magnetic field that breaks the time-reversal symmetry, some electronic states are confined within the outer boundaries ignoring the shape of the bulk. In acoustics and elastodynamics, when time-reversal symmetry is broken using a moving fluid[64], time modulation[108], gyroscopic forces[23,109], acoustic analogs to the quantum Hall effect can be evidenced with the manifestation of topological edge modes that are immune to structural defects.

An experimental implementation of nonreciprocal mechanical topological insulator based on synthetic angular momentum is shown in **Fig. 1.14**. In this implementation, unit cells composed of a PLA (polylactic acid) PLA host layer are bonded to piezoelectric disks which are spatiotemporally modulated by a rotating phase of the modulating signal, breaking the time-reversal symmetry. Topologically protected and backscattering immune wave propagation along edges and interfaces are demonstrated.

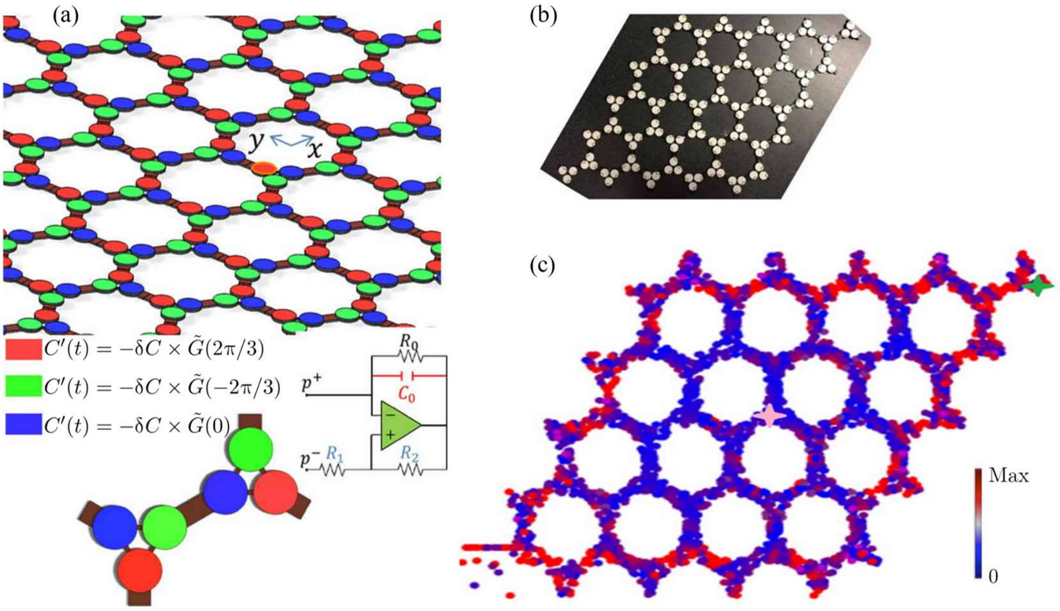

FIG. 1.14. Phononic crystal Floquet topological insulator consisting of a PLA plate with attached piezoelectric disks[108]. Synthetic angular momentum biasing is imparted by space-time modulated piezoelectric disks. (a) Schematic of the time-dependent phononic crystal formed by hexagonal unit cells with PLA as the host layer and attached circular piezoelectric patches and the shunted circuits. (b) Fabricated topological insulator prototype. (c) Experimentally measured displacement field excited by a source, documenting wave propagation along the free edges without backscattering against the defects.

In **Fig. 1.15**, an acoustic Chern insulator using moving fluid is displayed. The circulating fluid, as a kind of angular momentum biasing, breaks the time-reversal symmetry and construct an effective magnetic field, which keeps the Chern number nonvanishing in this system. Nonreciprocal chiral edge states are demonstrated with robust topological protection against various local defects.

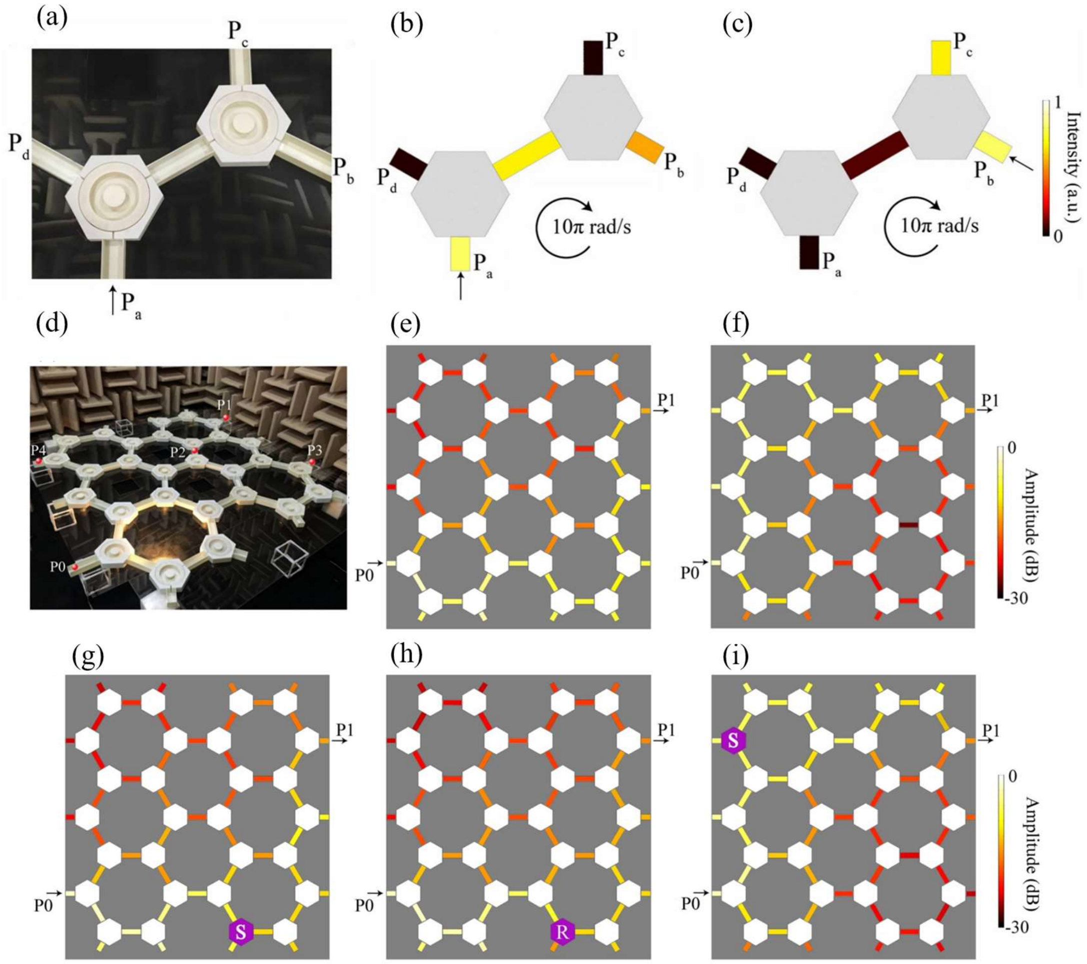

FIG. 1.15. Experimental realization of an acoustic Chern insulator using a circulating flow bias which breaks Lorentz reciprocity[64]. (a) The fabricated unit cell of the acoustic system with four ports defined as P_a, P_b, P_c, and P_d. (b) and (c) The intensity distributions measurements in a unit cell with incident wave from the ports P_a and P_b. (d) The photograph of acoustic Chern insulator prototype. (e-f) Measured pressure amplitude distributions of anticlockwise chiral edge mode and clockwise chiral edge mode. (g), (h) Measured pressure amplitude distributions of anticlockwise chiral edge mode with crystal defects (one selected circulator stops motion or reversely rotates, as denoted by S or R). (i) Measured pressure amplitude distributions of clockwise chiral edge mode with crystal defects.

II.6. Willis coupling

In regular governing equations of acoustics, particular velocity gradient is a function of first order time-derivation of acoustic pressure and pressure gradient is a function of first order time-derivation of particular velocity. But in Willis medium, the coupling between acoustic pressure and particular velocity is considered, then particular velocity and pressure gradients are functions of both first order time-derivations of themselves[110], as described by the following equations[111–113],

$$\frac{\partial u}{\partial x} = j\omega\left(\frac{1}{\kappa}p + \xi u\right) \tag{1.1}$$

$$\frac{\partial p}{\partial x} = j\omega(\rho u + \zeta p) \tag{1.2}$$

Where κ and ρ are the effective bulk modulus and density, while ξ and ζ are the Willis coefficients. The dispersion relationship in the Eq. (1.1) and Eq. (1.2) is,

$$k_{\pm} = \pm\frac{\omega}{2}\sqrt{(\xi-\zeta)^2 + 4\frac{\rho}{\kappa}} + \frac{\omega}{2}(\xi+\zeta) \tag{1.3}$$

The first term with radical sign is the reciprocal portion of the wavenumber, while the second term is the nonreciprocal portion. When $\xi + \zeta$ does not equal 0, strong nonreciprocity appears.

Liu et al.[114] realized the Willis coupling of bending waves in their experiments, and they used the bending resonance of the cantilever beam to prove that Willis coupling causes nonreciprocal reflection amplitude and phase. Liu et al.[115] used passive parity-time symmetric metamaterial crystals to realize the manipulation of unidirectional wave vectors in two-dimensional space. The asymmetric reflection properties of passive parity-time symmetric systems are similar to the anisotropy formulated by Willis coupling. Merkel et al.[116] unified the acoustic Willis coupling with the properties of parity-time symmetric systems under the same framework, indicating that a degenerate point in any case has significant scattering asymmetry and is accompanied by a one-way zero reflection of the acoustic wave.

Various design schemes have been proposed to achieve Willis coupling in acoustic metamaterials[113,117–119]. Muhlestein et al.[117] proposed a one-dimensional asymmetric acoustic system, and demonstrated both theoretically and experimentally that the local behavior of the asymmetric system can be described by asymmetric equivalent parameters. Ma et al.[118] proposed a bi-layer asymmetric acoustic metamaterial with Willis coupling and investigated the relationship between acoustic properties and the asymmetric propagations. Craig et al.[119] systematically achieved the anisotropic coupling between the pressure field and the velocity field in asymmetric wave propagation by using a time-reversal asymmetric acoustic grating. Li et al.[120] utilized super-gradient metasurfaces to achieve anisotropic refraction of acoustic waves, and ensured absolute control of refracted waves by locally controlling the anisotropic response of cells.

III. Conclusion

In this chapter, we have presented state of the art on research on nonreciprocity in the area of acoustics and elastodynamics. We have described different approaches proposed to achieve non-reciprocal wave propagation and gave examples of innovative acoustic nonreciprocal systems for wave uni-directional wave manipulation. Particularly, active acoustic and elastic meta-structures with engineered space and time modulations of their effective mechanical properties opens exciting routes towards exotic wave control. Consequently, this doctoral project focus specifically on contributing to this field by exploring new ways of achieving non-reciprocal wave manifestations using time modulated structural design on acoustic metamaterials.

References

[1] H. Helmholtz, **1860**, 1 (1860).

[2] H. Lamb, Proc. Lond. Math. Soc. **s1-19**, 144 (1887).

[3] A. Clebsch, *Théorie de l'élasticité des corps solides de Clebsch* (Dunod, Éditeur, 1885).

[4] J.C. Maxwell and W.D. Niven, *Sci. Pap. James Clerk Maxwell* (Cambridge University Press, Cambridge, 2011), pp. 598–604.

[5] E. Betti, Il Nuovo Cimento 1869-1876 **7**, 69 (1872).

[6] J.W. Strutt, Proc. Lond. Math. Soc. **s1-4**, 357 (1871).

[7] R.J. Potton, Rep. Prog. Phys. **67**, 717 (2004).

[8] M. Born and E. Wolf, *Principles of Optics: Electromagnetic Theory of Propagation, Interference and Diffraction of Light*, 7th ed. (Cambridge University Press, Cambridge, 1999).

[9] H.A. Lorentz, in *Collect. Pap. Vol. V*, edited by H.A. Lorentz (Springer Netherlands, Dordrecht, 1937), pp. 1–138.

[10] J.A. Achenbach and J.D. Achenbach, *Reciprocity in Elastodynamics* (Cambridge University Press, 2003).

[11] J. Zhang, B.W. Drinkwater, P.D. Wilcox, and A.J. Hunter, NDT E Int. **43**, 123 (2010).

[12] E. Larose, L. Margerin, B.A. van Tiggelen, and M. Campillo, Phys. Rev. Lett. **93**, 048501 (2004).

[13] K.L. Tsakmakidis, L. Shen, S.A. Schulz, X. Zheng, J. Upham, X. Deng, H. Altug, A.F. Vakakis, and R.W. Boyd, Science **356**, 1260 (2017).

[14] N. Boechler, G. Theocharis, and C. Daraio, Nat. Mater. **10**, 665 (2011).

[15] J. Li, C. Shen, X. Zhu, Y. Xie, and S.A. Cummer, Phys. Rev. B **99**, 144311 (2019).

[16] A. Mojahed, O.V. Gendelman, and A.F. Vakakis, J. Acoust. Soc. Am. **146**, 826 (2019).

[17] K. Yi, M. Collet, and S. Karkar, Phys. Rev. B **98**, 054109 (2018).

[18] I.H. Grinberg, M. Lin, C. Harris, W.A. Benalcazar, C.W. Peterson, T.L. Hughes, and G. Bahl, Nat. Commun. **11**, 974 (2020).

[19] R. Fleury, D.L. Sounas, C.F. Sieck, M.R. Haberman, and A. Alù, Science **343**, 516 (2014).

[20] B. Liang, X.S. Guo, J. Tu, D. Zhang, and J.C. Cheng, Nat. Mater. **9**, 989 (2010).

[21] Z. You, A. Baskaran, and M.C. Marchetti, Proc. Natl. Acad. Sci. **117**, 19767 (2020).

[22] M.A. Attarzadeh, J. Callanan, and M. Nouh, Phys. Rev. Appl. **13**, 021001 (2020).

[23] Y. Zhao, X. Zhou, and G. Huang, J. Mech. Phys. Solids **143**, 104065 (2020).

[24] B. Liang, B. Yuan, and J. Cheng, Phys. Rev. Lett. **103**, 104301 (2009).

[25] J. Zhu, X. Zhu, X. Yin, Y. Wang, and X. Zhang, Phys. Rev. Appl. **13**, 041001 (2020).

[26] Y. Zhu, L. Cao, A. Merkel, S.-W. Fan, B. Vincent, and B. Assouar, Nat. Commun. **12**, 7089 (2021).

[27] K.J. Moore, J. Bunyan, S. Tawfick, O.V. Gendelman, S. Li, M. Leamy, and A.F. Vakakis, Phys. Rev. E **97**, 012219 (2018).

[28] X. Zhu, X. Zou, B. Liang, and J. Cheng, J. Appl. Phys. **108**, 124909 (2010).

[29] H. Sun, S. Zhang, and X. Shui, Appl. Phys. Lett. **100**, 103507 (2012).

[30] A. Cicek, O. Adem Kaya, and B. Ulug, Appl. Phys. Lett. **100**, 111905 (2012).

[31] J. Hwan Oh, H. Woong Kim, P. Sik Ma, H. Min Seung, and Y. Young Kim, Appl. Phys. Lett. **100**, 213503 (2012).

[32] X.-F. Li, X. Ni, L. Feng, M.-H. Lu, C. He, and Y.-F. Chen, Phys. Rev. Lett. **106**, 084301 (2011).

[33] Z. He, S. Peng, Y. Ye, Z. Dai, C. Qiu, M. Ke, and Z. Liu, Appl. Phys. Lett. **98**, 083505 (2011).

[34] Y.-F. Zhu, X.-Y. Zou, B. Liang, and J.-C. Cheng, Appl. Phys. Lett. **107**, 113501 (2015).

[35] X.-P. Wang, L.-L. Wan, T.-N. Chen, Q.-X. Liang, and A.-L. Song, Appl. Phys. Lett. **109**, 044102 (2016).

[36] B. Yuan, B. Liang, J. Tao, X. Zou, and J. Cheng, Appl. Phys. Lett. **101**, 043503 (2012).

[37] M. di Bernardo, C.J. Budd, A.R. Champneys, P. Kowalczyk, A.B. Nordmark, G.O. Tost, and P.T. Piiroinen, SIAM Rev. (2008).

[38] Y.A. Kuznetsov, *Elements of Applied Bifurcation Theory* (Springer New York, New York, NY, 2004).

[39] B. Deng, P. Wang, Q. He, V. Tournat, and K. Bertoldi, Nat. Commun. **9**, 3410 (2018).

[40] H. Nassar, B. Yousefzadeh, R. Fleury, M. Ruzzene, A. Alù, C. Daraio, A.N. Norris, G. Huang, and M.R. Haberman, Nat. Rev. Mater. **5**, 667 (2020).

[41] S. Lepri and G. Casati, Phys. Rev. Lett. **106**, 164101 (2011).

[42] Z. Lu and A.N. Norris, J. Vib. Acoust. **142**, (2019).

[43] A. Cebrecos, N. Jiménez, V. Romero-García, R. Picó, V.J. Sánchez-Morcillo, and L.M. García-Raffi, AIP Adv. **6**, 121601 (2016).

[44] U. Harbola, A. Rosas, M. Esposito, and K. Lindenberg, Phys. Rev. E **80**, 031303 (2009).

[45] A. Mojahed, J. Bunyan, S. Tawfick, and A.F. Vakakis, Phys. Rev. Appl. **12**, 034033 (2019).

[46] A. Merkel, V. Tournat, and V. Gusev, Phys. Rev. E **90**, 023206 (2014).

[47] T. Devaux, V. Tournat, O. Richoux, and V. Pagneux, Phys. Rev. Lett. **115**, 234301 (2015).

[48] K. Li and P. Rizzo, J. Sound Vib. **365**, 15 (2016).

[49] A. Darabi, L. Fang, A. Mojahed, M.D. Fronk, A.F. Vakakis, and M.J. Leamy, Phys. Rev. B **99**, 214305 (2019).

[50] C. Fu, B. Wang, T. Zhao, and C.Q. Chen, Appl. Phys. Lett. **112**, 051902 (2018).

[51] Y.A. Kosevich, Phys. Rev. B **52**, 1017 (1995).

[52] V.F. Nesterenko, C. Daraio, E.B. Herbold, and S. Jin, Phys. Rev. Lett. **95**, 158702 (2005).

[53] J. D’Ambroise, P.G. Kevrekidis, and S. Lepri, J. Phys. Math. Theor. **45**, 444012 (2012).

[54] A.S. Gliozzi, M. Miniaci, A.O. Krushynska, B. Morvan, M. Scalerandi, N.M. Pugno, and F. Bosia, Sci. Rep. **9**, 9560 (2019).

[55] S.P. Wallen, M.R. Haberman, Z. Lu, A. Norris, T. Wiest, and C.C. Seepersad, Proc. Meet. Acoust. **34**, 065002 (2018).

[56] I. Grinberg, A.F. Vakakis, and O.V. Gendelman, Wave Motion **83**, 49 (2018).

[57] J. Bunyan and S. Tawfick, Adv. Eng. Mater. **21**, 1800791 (2019).

[58] T. Devaux, A. Cebrecos, O. Richoux, V. Pagneux, and V. Tournat, Nat. Commun. **10**, 3292 (2019).

[59] J.-G. Cui, T. Yang, and L.-Q. Chen, Appl. Phys. Lett. **112**, 181904 (2018).

[60] Y. Shi, Z. Yu, and S. Fan, Nat. Photonics **9**, 388 (2015).

[61] C. Rasmussen, L. Quan, and A. Alù, J. Appl. Phys. **129**, 210903 (2021).

[62] D.L. Sounas, C. Caloz, and A. Alù, Nat. Commun. **4**, 2407 (2013).

[63] P. Zeeman, Lond. Edinb. Dublin Philos. Mag. J. Sci. **43**, 226 (1897).

[64] Y. Ding, Y. Peng, Y. Zhu, X. Fan, J. Yang, B. Liang, X. Zhu, X. Wan, and J. Cheng, Phys. Rev. Lett. **122**, 014302 (2019).

[65] Z. Yang, F. Gao, X. Shi, X. Lin, Z. Gao, Y. Chong, and B. Zhang, Phys. Rev. Lett. **114**, 114301 (2015).

[66] A.B. Khanikaev, R. Fleury, S.H. Mousavi, and A. Alù, Nat. Commun. **6**, 8260 (2015).

[67] N. Janković and A. Alù, Phys. Rev. Appl. **15**, 024004 (2021).

[68] C.P. Wiederhold, D.L. Sounas, and A. Alù, J. Acoust. Soc. Am. **146**, 802 (2019).

[69](n.d.).

[70] E.S. Cassedy and A.A. Oliner, Proc. IEEE **51**, 1342 (1963).

[71] E.S. Cassedy, Proc. Inst. Electr. Eng. **112**, 269 (1965).

[72] D.L. Sounas and A. Alù, Nat. Photonics **11**, 774 (2017).

[73] Y. Hadad, D.L. Sounas, and A. Alu, Phys. Rev. B **92**, 100304 (2015).

[74] S. Taravati, Phys. Rev. B **96**, 235150 (2017).

[75] S. Taravati, N. Chamanara, and C. Caloz, Phys. Rev. B **96**, 165144 (2017).

[76] S. Taravati, Phys. Rev. B **97**, 115131 (2018).

[77] S. Taravati, Phys. Rev. Appl. **9**, 064012 (2018).

[78] S. Taravati and G.V. Eleftheriades, Sci. Rep. **11**, 7377 (2021).

[79] S. Taravati and G.V. Eleftheriades, ArXiv210303360 Phys. (2021).

[80] Z. Yu and S. Fan, Nat. Photonics **3**, 91 (2009).

[81] D.-W. Wang, H.-T. Zhou, M.-J. Guo, J.-X. Zhang, J. Evers, and S.-Y. Zhu, Phys. Rev. Lett. **110**, 093901 (2013).

[82] J.R. Zurita-Sánchez, P. Halevi, and J.C. Cervantes-González, Phys. Rev. A **79**, 053821 (2009).

[83] M. Chegnizadeh, M. Memarian, and K. Mehrany, JOSA B **37**, 88 (2020).

[84] R. Fleury, D.L. Sounas, and A. Alù, Phys. Rev. B **91**, 174306 (2015).

[85] C. Shen, X. Zhu, J. Li, and S.A. Cummer, Phys. Rev. B **100**, 054302 (2019).

[86] X. Zhu, J. Li, C. Shen, X. Peng, A. Song, L. Li, and S.A. Cummer, Appl. Phys. Lett. **116**, 034101 (2020).

[87] M. Oudich, Y. Deng, M. Tao, and Y. Jing, Phys. Rev. Res. **1**, 033069 (2019).

[88] G. Trainiti and M. Ruzzene, New J. Phys. **18**, 083047 (2016).

[89] Y. Wang, B. Yousefzadeh, H. Chen, H. Nassar, G. Huang, and C. Daraio, Phys. Rev. Lett. **121**, 194301 (2018).

[90] K. Yi, M. Ouisse, E. Sadoulet-Reboul, and G. Matten, Smart Mater. Struct. **28**, 065025 (2019).

[91] C. Sugino, M. Ruzzene, and A. Erturk, Phys. Rev. B **102**, 014304 (2020).

[92] M. Farhat, S. Guenneau, P.-Y. Chen, and Y. Wu, Phys. Rev. B **104**, 014308 (2021).

[93] N. Swinteck, S. Matsuo, K. Runge, J.O. Vasseur, P. Lucas, and P.A. Deymier, J. Appl. Phys. **118**, 063103 (2015).

[94] F. Li, C. Chong, J. Yang, P.G. Kevrekidis, and C. Daraio, Phys. Rev. E **90**, 053201 (2014).

[95] Z. Liu, X. Zhang, Y. Mao, Y.Y. Zhu, Z. Yang, C.T. Chan, and P. Sheng, Science **289**, 1734 (2000).

[96] W.H. Bragg and W.L. Bragg, Proc. R. Soc. Lond. Ser. Contain. Pap. Math. Phys. Character **88**, 428 (1913).

[97] X. Hu, Z. Hang, J. Li, J. Zi, and C.T. Chan, Phys. Rev. E **73**, 015602 (2006).

[98] M.A. Attarzadeh and M. Nouh, AIP Adv. **8**, 105302 (2018).

[99] X. Wen, X. Zhu, A. Fan, W.Y. Tam, J. Zhu, H.W. Wu, F. Lemoult, M. Fink, and J. Li, Commun. Phys. **5**, 1 (2022).

[100] Q. Wu, H. Chen, H. Nassar, and G. Huang, J. Mech. Phys. Solids **146**, 104196 (2021).

[101] B.M. Goldsberry, S.P. Wallen, and M.R. Haberman, J. Acoust. Soc. Am. **146**, 782 (2019).

[102] B.M. Goldsberry, S.P. Wallen, and M.R. Haberman, Phys. Rev. B **102**, 014312 (2020).

[103] J. Marconi, E. Riva, M. Di Ronco, G. Cazzulani, F. Braghin, and M. Ruzzene, Phys. Rev. Appl. **13**, 031001 (2020).

[104] Y. Chen, X. Li, H. Nassar, A.N. Norris, C. Daraio, and G. Huang, Phys. Rev. Appl. **11**, 064052 (2019).

[105] G. Trainiti, Y. Xia, J. Marconi, G. Cazzulani, A. Erturk, and M. Ruzzene, Phys. Rev. Lett. **122**, 124301 (2019).

[106] C. Shen, J. Li, Z. Jia, Y. Xie, and S.A. Cummer, Phys. Rev. B **99**, 134306 (2019).

[107] R. Fleury, A.B. Khanikaev, and A. Alù, Nat. Commun. **7**, 11744 (2016).

[108] A. Darabi, X. Ni, M. Leamy, and A. Alù, Sci. Adv. **6**, eaba8656 (2020).

[109] L. Zhang, J. Ren, J.-S. Wang, and B. Li, Phys. Rev. Lett. **105**, 225901 (2010).

[110] M.B. Muhlestein, C.F. Sieck, A. Alù, and M.R. Haberman, Proc. R. Soc. Math. Phys. Eng. Sci. **472**, 20160604 (2016).

[111] G.W. Milton and J.R. Willis, Proc. R. Soc. Math. Phys. Eng. Sci. **463**, 855 (2007).

[112] C.F. Sieck, A. Alù, and M.R. Haberman, Phys. Rev. B **96**, 104303 (2017).

[113] L. Quan, Y. Ra'di, D.L. Sounas, and A. Alù, Phys. Rev. Lett. **120**, 254301 (2018).

[114] Y. Liu, Z. Liang, J. Zhu, L. Xia, O. Mondain-Monval, T. Brunet, A. Alù, and J. Li, Phys. Rev. X **9**, 011040 (2019).

[115] T. Liu, X. Zhu, F. Chen, S. Liang, and J. Zhu, Phys. Rev. Lett. **120**, 124502 (2018).

[116] A. Merkel, V. Romero-García, J.-P. Groby, J. Li, and J. Christensen, Phys. Rev. B **98**, 201102 (2018).

[117] M.B. Muhlestein, C.F. Sieck, P.S. Wilson, and M.R. Haberman, Nat. Commun. **8**, 15625 (2017).

[118] F. Ma, M. Huang, Y. Xu, and J.H. Wu, J. Appl. Phys. **123**, 035104 (2018).

[119] S.R. Craig, X. Su, A. Norris, and C. Shi, Phys. Rev. Appl. **11**, 061002 (2019).

[120] J. Li, C. Shen, A. Díaz-Rubio, S.A. Tretyakov, and S.A. Cummer, Nat. Commun. **9**, 1342 (2018).

Chapter 2

Nonreciprocal acoustics: theory and modeling approaches

Contents

I. Introduction

Since 2014, great interest was brought to the realization of non-reciprocal acoustic wave propagation via space-time modulated (STM) systems and moving media which have taken the place of nonreciprocal metamaterials using nonlinear materials[1]. The STM and moving media systems are based on time-variation of the effective mechanical properties which involves solving the acoustic governing equations with time dependent parameters. This sparked the development of analytical and numerical approaches such as finite element method (FEM)[2–6] to describe the wave dispersion on these systems. Despite the practicability of using numerical methods, they remain mostly based on solving the system in the time domain which is time consuming. Hence, analytical and semi-analytical approaches were developed. The well-corelated analytical approaches reduce the need of large computational resources and facilitate experimental realizations. Among the analytical approaches adopted for time-varying media are the temporal coupled-mode theory (TCMT)[3,7], the transfer matrix method (TMM)[4], and the quadratic eigenvalue problem (QEP) solving[8,9] .

In this chapter, we focus on the theoretical approaches used in the study of space-or-time modulated systems and moving media. We first briefly introduce the FEM and the finite difference time domain (FDTD) as two major numerical approaches. Then we present in detail the three semi-analytical approaches: TCMT, TMM, and QEP. We show with demonstration how the solution is developed in these approaches and give examples. We also discuss their applicability and limitations.

II. Numerical approaches

Numerical approaches are indispensable for getting reference solution corelating the analytical models, predicting the experimental results, and optimizing the structural design of the system, in which FEM and the FDTD are frequently adopted.

FEM is based on arbitrarily dividing a continuous solution domain into many tiny elements of appropriate shape defined by nodes, and to construct an interpolation function in each small element[10]. The governing equation of the problem is converted into finite element equations on all elements, that is, the local elements are synthesized as an entity to form an algebraic equation system with the specified boundary conditions being implanted. By solving the set of equations, the values of the solution on each node are calculated. The boundary element method (BEM), derivatized from FEM, uses the Green's function formula to convert the partial differential equation in the spatial solution domain into the integral equation on its boundary[11]. Although with the same discrete precision, the precision of BEM solution is higher than that of FEM, BEM is only frequently used in the industry.

The FDTD method is based on discretizing the derivatives in the governing equations to be solved by the difference quotient of the function value on the grid node, thereby establishing a set of algebraic equations with the unknown value on the grid node[12]. This method gives an approximate numerical solution that directly turns a differential problem into an algebraic problem, with intuitive mathematical concept and the simple expression.

The FEM is suitable for dealing with complex structures with acceptable precision for specific number of mesh elements. The disadvantage is the huge amount of needed memory and computation time. The FTDT method is intuitive, easy to program and parallelize, but has dispersion errors and tedious processing of irregular areas[13] and can also be time consuming for large and complex systems.

Having a complete, stable, and reliable numerical tools facilitating the use of FEM such as COMSOL Multiphysics and ANSYS, FEM is much preferred by researchers to solve a system with complex geometry and parameters with high practicability. For example, solving the equations for the air circulator system with predefined air flux field[2,3], using time-dependent parameters in transit calculations to solve time-modulated system[4,5], calculating the mode shapes of unit cell[6], etc. In contrast, FTDT is usually applied to simple 1D structure[9,14].

Unlike conventional time-invariant structure can be calculated in steady state (FEM frequency domain simulation in COMSOL), the time-variant structure is not possible to be steady in definition. So, the numerical calculation of time-variant structure must be performed time-dependently.

The FEM transit simulation in COMSOL is utilized for all the time-variant structures in our research, which allows us to vary the properties of the structure in time by defining functions of time. As for the excitation, we use Gaussian signal. Due to precision purpose, the duration of this Gaussian signal must be much longer than the period of time modulation. As result, we get a time-domain response signal. Then we postprocess this time-domain response signal with Fast Fourier Transform (FFT) without adding any window, and we can finally get the frequency domain response.

III. Analytical approaches

TCMT, TMM, and QEP, are considered to be the "shell" for finding solutions in the case of STM systems or moving-media systems. When the time variation of the effective properties of the medium is introduced, the frequency response of the system undergoes mode conversion or parameter biasing. Fourier decomposition in time or perturbation method is used to write the formulation of the general solution which is then implanted into the "shell" approach.

In a time-periodic system where the Floquet theorem can be applied, we expand the solution into finite orders of modes both in time and space (Fourier decomposition in the space or time variables), then we search for the relationship between different coefficients of the orders knowing the input and output parameters. The precision of solution is related to the number of the orders considered. In most space-or-time periodic system with slow variation, the higher order modes can be neglected (orders > 4 or < -4), so an expansion to a first three orders is generally sufficient to get a good approximation of the solution in most cases.

The perturbation method is also called the small parameter expansion method. Using the perturbation method to solve the asymptotic solution of the equation, the physical equation and the final solution conditions are usually dimensionless, and a small parameter reflecting the physical characteristics (for example, the stiffness in the elastic equation) is selected as the perturbation factor. It is assumed that the solution can be developed into a power series with small parameters, and after substituting this series into the dimensionless equation, approximate equations at all orders can be obtained. The coefficients of each power series can be determined, and the asymptotic solution of the original equation can be obtained by truncating the series.

Since the perturbation method is not the principal core solution in this thesis, we will not describe into further details this method. One can consult the work of Chen *et al.*[8] where a typical perturbation method for spatiotemporally modulated system is described. We will only focus on the Fourier decomposition in time in this chapter, and in each following part, we show how the decomposition of the solution is implanted into the "shell" approaches.

III.1. Temporal coupled-mode theory (TCMT)

The temporal coupled-mode theory (TCMT) is initially developed for describing the Fano resonance in optical resonators[15,16]. It can be used in most finite systems. Under one-dimension condition, we consider a static resonator coupled with 2 ports, labeled 1 and 2 (**Fig. 2.1(b)**).

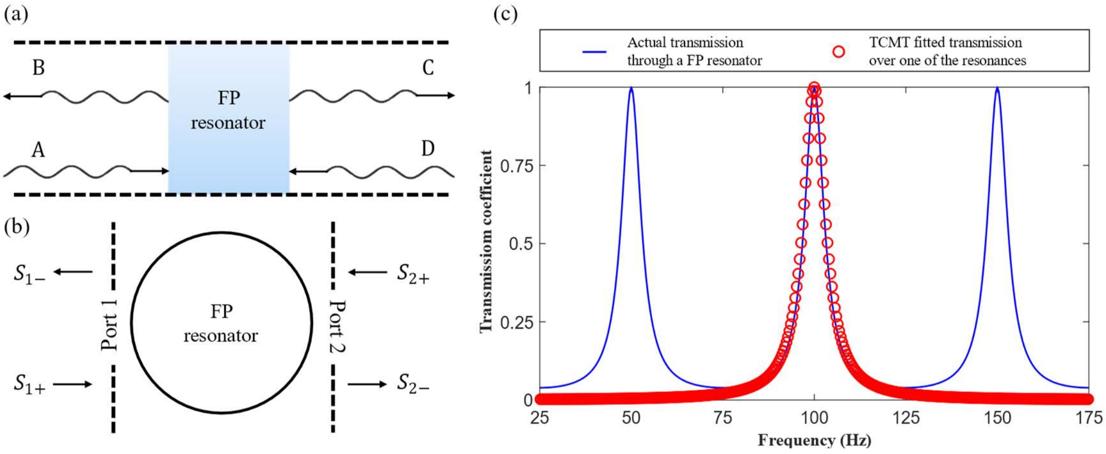

FIG. 2.1. (a) Single Fabry-Perot (FP) resonator implanted in an air waveguide for longitudinal wave propagation. (b) The corresponding schematic for the TCMT method. (c) A result of the single FP resonator system using TCMT. The blue curve is the actual transmission coefficient of this system (using TMM), and the red circles are the single-mode TCMT fitted transmission coefficient over the second order resonance frequency.

The incident waves and the outgoing waves writes, respectively,

$$\boldsymbol{s}_{+} = \begin{bmatrix} s_{1+} \\ s_{2+} \end{bmatrix} \tag{2.1}$$

$$\boldsymbol{s}_{-} = \begin{bmatrix} s_{1-} \\ s_{2-} \end{bmatrix} \tag{2.2}$$

The dynamic equations for the normalized amplitude a of the resonance mode can be written as

$$\frac{da}{dt} = \left(j\omega_0 - \frac{1}{\tau}\right) a + \boldsymbol{\kappa} \cdot \boldsymbol{s}_{+} \tag{2.3}$$

$$\boldsymbol{s}_{-} = \boldsymbol{C}\boldsymbol{s}_{+} + a\boldsymbol{\kappa} \tag{2.4}$$

where ω_0 is the resonance frequency, τ is the resonance lifetime, and $\boldsymbol{\kappa}$ is the vector of coupling constant between the resonance and waves at the ports,

$$\boldsymbol{\kappa} = \begin{bmatrix} \kappa_1 \\ \kappa_2 \end{bmatrix} \tag{2.5}$$

In the case with the same waveguide medium connected to the two ports, we consider $\kappa_1 = \kappa_2$. $\boldsymbol{C}$ is the scattering matrix which relates directly the incident waves to the outgoing waves at ports, acquiring a special form[17],

$$\boldsymbol{C} = e^{j\phi} \begin{bmatrix} r & jt \\ jt & r \end{bmatrix} \tag{2.6}$$

where r, t and ϕ are real constant with $r^2 + t^2 = 1$. In Fabry-Perot (FP) resonators, $\boldsymbol{C}$ is an identity matrix[18]. According to Fan et al.[15], the condition $\boldsymbol{\kappa} \cdot \boldsymbol{\kappa} = 2/\tau$ is satisfied under time-reversal symmetry.

From the above equations, we can easily derive the transmission coefficient s_{2-}/s_{1+} of this single static resonator with the incidence at the frequency ω,

$$\frac{s_{2-}}{s_{1+}} = \frac{1/\tau}{j(\omega - \omega_0) + 1/\tau} \tag{2.7}$$

The disadvantage of TCMT is that τ and $\boldsymbol{\kappa}$, as key parameters in this method, are not directly related to any physical properties in acoustics and elastodynamics. To acquire the values of these parameters, the practical way is to fit the TCMT equation to the results of experiments[7] or numerical simulations[18]. Additionally, if only one resonance mode is considered, the TCMT only works near the considered resonance. In **Fig. 2.1(c)**, we show an example of single-mode TCMT result of the single Fabry-Perot (FP) resonator system (**Fig. 2.1(a)**). It is clearly shown that for a system with multiple harmonic resonances, single-mode TCMT only works around the fitted one of interest in the study. To be able to describe the system around the other resonances, we have to consider the modes coupling[16]. The analytical approach used in the acoustic circulator system[3] is a typical 3-port TCMT with 2 coupled modes (splitting resonance modes, see the introduction in Chapter 1 section II.3).

Equation 2.7 is for a single-mode TCMT model for static resonator. We then consider the case of a time-varying resonator. To solve this problem, we first use the perturbation method and then perform the PWE. The time-varying terms are seen as perturbations in TCMT. We postulate that by using a time-varying sound speed in the acoustic FP resonator, its resonance frequency and the coupling constants will change in time. Since the perturbation is time-dependent with periodic perturbations, $\sum_{-P}^{P} \alpha_p e^{jp\Omega t}$

(perturbations of complex resonance frequency) and $\sum_{-P}^{P}\boldsymbol{\chi}_p e^{jp\Omega t}$ (perturbations of the coupling coefficients), are considered for both complex resonance frequency and the coupling constants,

$$\frac{da}{dt}=\left(j\omega_0-\frac{1}{\tau}+\sum_p \alpha_p e^{jp\Omega t}\right)a+\left(\boldsymbol{\kappa}+\sum_p \boldsymbol{\chi}_p e^{jp\Omega t}\right)\cdot \boldsymbol{s}_+ \tag{2.8}$$

where Ω is the modulation angular frequency. If we only consider the incidence at the port 1, $s_{1+}=e^{j\omega t}$, then all the terms concerning the s_{2+} are eliminated

$$\frac{da}{dt}=\left(j\omega_0-\frac{1}{\tau}+\sum_p \alpha_p e^{jp\Omega t}\right)a+\left(\kappa_1+\sum_p \chi_{1,p} e^{jp\Omega t}\right)s_{1+} \tag{2.9}$$

According to the Floquet theorem, the general solution of the amplitude in the resonator should be,

$$a=\sum_n a_n e^{j(\omega+n\Omega)t} \tag{2.10}$$

By inserting Eq (2.10) into Eq (2.9), and presuming $s_{1+}=\sum_n \delta_n e^{j(\omega+n\Omega)t}$, in which δ_n is Kronecker function, one can have

$$\sum_n j(\omega+n\Omega)a_n e^{j(\omega+n\Omega)t}=\left(j\omega_0-\frac{1}{\tau}+\sum_p \alpha_p e^{jp\Omega t}\right)\sum_n a_n e^{j(\omega+n\Omega)t}$$
$$+\left(\kappa_1+\sum_p \chi_{1,p} e^{jp\Omega t}\right)\sum_n \delta_n e^{j(\omega+n\Omega)t} \tag{2.11}$$

At this stage, by replacing p by $n'-n$ and some further index replacements,

$$\left[j(\omega-\omega_0+n\Omega)+\frac{1}{\tau}\right]a_n-\sum_{n'}\alpha_{n-n'}a_{n'}=\kappa_1\delta_n+\sum_{n'}\chi_{1,n-n'}\delta_{n'} \tag{2.12}$$

This equation can be written in a vectorial form (we consider only -1, 0 and +1 orders for simplification purpose),

$$\begin{bmatrix} w_{-1}-\alpha_0 & -\alpha_{-1} & -\alpha_{-2} \\ -\alpha_{+1} & w_0-\alpha_0 & -\alpha_{-1} \\ -\alpha_{+2} & -\alpha_{+1} & w_{+1}-\alpha_0 \end{bmatrix}\begin{bmatrix} a_{-1} \\ a_0 \\ a_{+1} \end{bmatrix}=\begin{bmatrix} \chi_{1,+1} \\ \kappa_1+\chi_{1,0} \\ \chi_{1,-1} \end{bmatrix} \tag{2.13}$$

where $w_n = j(\omega - \omega_0 + n\Omega) + \frac{1}{\tau}$. Denoting that,

$$\boldsymbol{W} = \begin{bmatrix} w_{-1} - \alpha_0 & -\alpha_{-1} & -\alpha_{-2} \\ -\alpha_{+1} & w_0 - \alpha_0 & -\alpha_{-1} \\ -\alpha_{+2} & -\alpha_{+1} & w_{+1} - \alpha_0 \end{bmatrix} \tag{2.14}$$

the solution for the resonance amplitude can be accessed,

$$\begin{bmatrix} a_{-1} \\ a_0 \\ a_{+1} \end{bmatrix} = \boldsymbol{W}^{-1} \begin{bmatrix} \chi_{1,+1} \\ \kappa_1 + \chi_{1,0} \\ \chi_{1,-1} \end{bmatrix} \tag{2.15}$$

Now we focus on the variation of Eq (2.4), considering only the transmission $\boldsymbol{s}_{2+} = \sum_n s_{2+,n} e^{j(\omega+n\Omega)t}$

$$\sum_n s_{2+,n} e^{j(\omega+n\Omega)t} = \sum_n a_n e^{j(\omega+n\Omega)t} \left(\kappa_2 + \sum_p \chi_{2,p} e^{jp\Omega t} \right) \tag{2.16}$$

Appling similar algebraic manipulations as above, one can get the solutions for $\boldsymbol{s}_{2+}$

$$s_{2+,n} = \kappa_2 a_n + \sum_{n'} \chi_{2,n-n'} a_{n'} \tag{2.17}$$

The term $\boldsymbol{\chi}$ is similar to the coupling constants, having no direct relation to any physical properties. It is a challenge to implement such a method in some time-varying systems where $\boldsymbol{\chi}$ is not zero. The above process can also be done in the perturbation method[18].

Till now, we only present the TCMT model in a single resonator for single resonance mode. As for the systems with two coupled resonators, the complexity of the model increases. Unlike TMM, TCMT considers every resonator with an independent resonance mode and must couple them together. So, in the TCMT for two coupled resonators, both resonators are involved in the algebraic process. One can consult the work of Suh[16] for further demonstration of TCMT on the bi-resonator systems. Additionally, Shen et al.[19] used TCMT on time-modulated bi-resonator systems, and Chegnizadeh et al.[18] did the same with the perturbation method.

On the other hand, since in TCMT many factors are only accessible via fitting with numerical or experimental results, we do not think it is helpful for us to explore the nature and origin of some unexpected phenomenon in our work. Despite the fact that it is a very practical method to analytically model a system with coupled resonators, we only focus on working with the TMM.

III.2. Transfer matrix method (TMM)

The TMM is one of the most powerful methods in contemporary theoretical research. It yields accurate solutions for the one-dimensional models and allows calculating the a good approximation of the solution. Compared with TCMT, the TMM works on a large band of frequency and directly takes the physical properties as parameters. In the scenarios with multiple partitions (resonators), with TMM, one can still analyze each partition separately, and the transfer matrices corresponding to each partition are combined to get the final matrix describing the whole system. Inspired from the work of Chegnizadeh et al.[18] and Zhu et al.[4], we developed our own featured TMM for finite time-modulated resonators system with PWE.

According to whether the dimension of the resonator is considered, two scenarios of the TMM are categorized here, which are explained in **Fig. 2.2**. For example, the dimension of FP resonator is normally not negligible while the dimension of membrane (thickness) is ignored (**Fig. 2.2(a)**). These cases are separated into two scenarios, because the dispersion relation in a time-modulated resonator is different from the waveguide medium, once the dimension of this part is considered, there will be a complex coupling between the two kinds of dispersions.

Since we can analyze each resonator separately in the TMM, and the TMM of each part can be assembled easily, we only discuss the cases with single resonator in the following part. For the TMM of time-varying acoustic medium, please read the theoretical part in Chapter 3 for a detailed demonstration. Here, let us first consider an elastic beam with single FP resonator for longitudinal wave propagation, in which the Young's modulus and density vary harmonically in time with an initial modulation phase ($E = E_r + E^M \cos(\Omega t + \phi)$ and $\rho = \rho_r + \rho^M \cos(\Omega t + \phi)$), as shown in **Fig. 2.2(a)**. We impose the conservation of linear momentum along axial direction and the continuity law for the cross section of the beam to get the following motion equation in the FP resonator for longitudinal waves,

$$\frac{\partial}{\partial x}\left[E(t)\frac{\partial u(x,t)}{\partial x}\right] - \frac{\partial}{\partial t}\left[\rho(t)\frac{\partial u(x,t)}{\partial t}\right] = 0 \qquad (2.18)$$

The time-varying Young's modulus and density can be written in Floquet form,

$$E(t) = \sum_{m=-\infty}^{+\infty} E_m e^{jm\Omega t} e^{j\phi_m} \tag{2.19}$$

$$\rho(t) = \sum_{m=-\infty}^{+\infty} \rho_m e^{jm\Omega t} e^{j\phi_m} \tag{2.20}$$

in which $E_0 = E_r$, $\rho_0 = \rho_r$, $E_{\pm 1} = 0.5E^M$, $\rho_{\pm 1} = 0.5\rho^M$, $\phi_{\pm 1} = \pm\phi$, and Ω is the modulation angular frequency. Accordingly, the general solutions for the displacement have a Floquet form,

$$u(x,t) = \sum_{n=-\infty}^{+\infty} u_n(x) e^{j(\omega+n\Omega)t} \tag{2.21}$$

ω is the operational angular frequency. Now we substitute the Eq (2.19) - (2.21) into Eq (2.18),

$$\sum_{n,m} \frac{\partial^2 u_n(x)}{\partial x^2} E_m e^{j[\omega+(n+m)\Omega]t} e^{j\phi_m} + \sum_{n,m} m\Omega(\omega + n\Omega) u_n(x) \rho_m e^{j[\omega+(n+m)\Omega]t} e^{j\phi_m}$$

$$+ \sum_{n,m} (\omega + n\Omega)(\omega + n\Omega) u_n(x) \rho_m e^{j[\omega+(n+m)\Omega]t} e^{j\phi_m} = 0 \tag{2.22}$$

By replacing the index script m with $n - n'$, we can develop Eq (2.22) into the following equation,

$$\sum_{n,n'} \frac{\partial^2 u_n(x)}{\partial x^2} E_{n'-n} e^{j(\omega+n'\Omega)t} e^{j\phi_{n'-n}} +$$

$$\sum_{n,n'} (\omega + n'\Omega)(\omega + n\Omega) u_n(x) \rho_{n'-n} e^{j(\omega+n'\Omega)t} e^{j\phi_{n'-n}} = 0 \tag{2.23}$$

Applying the orthogonality of $\left(e^{jn\Omega t}\right)_n$, we eliminate the time terms,

$$\sum_{n'} \frac{\partial^2 u_{n'}(x)}{\partial x^2} E_{n-n'} e^{j\phi_{n-n'}} + \sum_{n'} (\omega + n'\Omega)(\omega + n\Omega) u_{n'}(x) \rho_{n-n'} e^{j\phi_{n-n'}} = 0 \tag{2.24}$$

The above linear partial differential equation (LPDE) can be written in the vectorial form. We only show $n-1$, n and $n+1$ orders for simplification,

$$\begin{bmatrix} H_0 & H_{-1} & 0 \\ H_{+1} & H_0 & H_{-1} \\ 0 & H_{+1} & H_0 \end{bmatrix} \frac{\partial^2}{\partial x^2} \begin{bmatrix} u_{n-1} \\ u_n \\ u_{n+1} \end{bmatrix} +$$

$$\begin{bmatrix} W_{n-1}W_n\Lambda_0 & W_{n-1}W_{n+1}\Lambda_{-1} & 0 \\ W_nW_{n-1}\Lambda_{+1} & W_nW_n\Lambda_0 & W_nW_{n+1}\Lambda_{-1} \\ 0 & W_{n+1}W_{n-1}\Lambda_{+1} & W_{n+1}W_n\Lambda_0 \end{bmatrix} \begin{bmatrix} u_{n-1} \\ u_n \\ u_{n+1} \end{bmatrix} = 0 \tag{2.25}$$

in which $H_i = E_i e^{j\phi_i}$, $\Lambda_i = (\omega + n'\Omega)\rho_i e^{j\phi_i}$, and $W_i = (\omega + i\Omega)$. We find that the first order terms are absent in this series of LPDEs, and only the second orders and the zeroth orders exist, so we are sure that it has pairs of conjugated complex roots. We generalize the Eq (2.25) to $-N, \ldots, +N$ orders, then solve the equations,

$$[\boldsymbol{u}^N] = \sum_{i=-N}^{+N} C_i^- \boldsymbol{V}_i^- e^{-\lambda_i^-(x-x_0)} + \sum_{i=-N}^{+N} C_i^+ \boldsymbol{V}_i^+ e^{-\lambda_i^+(x-x_0)} \tag{2.26}$$

where $\boldsymbol{u}^N = \langle u_{-N}, \ldots, u_0, \ldots, u_N \rangle^T$, $\boldsymbol{V}_i^{\pm}$ and $\lambda_i^{\pm}$ are the i^{th} eigenvector and eigenvalue of the series of LPDEs, corresponding to forward and backward wave propagation. $C_i^{\pm}$ correspond to the i^{th} order harmonic wave amplitudes of forward and backward wave propagation. x_0 is the left boundary coordinate of the local FP resonator. By some simple mathematic manipulations (see the theoretical parts in Chapter 3), we can obtain the transfer matrix representing the transfer from partition s to partition $s+1$ from the above results,

$$\boldsymbol{M}_{s\to s+1} = \langle \boldsymbol{V}_{s+1}^+ | \boldsymbol{V}_{s+1}^- \rangle^{-1} \langle \boldsymbol{V}_s^+ | \boldsymbol{V}_s^- \rangle \begin{bmatrix} \boldsymbol{H}_s & \boldsymbol{O} \\ \boldsymbol{O} & {\boldsymbol{H}_s}^{-1} \end{bmatrix} \tag{2.27}$$

where $\boldsymbol{H}_s = \begin{bmatrix} \boldsymbol{H}_s^+ & \boldsymbol{O} \\ \boldsymbol{O} & \boldsymbol{H}_s^- \end{bmatrix}$, $\boldsymbol{H}_{s,(n,n')}^{\pm} = e^{-\lambda_{s,n-N-1}^{\pm}(x_{s+1,0}-x_{s,0})}\delta_{n-n'}$, $\boldsymbol{V}_s^{\pm} = \langle \boldsymbol{V}_{s,-N}^{\pm}, \ldots, \boldsymbol{V}_{s,0}^{\pm}, \ldots, \boldsymbol{V}_{s,N}^{\pm} \rangle$ and $\boldsymbol{C}_s^{\pm} = \left\langle C_{s,-N}^{\pm}, \ldots, C_{s,0}^{\pm}, \ldots, C_{s,N}^{\pm} \right\rangle^T$. $x_{s+1,0} - x_{s,0}$ represents the dimension of the partition s. $\boldsymbol{O}$ is the zero matrix. A typical result of this kind of system (at one resonance frequency) is shown in **Fig. 2.2(c)**.

The above equations give the solution for a harmonic time-modulated resonator for longitudinal wave propagations. The corresponding solutions for acoustic waves (see Chapter 3) and flexural waves are a little different, in which the former one has first order LPDEs and the latter one involves fourth order LPDEs.

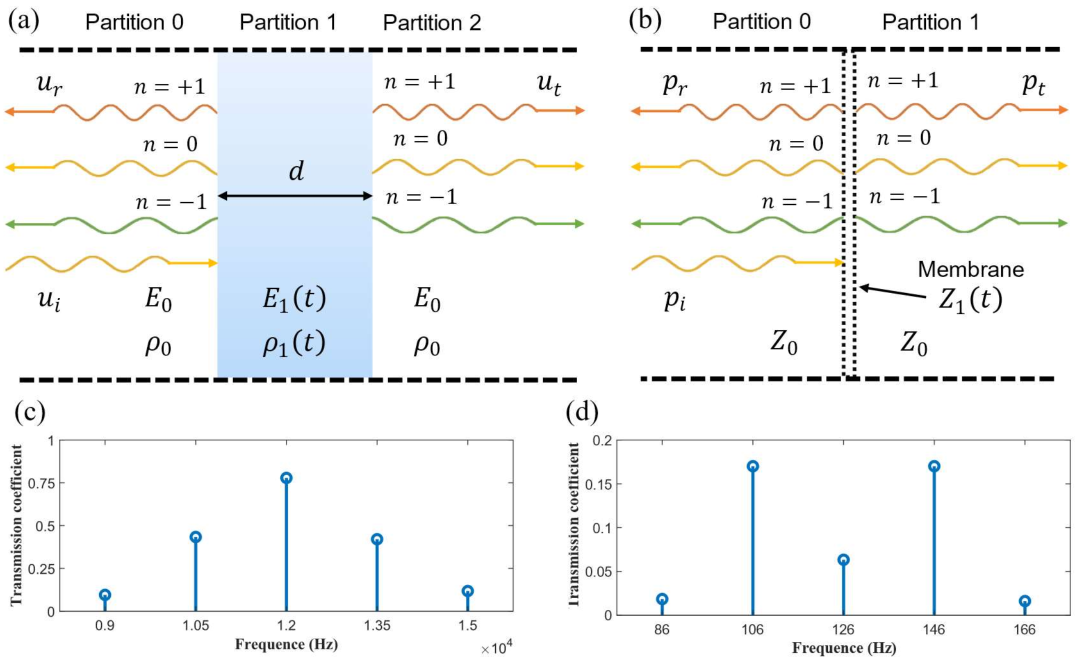

FIG. 2.2. (a) Time-modulated elastic beam with single FP resonator for longitudinal wave propagation. Young's modulus and density vary in time. (b) Single membrane with time-modulated impedance being planted in an air waveguide. A 'partition' indicates a part whose dimension must be taken into account. (c) A TMM result of the system shown in (a). (d) A TMM result of the system shown in (b).

Having described the TMM for the coupled FP resonators, we will then express the transfer matrix for the case of waveguide with a membrane. We consider a membrane with time-modulated tension being implanted in an air waveguide, as shown in **Fig. 2.2(b)**. Let us directly consider the pressure and the particle velocity in the Floquet formulation,

$$p(x,t) = \sum_{n=-\infty}^{+\infty} p_n(x) e^{j(\omega+n\Omega)t} \tag{2.28}$$

$$v(x,t) = \sum_{n=-\infty}^{+\infty} v_n(x) e^{j(\omega+n\Omega)t} \tag{2.29}$$

The dispersion relation in the waveguide part is $k = \omega/c$, where c is the sound speed. Also, the above pressure field and velocity verify the governing equation $\rho_0 \partial_t v = -\partial_x p$, where ρ_0 is air density.

In this scenario, the effect of the membrane resonator is implied in the continuity conditions on the level of equations. The velocity continuity is trivial at $x = 0$ where the membrane is located at x=0,

$$v^+(0,t) = v^-(0,t) \tag{2.30}$$

in which the + and – signs indicate the left and right sides of the membrane. Then the pressure continuity yields,

$$p^+(0,t) = p^-(0,t) + Z^M(t)v^-(0,t) \tag{2.31}$$

Where $Z^M(t)$ is the time-varying impedance of the membrane, as a result of its time-modulated tension. Let us write the $Z^M(t)$ directly in the Floquet decomposition form with the modulation angular frequency Ω in the case of a harmonic time modulation,

$$Z^M(t) = \sum_{m=-\infty}^{+\infty} Z_m e^{jm\Omega t} e^{j\phi_m} \tag{2.32}$$

As usual, if we consider only the first-order Fourier expansion of Z^M, $Z_m = 0$ and $\phi_m = 0$ in case of $|m| > 1$. Now substituting the Floquet form of Z^M, p and v into the continuity conditions (2.30) and (2.31),

$$\sum_{n=-\infty}^{+\infty} v_n^+(0)e^{j(\omega+n\Omega)t} = \sum_{n=-\infty}^{+\infty} v_n^-(0)e^{j(\omega+n\Omega)t} \tag{2.33}$$

$$\sum_{n=-\infty}^{+\infty} p_n^+(0)e^{j(\omega+n\Omega)t} = \sum_{n=-\infty}^{+\infty} p_n^-(0)e^{j(\omega+n\Omega)t} +$$

$$\sum_{m=-\infty}^{+\infty} Z_m e^{jm\Omega t} e^{j\phi_m} \sum_{n=-\infty}^{+\infty} v_n^-(0)e^{j(\omega+n\Omega)t} \tag{2.34}$$

Utilizing the orthogonality of $\left(e^{jn\Omega t}\right)_n$ and index replacements,

$$v_n^+(0) = v_n^-(0) \tag{2.35}$$

$$p_n^+(0) = p_n^-(0) + \sum_{n'} Z_{n-n'} v_{n'}^-(0)e^{j\phi_{n-n'}} \tag{2.36}$$

Now we detail the sub-components of pressure field, taking the forward and backward waves into account,

$$p_n^+(x) = A_n e^{-jk_n x} + B_n e^{jk_n x} \tag{2.37}$$

$$p_n^-(x) = C_n e^{-jk_n x} + D_n e^{jk_n x}$$

Along with the relation between v and p, Eqs (2.35) and (2.36) can be developed into,

$$A_n - B_n = C_n - D_n \tag{2.38}$$

$$A_n + B_n = C_n + D_n + \sum_{n'} \frac{Z_{n-n'}}{Z_0}(C_{n'} - D_{n'})e^{j\phi_{n-n'}} \tag{2.39}$$

Then, reformulating the above equations and rewriting them into a vectorial form by only showing $n-1$, n and $n+1$ orders for simplification, we have,

$$\begin{bmatrix} 1 & 0 & 0 & -1 & 0 & 0 \\ 0 & 1 & 0 & 0 & -1 & 0 \\ 0 & 0 & 1 & 0 & 0 & -1 \\ 1 & 0 & 0 & 1 & 0 & 0 \\ 0 & 1 & 0 & 0 & 1 & 0 \\ 0 & 0 & 1 & 0 & 0 & 1 \end{bmatrix} \begin{bmatrix} A_{n-1} \\ A_n \\ A_{n+1} \\ B_{n-1} \\ B_n \\ B_{n+1} \end{bmatrix} =$$

$$\begin{bmatrix} 1 & 0 & 0 & -1 & 0 & 0 \\ 0 & 1 & 0 & 0 & -1 & 0 \\ 0 & 0 & 1 & 0 & 0 & -1 \\ 1+\xi_0 & +\xi_{-1} & 0 & 1-\xi_0 & -\xi_{-1} & 0 \\ +\xi_{+1} & 1+\xi_0 & +\xi_{-1} & -\xi_{+1} & 1-\xi_0 & -\xi_{-1} \\ 0 & +\xi_{+1} & 1+\xi_0 & 0 & -\xi_{+1} & 1-\xi_0 \end{bmatrix} \begin{bmatrix} C_{n-1} \\ C_n \\ C_{n+1} \\ D_{n-1} \\ D_n \\ D_{n+1} \end{bmatrix} \tag{2.40}$$

where $\xi_i = \frac{Z_i}{Z_0} e^{j\phi_i}$. Finally, we get the matrix $\boldsymbol{M}$ linking the waves amplitudes between the left and right sides of the time-varying membrane,

$$\boldsymbol{M} = \begin{bmatrix} 1 & 0 & 0 & -1 & 0 & 0 \\ 0 & 1 & 0 & 0 & -1 & 0 \\ 0 & 0 & 1 & 0 & 0 & -1 \\ 1+\xi_0 & +\xi_{-1} & 0 & 1-\xi_0 & -\xi_{-1} & 0 \\ +\xi_{+1} & 1+\xi_0 & +\xi_{-1} & -\xi_{+1} & 1-\xi_0 & -\xi_{-1} \\ 0 & +\xi_{+1} & 1+\xi_0 & 0 & -\xi_{+1} & 1-\xi_0 \end{bmatrix}^{-1}$$

$$\times \begin{bmatrix} 1 & 0 & 0 & -1 & 0 & 0 \\ 0 & 1 & 0 & 0 & -1 & 0 \\ 0 & 0 & 1 & 0 & 0 & -1 \\ 1 & 0 & 0 & 1 & 0 & 0 \\ 0 & 1 & 0 & 0 & 1 & 0 \\ 0 & 0 & 1 & 0 & 0 & 1 \end{bmatrix} \tag{2.41}$$

A typical result example of this kind of system (at one resonance frequency) is shown in **Fig. 2.2(d)**. We can clearly see the generation of high order harmonics from the incident wave excitation at the fundamental frequency.

III.3. Quadratic eigenvalue problem (QEP) solving

The quadratic eigenvalue problem (QEP) is a practical formulation to solve the dispersion relation in STM systems in which the variation is continuous in space[9,20]. In some cases where this variation is not spatially continuous, researchers could consider it as continuous for simplification purpose, like the work of Shen et al.[8]. Considering a beam with Young's modulus E and density ρ as periodic functions of space and time (**Fig. 2.3(a)**), we start from the equation of motion (Eq (2.18)) for longitudinal waves. The space-time-varying Young's modulus and density can be written in Floquet-Bloch form,

$$E(t) = \sum_{m=-\infty}^{+\infty} E_m e^{jm(\Omega t - Kx)} \tag{2.42}$$

$$\rho(t) = \sum_{m=-\infty}^{+\infty} \rho_m e^{jm(\Omega t - Kx)} \tag{2.43}$$

Accordingly, the general solution for the displacement also has a Floquet-Bloch form,

$$u(x,t) = e^{j(\omega t - \quad)} \sum_{n=-\infty}^{+\infty} u_n e^{jn(\Omega t - Kx)} \tag{2.44}$$

Substituting Eq (2.44) into Eq (2.18), together with the Floquet-Bloch form for the material properties in Eq (2.42) and Eq (2.43),

$$\begin{aligned} &\sum_{n,m} (k + nK)[k + (n+m)K]\, E_m u_n e^{j[\omega + (n+m)\Omega t] - j[k + (n+m)K]x} \\ &= \sum_{n,m} (\omega + n\Omega)[\omega + (n+m)\Omega]\, \rho_m u_n e^{j[\omega + (n+m)\Omega t] - j[k + (n+m)K]x} \end{aligned} \tag{2.45}$$

Now we simplify the above equation by exploiting orthogonality of the Fourier basis in Eq (2.18) and sub-index changing,

$$\sum_{p} (k + nK)(k + pK)\, E_{n-p} u_p = \sum_{p} (\omega + n\Omega)(\omega + p\Omega)\, \rho_{n-p} u_p \tag{2.46}$$

Having the equation holding for longitudinal motion of the beam, we consider a finite number of terms (from $-N$ to N) in Eq (2.44). Then, Eq (2.46) represents a finite series of $2N+1$ equations. We then write those equations in the vectorial form (only $n-1$, n and $n+1$ orders are considered here for simplification purpose),

$$\begin{bmatrix} A_{n-1}A_nE_0 & A_{n-1}A_{n+1}E_{-1} & A_{n-1}A_{n+2}E_{-2} \\ A_nA_{n-1}E_{+1} & A_nA_nE_0 & A_nA_{n+1}E_{-1} \\ A_{n+1}A_{n-2}E_{+2} & A_{n+1}A_{n-1}E_{+1} & A_{n+1}A_nE_0 \end{bmatrix} \begin{bmatrix} u_{n-1} \\ u_n \\ u_{n+1} \end{bmatrix} =$$

$$\mathit{\Omega}^2 \begin{bmatrix} (n-1)n\rho_0 & (n-1)(n+1)\rho_{-1} & (n-1)(n+2)\rho_{-2} \\ n(n-1)\rho_{+1} & nn\rho_0 & n(n+1)\rho_{-1} \\ (n+1)(n-2)\rho_{+2} & (n+1)(n-1)\rho_{+1} & (n+1)n\rho_0 \end{bmatrix} \begin{bmatrix} u_{n-1} \\ u_n \\ u_{n+1} \end{bmatrix}$$

$$+\omega\mathit{\Omega} \begin{bmatrix} (2n-1)\rho_0 & 2n\rho_{-1} & (2n+1)\rho_{-2} \\ (2n-1)\rho_{+1} & 2n\rho_0 & (2n+1)\rho_{-1} \\ (2n-1)\rho_{+2} & 2n\rho_{+1} & (2n+1)n\rho_0 \end{bmatrix} \begin{bmatrix} u_{n-1} \\ u_n \\ u_{n+1} \end{bmatrix}$$

$$+\omega^2 \begin{bmatrix} \rho_0 & \rho_{-1} & \rho_{-2} \\ \rho_{+1} & \rho_0 & \rho_{-1} \\ \rho_{+2} & \rho_{+1} & \rho_0 \end{bmatrix} \begin{bmatrix} u_{n-1} \\ u_n \\ u_{n+1} \end{bmatrix} \tag{2.47}$$

in which $A_i = (k + iK)$. In the work of Chen et al.[8], the perturbation method is applied. The above equation can be cast in the QEP form,

$$(\omega^2\boldsymbol{L}_2 + \omega\boldsymbol{L}_1 + \boldsymbol{L}_0)\boldsymbol{u} = \boldsymbol{0}\,, \tag{2.48}$$

where $L_{2,m,n} = \rho_{m-n}$, $L_{1,m,n} = (m+n)\rho_{m-n}\mathit{\Omega}$, and $L_{0,m,n} = mn\rho_{m-n}\mathit{\Omega}^2 - A_mA_nE_{m-n}$. The solutions for ω are the eigenvalues of the above quadratic problem. By varying the k in a specific range then solving the corresponding ω for each variance of k, we can plot the dispersion diagram. For structure being only periodic in space, this range is given by the irreducible Brillouin zone (IBZ)[21], while the classical definition of the IBZ does not adapt to spatiotemporal modulation, so we enlarge the wavenumber range ($2\pi k/K \in \left[-\frac{3\pi}{2}, \frac{3\pi}{2}\right]$). We show an example result in **Fig. 2.3(b)**, in which the STM of the Young's modulus and density are cosine functions (±1 orders in the Floquet-Bloch form). Directional bandgaps are clear observed in the dispersion diagram.

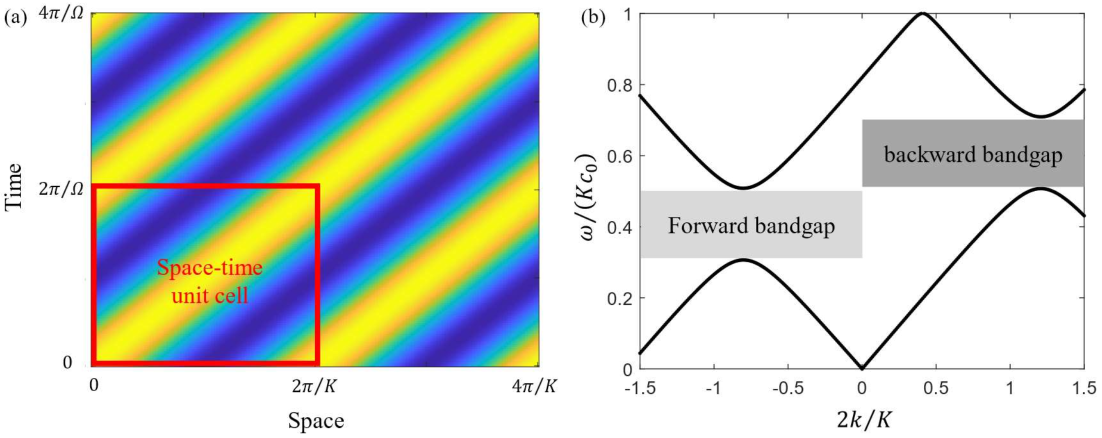

FIG. 2.3. (a) Spatiotemporal modulation of Young's modulus and of density (cosine function) of a beam. Ω is the modulation frequency, and K is the modulation wave number. The region marked by red rectangular is seen as a space-time unit cell. (b) The dispersion diagram of the beam in (a) obtained by solving QEPs.

IV. Conclusion

In this chapter, we introduce the mainstream numerical and analytical approaches appearing in the research on STM and nonreciprocal metamaterials based on moving media. We give the detailed Fourier-decomposition-based demonstration equations for temporal coupled-mode theory, transfer matrix method, and quadratic eigenvalue problem solving with simplified application scenarios.

To summarize, the QEP can only solve the dispersion relationship in the periodic system. The TCMT is mostly adoptable in finite systems, but the mode coupling process is complicated, and some key factors are only available by fitting. Similarly adoptable in most finite system, TMM is have less limitations and preferred in our research.

References

[1] H. Nassar, B. Yousefzadeh, R. Fleury, M. Ruzzene, A. Alù, C. Daraio, A.N. Norris, G. Huang, and M.R. Haberman, Nat. Rev. Mater. **5**, 667 (2020).

[2] Y. Zhu, L. Cao, A. Merkel, S.-W. Fan, B. Vincent, and B. Assouar, Nat. Commun. **12**, 7089 (2021).

[3] R. Fleury, D.L. Sounas, C.F. Sieck, M.R. Haberman, and A. Alù, Science **343**, 516 (2014).

[4] X. Zhu, J. Li, C. Shen, X. Peng, A. Song, L. Li, and S.A. Cummer, Appl. Phys. Lett. **116**, 034101 (2020).

[5] Q. Wu, H. Chen, H. Nassar, and G. Huang, J. Mech. Phys. Solids **146**, 104196 (2021).

[6] B.M. Goldsberry, S.P. Wallen, and M.R. Haberman, Phys. Rev. B **102**, 014312 (2020).

[7] C. Shen, X. Zhu, J. Li, and S.A. Cummer, Phys. Rev. B **100**, 054302 (2019).

[8] Y. Chen, X. Li, H. Nassar, A.N. Norris, C. Daraio, and G. Huang, Phys. Rev. Appl. **11**, 064052 (2019).

[9] J. Li, C. Shen, X. Zhu, Y. Xie, and S.A. Cummer, Phys. Rev. B **99**, 144311 (2019).

[10] J. Reddy, *Introduction to the Finite Element Method 4E*, (McGraw Hill, New York, NY, 2018).

[11] T.W. Wu and M. Ochmann, J. Acoust. Soc. Am. **111**, 1507 (2002).

[12] K. Yee, IEEE Trans. Antennas Propag. **14**, 302 (1966).

[13] B. Finkelstein and R. Kastner, J. Comput. Phys. **221**, 422 (2007).

[14] C. Shen, J. Li, Z. Jia, Y. Xie, and S.A. Cummer, Phys. Rev. B **99**, 134306 (2019).

[15] S. Fan, W. Suh, and J.D. Joannopoulos, JOSA A **20**, 569 (2003).

[16] W. Suh, Z. Wang, and S. Fan, IEEE J. Quantum Electron. **40**, 1511 (2004).

[17] Hermann A. Haus, *Waves And Fields In Optoelectronics* (1984).

[18] M. Chegnizadeh, M. Memarian, and K. Mehrany, JOSA B **37**, 88 (2020).

[19] C. Shen, Phys. Rev. B **100**, (2019).

[20] G. Trainiti and M. Ruzzene, New J. Phys. **18**, 083047 (2016).

[21] Leon Brillouin, *Wave Propagation In Periodic Structures Electric Filters And Crystal Lattices First Edition* (1946).

Chapter 3

Nonreciprocal acoustic metamaterials based on cascaded time-modulated Fabry-Pérot resonator

Contents

I. Introduction

In most of the works applied to classical waves and especially in acoustics, the physics of nonreciprocity is based on shifting the Bragg bandgap in the frequency domain for opposite directions to prohibit wave propagation unidirectionally[1–3]. This mechanism was achieved by space-time modulating the effective properties of the constituent materials (stiffness) along several periods of the structure (at least 10 periods). Consequently, the periodic parts of the system have to be precisely synchronized which makes the experimental realization quite challenging, and thus limit the practicability of the device. For instance, in acoustics, although dynamically changing the effective density of air is locally possible[4], a precise harmonic modulation in both space and time along several periods remains challenging. Besides, systems such as coupled modulated Helmholtz resonators[5], air cavities[6], membranes[7], and even Fabry–Perot based photonic slabs[8] inspired us for a simple design compared to the aforementioned systems. For instance, Shen et al.[5] showed that using two cascaded time-modulated Helmholtz resonators (HR), nonreciprocal wave behavior can be realized via frequency conversion with high order modes occcuring differently in positive and negative propagation. However, nonreciprocity is obtained far from the resonance frequency of the HR as the wave is completely reflected at this frequency. Under this restriction, the fundamental mode with the frequency of the incident wave is always accompanied with considerable high order modes in the transmission whatever the direction of propagation is. Nevertheless, the choice of cascaded slabs is more advantageous since it allows high wave transmission at the Fabry–Perot resonance. Consequently, the slab-based-system has the potential to create the situation of unidirectional wave conversion, for instance, hence offering more control over nonreciprocity via mode conversion.

According to these existing nonreciprocal bi-resonator structures in optics[8], acoustics and elastodynamics[5–7], we summarize the following characteristics in common: first, the initial phases of the temporal modulations applied on the two resonators are different, and this difference is usually exactly $\pi/2$ or some other approximate values, pursuing the highest level of spatial asymmetry in the system. Second, a Fabry-Perot (FP) resonance is in fact generated over the two resonators with the inter waveguide, and this resonance is usually coupled with the two resonators. In this work, we demonstrated nonreciprocal acoustic transmission in a finite system based on coupled Fabry-Perot resonators with temporal modulation on their effective properties. A good nonreciprocity is obtained in our system with a quasi-lossless transmission in one direction and a nearly-zero transmission of the fundamental mode in opposite direction. In contrast to the previous works that used Bragg band gap combined with modulating the effective properties of the materials along several periods of the structure, our system is composed of two coupled fluid slabs that behave as coupled Fabry-Perot (FP) resonators whose density, however, is time modulated. A spatial bias is introduced by forcing a phase difference on the time modulated density between the two slabs. This kind of modulation could be easily achieved by periodically compressing the fluid for instance[4,9]. In such design, the physical mechanism is mainly based on frequency conversion where the acoustic energy is transferred from the fundamental mode into higher order ones [10,11].

The Fourier decomposition method[12] is first adopted to construct the scattering matrix describing the system, which analytically solves the acoustic transmission. The analytical result matches perfectly with the finite-element-method (FEM) simulation results. Then, we took advantage of this model to seek for parameters and configurations that yield a good nonreciprocity. Furthermore, under the premise of high nonreciprocity, we also discussed the possibility of unidirectional frequency conversion. The latter is an important wave phenomenon that enables generating waves at desired frequencies from an incident wave at different frequencies. Recently, the application of frequency conversion is expanded to acoustic domain, such as directional loudspeakers and nondestructive evaluation[13,14].

II. Design and theory

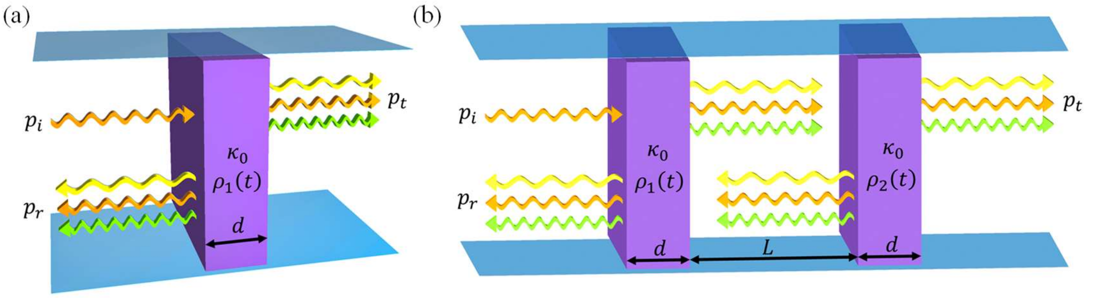

FIG. 3.1. Schematic of a single-slab (a) system and a two-cascaded-slab (b) system with time modulated effectives densities. Harmonics appear in the transmitted and reflected waves due to the modulation.

We first considered an adiabatic single slab resonator as shown in **Fig. 3.1**. The background medium is air, whose density is ρ_0 and sound speed is c_0, with bulk modulus $\kappa_0 = \rho_0 {c_0}^2$. The thickness of the slab resonator is d. The medium of the slab resonator is a fluid whose density is different from that of air. In this model, we assume that the density of the slab can be modulated in time: $\rho = \delta[\rho_0 + \rho^M \cos(\Omega t + \phi)]$, where $\rho^M = 2M\rho_0$. In the static state, it can be understood as air in the slab resonator being compressed δ times. As we consider the constant bulk modulus throughout this study ($\kappa_0 = 141.2kPa$), the sound speed in the slab resonator is consequently modulated as $c = \sqrt{\kappa_0/\rho}$. In the static state, the sound speed in the slab resonator is $c^\delta = c_0/\sqrt{\delta}$.

In practice, this kind of modulation can for instance be achieved by driving a piston with rotating elements to induce varying compression in time. Here, δ is the static density ratio, M is the modulation depth, Ω is the angular frequency of modulation, and ϕ is the initial phase of the modulation. Considering a forward incident wave at the angular frequency ω, and using the Floquet-Bloch theorem, the acoustic pressure and the particle velocity fields in the slab yield,

$$p(x,t) = \sum_{n=-\infty}^{+\infty} p_n(x) e^{j(\omega + n\Omega)t} \tag{3.1}$$

$$v(x,t) = \sum_{n=-\infty}^{+\infty} v_n(x) e^{j(\omega + n\Omega)t} \tag{3.2}$$

where $p_n(x)$ and $v_n(x)$ are the Fourier components of the pressure and velocity, respectively, in the time domain for both forward and backward propagating waves. The time modulated density can be rewritten in the same way,

$$\rho(t) = \delta \sum_{m=-\infty}^{+\infty} \rho_m e^{jm\Omega t} e^{j\phi_m} \tag{3.3}$$

According to the adopted harmonic modulation for slab medium density, we have here $\rho_{\pm 1} = 0.5\rho^M$, and $\rho_m = 0$ for $m \neq 0, \pm 1$, $\phi_1 = \phi$ and $\phi_{-1} = -\phi$. By substituting Eqs. (3.2) and (3.3) into the known acoustic equation $\partial_x p = -\rho(t)\partial_t v$, we get the following relation,

$$\frac{\partial p(x,t)}{\partial x} = -\delta \sum_{m=-\infty}^{+\infty} \rho_m e^{jm\Omega t} e^{j\phi_m} \sum_{n'=-\infty}^{+\infty} j(\omega + n'\Omega) v_{n'}(x)\, e^{j(\omega+n'\Omega)t} \tag{3.4}$$

Then we develop Eq. (3.4) by combining the two summations,

$$\frac{\partial p(x,t)}{\partial x} = -j\delta \sum_{n',m} (\omega + n'\Omega)\rho_m v_{n'}(x) e^{j[\omega+(n'+m)\Omega]t} e^{j\phi_m} \tag{3.5}$$

By eliminating the index script m by replacing it with $n - n'$, we can develop Eq. (3.5) into the following equation,

$$\frac{\partial p(x,t)}{\partial x} = -j\delta \sum_{n',n} (\omega + n'\Omega)\rho_{n-n'} v_{n'}(x) e^{j\phi_{n-n'}} e^{j(\omega+n\Omega)t} \tag{3.6}$$

By substituting Eq. (3.1) into Eq. (3.6) and using the orthogonality of $\left(e^{jn\Omega t}\right)_n$, we have,

$$\frac{\partial p_n(x)}{\partial x} = -j\delta \sum_{n'} (\omega + n'\Omega)\rho_{n-n'} e^{j\phi_{n-n'}} v_{n'}(x) \tag{3.7}$$

So that the time dependent term $e^{j\omega t}$ is eliminated. Substituting Eqs. (3.1) and (3.2) into the known acoustic equation $\partial_x v = -\kappa_0^{-1}\, \partial_t p$, we get,

$$\sum_{n=-\infty}^{+\infty} \frac{\partial v_n(x)}{\partial x} e^{j(\omega+n\Omega)t} = -\frac{1}{\kappa_0} \sum_{n=-\infty}^{+\infty} j(\omega + n\Omega) p_n(x) e^{j(\omega+n\Omega)t} \tag{3.8}$$

Using the orthogonality of $\left(e^{jn\Omega t}\right)_n$ again, we have,

$$\frac{\partial v_n(x)}{\partial x} = -j(\omega + n\Omega)\frac{1}{\kappa_0}p_n(x) \tag{3.9}$$

After further developments by defining a new variable $\xi = x\Omega/c_s$, where c_s is the speed of sound in layer s and in the slab c_s equals c^δ, Eq. (3.7) and (3.9) become,

$$\frac{\partial p_n(\xi)}{\partial \xi} = -jZ^\delta \sum_{n'} \left(\frac{\omega}{\Omega} + n'\right) \tilde{\rho}_{n-n'} e^{j\phi_{n-n'}} v_{n'}(\xi) \tag{3.10}$$

$$\frac{\partial v_n(\xi)}{\partial \xi} = -j\frac{1}{Z^\delta}\left(\frac{\omega}{\Omega} + n\right)p_n(\xi) \tag{3.11}$$

where $Z^\delta = \delta\rho_0 c^\delta$ is the static impedance in the slab and $\tilde{\rho}_{n-n'} = \rho_{n-n'}/\rho_0$.

Thus, a series of first order partial differential equations is constructed based on Eqs. (3.10) and (3.11), which depends on the number of decompositions N we adopt to approximate the solution,

$$\boldsymbol{A}_s \cdot \begin{bmatrix} \boldsymbol{p}^N \\ \boldsymbol{v}^N \end{bmatrix}_s - \boldsymbol{I} \cdot \partial_\xi \begin{bmatrix} \boldsymbol{p}^N \\ \boldsymbol{v}^N \end{bmatrix}_s = 0 \tag{3.12}$$

where $\boldsymbol{p}^N = \langle p_{-N}, \dots, p_0, \dots, p_N \rangle^T$, $\boldsymbol{v}^N = \langle v_{-N}, \dots, v_0, \dots, v_N \rangle^T$, $\boldsymbol{A}_s = \begin{bmatrix} 0 & \boldsymbol{A}_s^p \\ \boldsymbol{A}_s^v & 0 \end{bmatrix}$, $\boldsymbol{I}$ is the identity matrix and the subscript s indicates the domain index. For example, in **Fig. 3.2**, $s = 1$ refers to the slab resonator and $s = 2$ refers to the next air medium in contact. $\boldsymbol{A}_s^p$ and $\boldsymbol{A}_s^v$ are both square matrices with size $2N + 1$,

$$\boldsymbol{A}_{s,(n,n')}^p = -jZ^\delta \left(\frac{\omega}{\Omega} + n'\right) \tilde{\rho}_{n-n'} e^{j\phi_{n-n'}} \tag{3.13}$$

$$\boldsymbol{A}_{s,(n,n')}^v = -j\frac{1}{Z^\delta}\left(\frac{\omega}{\Omega} + n\right) K_{n-n'} \tag{3.14}$$

where $K_{n-n'}$ is the Kronecker function. As $\boldsymbol{A}_s$ is not function of ξ, Eqs. (3.12) have a solution in this form,

$$\begin{bmatrix} \boldsymbol{p}^N \\ \boldsymbol{v}^N \end{bmatrix}_s = \sum_{i=-N}^{+N} C_{s,i}^{\pm} \boldsymbol{V}_{s,i}^{\pm} e^{-\lambda_{s,i}^{\pm}(\xi_s(x) - \xi_{s,0})} \tag{3.15}$$

where $\boldsymbol{V}_{s,i}^{\pm}$ and $\lambda_{s,i}^{\pm}$ are the i^{th} eigenvector and eigenvalue associated to the matrix $\boldsymbol{A}_s$ respectively, corresponding to forward and backward wave propagation associated with the layer s, $C_{s,i}^{\pm}$ correspond to the i^{th} order harmonic wave amplitudes of forward and backward wave propagation as explained in **Fig. 3.2**, and $\xi_{s,0}$ corresponds to the x coordinate at the far left point of the layer s. By directly solving this series of first order partial differential equations, we do not need to solve the dispersion relation separately, which is now automatically involved in the solution. Then by considering the boundary conditions (continuity of pressure and velocity) between the layers in contact labeled s and $s+1$,

$$\begin{bmatrix} \boldsymbol{p}^N(\xi_{s+1,0}) \\ \boldsymbol{v}^N(\xi_{s+1,0}) \end{bmatrix}_s = \begin{bmatrix} \boldsymbol{p}^N(\xi_{s+1,0}) \\ \boldsymbol{v}^N(\xi_{s+1,0}) \end{bmatrix}_{s+1} \tag{3.16}$$

By substituting Eq. (3.15) into Eq. (3.16), we have,

$$\begin{gathered} \sum_{i=-N}^{+N} C_{s+1,i}^{+} \boldsymbol{V}_{s+1,i}^{+} + \sum_{i=-N}^{+N} C_{s+1,i}^{-} \boldsymbol{V}_{s+1,i}^{-} = \\ \sum_{i=-N}^{+N} C_{s,i}^{+} \boldsymbol{V}_{s,i}^{+} e^{-\lambda_{s,i}^{+}(\xi_{s+1,0}-\xi_{s,0}))} + \sum_{i=-N}^{+N} C_{s,i}^{-} \boldsymbol{V}_{s,i}^{-} e^{-\lambda_{s,i}^{-}(\xi_{s+1,0}-\xi_{s,0})} \end{gathered} \tag{3.17}$$

This equation can be reformed into the form of matrix,

$$\langle \boldsymbol{V}_{s+1}^{+} | \boldsymbol{V}_{s+1}^{-} \rangle \begin{bmatrix} \boldsymbol{C}_{s+1}^{+} \\ \boldsymbol{C}_{s+1}^{-} \end{bmatrix} = \langle \boldsymbol{V}_{s}^{+} | \boldsymbol{V}_{s}^{-} \rangle \begin{bmatrix} \boldsymbol{H}_s & \boldsymbol{O} \\ \boldsymbol{O} & \boldsymbol{H}_s{}^{-1} \end{bmatrix} \begin{bmatrix} \boldsymbol{C}_{s}^{+} \\ \boldsymbol{C}_{s}^{-} \end{bmatrix} \tag{3.18}$$

where $\boldsymbol{H}_s = \begin{bmatrix} \boldsymbol{H}_s^{+} & \boldsymbol{O} \\ \boldsymbol{O} & \boldsymbol{H}_s^{-} \end{bmatrix}$, $\boldsymbol{H}_{s,(n,n')}^{\pm} = e^{-\lambda_{s,n-N-1}^{\pm}(\xi_{s+1,0}-\xi_{s,0})}\delta_{n-n'}$, $\boldsymbol{V}_s^{\pm} = \langle \boldsymbol{V}_{s,-N}^{\pm}, \dots, \boldsymbol{V}_{s,0}^{\pm}, \dots, \boldsymbol{V}_{s,N}^{\pm} \rangle$ and $\boldsymbol{C}_s^{\pm} = \left\langle C_{s,-N}^{\pm}, \dots, C_{s,0}^{\pm}, \dots, C_{s,N}^{\pm} \right\rangle^T$. $\xi_{s+1,0} - \xi_{s,0} = \frac{d_s \Omega}{c_s}$, where d_s is the length of layer s. Now we can obtain the transfer matrix $\boldsymbol{M}_{s\to s+1}$ which is defined by,

$$\begin{bmatrix} \boldsymbol{C}_{s+1}^{+} \\ \boldsymbol{C}_{s+1}^{-} \end{bmatrix} = \boldsymbol{M}_{s\to s+1} \begin{bmatrix} \boldsymbol{C}_{s}^{+} \\ \boldsymbol{C}_{s}^{-} \end{bmatrix} \tag{3.19}$$

$\boldsymbol{M}_{s\to s+1}$ can be developed from Eq (3.18),

$$\boldsymbol{M}_{s\to s+1} = \langle \boldsymbol{V}_{s+1}^{+} | \boldsymbol{V}_{s+1}^{-} \rangle^{-1} \langle \boldsymbol{V}_{s}^{+} | \boldsymbol{V}_{s}^{-} \rangle \begin{bmatrix} \boldsymbol{H}_s & \boldsymbol{O} \\ \boldsymbol{O} & \boldsymbol{H}_s{}^{-1} \end{bmatrix} \tag{3.20}$$

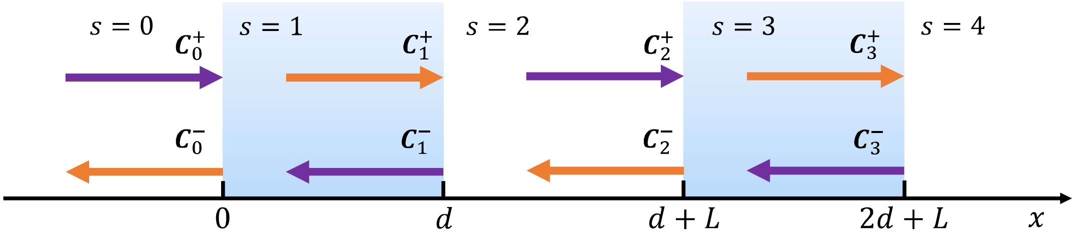

FIG. 3.2. Schematic of the transfer matrix $\boldsymbol{M}_{s\to s+1}$ between layers. $\boldsymbol{C}_s^{\pm}$ is the complex amplitude of forward/backward wave at the right boundary of layer s.

From Eq. (3.20), we constructed the transfer matrix $\boldsymbol{M}$ describing the complete system presented in **Fig.3.2**,

$$\boldsymbol{M} = \prod_{i}^{X} \boldsymbol{M}_{(X-i)\to(X+1-i)} \tag{3.21}$$

The above solution is based on Fourier decomposition and the precision of the solution is related to the considered number N of plane waves. In our work, the convergence of the result is guaranteed with $N \geq 4$.

The schematic of the scattering system is shown is **Fig. 3.3**. Refer to the Appendix A for the transformation from transfer matrix to scattering matrix. The transfer matrix $\boldsymbol{M}$ and the scattering matrix $\boldsymbol{S}$ are defined as

$$\begin{bmatrix} \boldsymbol{C}^N \\ \boldsymbol{D}^N \end{bmatrix} = \begin{bmatrix} \boldsymbol{M}_{11} & \boldsymbol{M}_{12} \\ \boldsymbol{M}_{21} & \boldsymbol{M}_{22} \end{bmatrix} \begin{bmatrix} \boldsymbol{A}^N \\ \boldsymbol{B}^N \end{bmatrix} \tag{3.22}$$

$$\begin{bmatrix} \boldsymbol{B}^N \\ \boldsymbol{C}^N \end{bmatrix} = \begin{bmatrix} \boldsymbol{S}_{11} & \boldsymbol{S}_{12} \\ \boldsymbol{S}_{21} & \boldsymbol{S}_{22} \end{bmatrix} \begin{bmatrix} \boldsymbol{A}^N \\ \boldsymbol{D}^N \end{bmatrix} \tag{3.23}$$

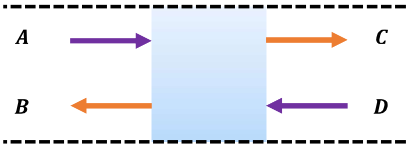

FIG. 3.3. Schematic of the system for matrix conversion.

where $\boldsymbol{A}^N = \langle A_{-N}, \dots, A_N \rangle^T$, $\boldsymbol{B}^N = \langle B_{-N}, \dots, B_N \rangle^T$, $\boldsymbol{C}^N = \langle C_{-N}, \dots, C_N \rangle^T$ and $\boldsymbol{D}^N = \langle D_{-N}, \dots, D_N \rangle^T$. $\boldsymbol{M}_{11}$, $\boldsymbol{M}_{12}$, $\boldsymbol{M}_{21}$ and $\boldsymbol{M}_{22}$ are matrices with $2N + 1$ orders.

Using the vector describing the incident wave of positive direction $\boldsymbol{J}^+ = \langle K_N, \dots, K_0, \dots, K_{-N} | \boldsymbol{O}^N \rangle^T$, we can deduce the corresponding reflection and transmission coefficients, K_n is Kronecker function,

$$\begin{bmatrix} \boldsymbol{r}^{N,+} \\ \boldsymbol{t}^{N,+} \end{bmatrix} = \boldsymbol{S} \cdot \boldsymbol{J}^{+} \tag{3.24}$$

where $\boldsymbol{r}^{N,+} = \langle r_{-N}^{+}, \dots, r_{0}^{+}, \dots, r_{N}^{+} \rangle^{T}$ and $\boldsymbol{t}^{N,+} = \langle t_{-N}^{+}, \dots, t_{0}^{+}, \dots, t_{N}^{+} \rangle^{T}$. Similarly, the reflection and transmission coefficients for negative incidence can be obtained using the vector associated to negative incident wave: $\boldsymbol{J}^{-} = \langle \boldsymbol{O}^{N} | K_{-N}, \dots, K_{0}, \dots, K_{N} \rangle^{T}$,

$$\begin{bmatrix} \boldsymbol{t}^{N,-} \\ \boldsymbol{r}^{N,-} \end{bmatrix} = \boldsymbol{S} \cdot \boldsymbol{J}^{-} \tag{3.25}$$

where $\boldsymbol{t}^{N,-} = \langle t_{-N}^{-}, \dots, t_{0}^{-}, \dots, t_{N}^{-} \rangle^{T}$ and $\boldsymbol{r}^{N,-} = \langle r_{-N}^{-}, \dots, r_{0}^{-}, \dots, r_{N}^{-} \rangle^{T}$ are the corresponding transmission and reflection coefficients, respectively.

These equations allowed us to evaluate the transmission and reflection coefficients for each frequency order. We have performed a series of calculations using our theoretical model to determine the optimized design that enables unidirectional propagation and frequency conversion. The involved parameters for our optimization process are the incident angular frequency ω, the modulation frequency Ω, the static density ratio δ and the phase difference between the modulations of the slabs $\Delta\phi = \phi_1 - \phi_2$.

III. Results and discussion

III.1. Single slab resonator

In the present study, the considered intrinsic parameters for air at ambient temperature are: $\rho_0 = 1.2\, kg/m^3$ and $c_0 = 343\, m/s$. Since the acoustic equations are linear in this study, we considered normalized incident frequency $F_{in} = \omega/(2\pi\, f_{\mathrm{r}}^{\delta})$ and normalized modulation frequency $F_m = \Omega/(2\pi\, f_{\mathrm{r}}^{\delta})$, where $f_{\mathrm{r}}^{\delta} = c_1^{\delta}/(2d)$ is the resonance frequency of the slab without temporal modulation.

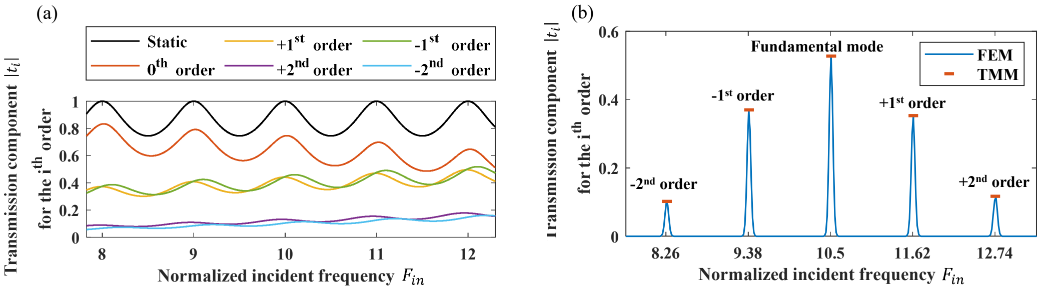

FIG. 3.4. Transmission through a single time modulated slab. (a) Calculated transmission in the static case (black solid line) and transmission components $|t_i|$ for

the i^{th} order up to the second order. The modulation frequency in this case is $F_m = 1.12$. (b) Transmission spectrum for an incident monochromatic wave at frequency F_{in}=10.5. Blue solid curve stands for the spectrum obtained from time dependent finite element simulation (FEM), while red flat marks stand for theoretically predicted transmission coefficients for the 0^{th}, $\pm 1^{st}$ and $\pm 2^{nd}$ orders (TMM).

Fig. 3.4 shows the transmission results for the case of $\delta = 5$, $F_m = 1.12$ and $N = 5$. In such configuration, since the modulation rate is relatively weak, the conversion from the fundamental mode to higher order harmonics ($|n| \geq 3$) can be omitted, so, only $n = 0, \pm 1, \pm 2$ are shown in the figure. **Fig. 3.4(a)** displays the transmission curves for the static case without modulation (black curve) and the transmission coefficients for the time modulated slab for orders $i = 0, \pm 1, \pm 2$ as function of the incident frequency. We can see that under temporal modulation, part of the energy of the fundamental mode is converted to higher orders modes located at $F_{in} \pm nF_m$. It indicates that if the system is properly tuned, the nonreciprocity is feasible with some spatial bias involved under considerable frequency conversion. Further, we confronted these results with numerical ones from simulations based on finite elements (FE) via the commercial software COMSOL Multiphysics v5.5. The comparison is shown in **Fig. 3.4(b)** for the chosen case of the monochromatic incident wave at frequency $F_{in} = 10.5$. Because of the existence of time-varying properties, the FE simulations were performed in the time domain. The length of input signal has to be much longer than the modulation period $T_m = 2\pi/\Omega$ in order to guarantee the stability and accuracy of the result. In **Fig. 3.4(b)**, the response of the time modulated slab is analyzed via Fourier transform. Nice agreement between theory (flat symbols) and simulation (blue solid lines) was observed.

III.2. Bilayer slab resonator

As shown in **Fig. 3.1(b)**, spatial bias is introduced into the system by connecting a second time-modulated slab resonator with different initial phase of the time modulation. We consider the two slabs with the same thickness d, located at $x = 0$ and $x = L + d$, with an air medium of length L between them. The inner air medium can be seen as a resonator as well whose resonance frequency is $f_g = c_0 / 2L$. In order to achieve good nonreciprocity with this system, we tune the incident frequency F_{in}, the modulation frequency Ω, the static density ratio δ and the phase difference $\Delta\phi$ between the modulations of the two slabs, within certain ranges. Our strategy to achieve nonreciprocity is two-level tuning. Firstly, we tune F_{in} and F_m with properly predefined $\Delta\phi$ and δ. By analyzing the diagrams of transmittance asymmetry difference $\left|T_0^+ - T_0^-\right|$ (with $T_0^+ = |t_0^+|^2$ and $T_0^- = |t_0^-|^2$), their ratio $\left|10\,log_{10}(T_0^+/T_0^-)\right|$ and the total transmission difference $\left|(\sum_{-N}^{N} T_i^+)^{\frac{1}{2}} - (\sum_{-N}^{N} T_i^-)^{\frac{1}{2}}\right|$, we were able to select a proper series of F_{in} and F_m. Afterwards, a fine optimization was performed by tuning $\Delta\phi$ and δ with fixed F_{in} and F_m. To access the nonreciprocity at a specific frequency, we can scale the dimension of the whole structure.

The coupling behavior of the resonators in static state (without modulation) has a significant effect on nonreciprocity. A definite static coupling behavior reduces variable elements in the tuning process. To characterize the coupling behavior, we introduce coupling factor $\alpha = f_g/f_{\mathrm{r}}^{\delta}$, the ratio between the resonance frequency of the inner air waveguide $f_g = c_0/2L$ and the static slab resonance frequency f_{r}^{δ}.

The value of α is directly related to the coupling behaviors in static state, which we plotted in **Fig. 3.5**, the transmission coefficients without modulation for various values of coupling factor α. **Fig. 3.5 (a)** displays the classical resonances of the single slab, while **Fig. 3.5(b)-(d)** are the transmission curves for the case of two coupled static slabs for different values of α. As we increase the coupling factor, the scattering changes and the average transmission bandwidth becomes smaller while stronger undulations of the transmission coefficient occur. Strong coupling is desired in order to achieve strong nonreciprocity and frequency conversion. Addtionally, the frequency interval between the sub-crests (red mark in **Fig. 3.5**) has close relation with the selection of modulation frequency.

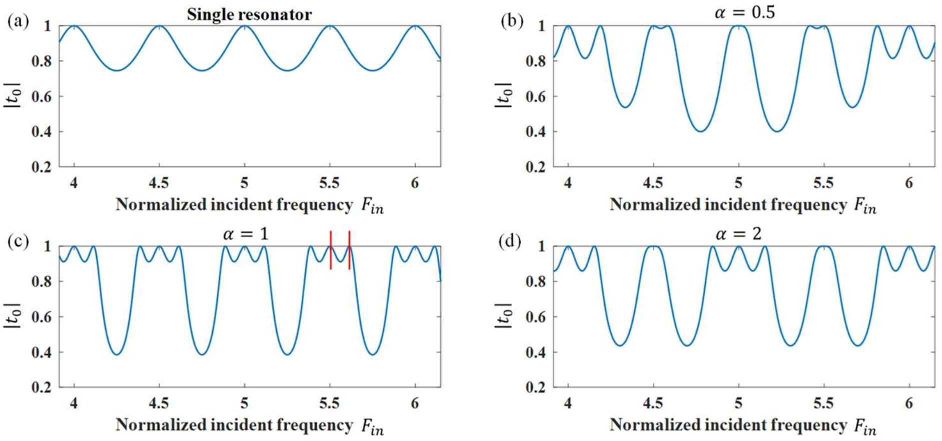

FIG. 3.5. Transmission coefficient for the static case (without time modulation): (a) single resonator, (b) cascaded resonators with $\alpha = 0.5$, (c) cascaded resonators with $\alpha = 1$ and (d) cascaded resonators with $\alpha = 2$. Red lines mark an example of frequency interval between the sub-crests.

The static density ratio δ determines the effective sound speed and the effective density in the slab medium, thus, its static impedance. Therefore, it affects directly the scattering behavior on the boundary between slab and air, because this density change leads to mismatched impedance on the boundary which affects the wave propagation. As δ is larger, this scattering becomes stronger, which contributes to the wave asymmetry under spatial bias. However, large δ weakens the feasibility of the system, so we selected $\delta = 5$. The thickness of slab is set as $d = 0.05m$ and the length of the air medium L is determined by $L = \sqrt{\delta} d/\alpha$.

The density of the two cascaded slabs is time-modulated as $\rho_1 = \delta\rho_0[1 + 2 \cdot M \cos(\Omega t)]$ and $\rho_2 = \delta\rho_0[1 + 2 \cdot M \cos(\Omega t + \Delta\phi)]$, where the phase difference $\Delta\phi$ is considered. In what follows, we utilized 0.5π as the preset value of $\Delta\phi$ which leads to spatiotemporal bias and breaks the time reversal symmetry. When $\Delta\phi = 0$, the system complies with time reversal symmetry as the bilayer slab resonator system is symmetric. When $\Delta\phi = \pi$, although the time reversal symmetry is broken, it only leads to phase inversion between the wave transmitted in opposite directions while the amplitudes maintain the same. As asymmetry appears in $\Delta\phi \in (0, \pi)$ while we get no asymmetry at both limits of this range, an extremum exists. Consequently, we have first chosen $\Delta\phi = 0.5\pi$ where we expect the maximum effect of asymmetry.

In order to verify the consistency of the preset phase difference $\Delta\phi = 0.5$, a series of calculations were performed upon $\Delta\phi$. **Fig. 3.6** displays the absolute value of difference between the right and left transmission coefficients of the fundamental mode, $\left||t_0^+| - |t_0^-|\right|$, as function of $\Delta\phi$ for the considered modulating frequencies F_m = 0.7, 0.9, and 1.1. For all these cases, high level of transmission difference occurs where $\Delta\phi$ is between 0.4 π and 0.6 π. To conclude, it is reasonable to assume strong asymmetry at $\Delta\phi = 0.5$.

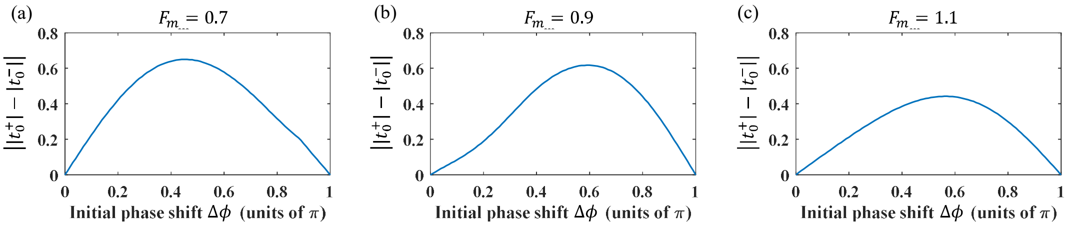

FIG. 3.6. Transmission coefficient difference $\left||t_0^+| - |t_0^-|\right|$ of the fundamental mode as function of $\Delta\phi$ for an incident wave frequency of $F_{in} = 8.94$, for the case of frequency modulations $F_m = 0.7$ (a), $F_m = 0.9$ (b), and $F_m = 1.1$ (c).

The modulation depth M is directly related to the external energy input into the system actively, so practically we tend to adopt relatively small values for the modulation depth. A weak modulation not only improves the feasibility of the system, but also prevents the transmitted wave from being over-amplified. Here the modulation depth is chosen as $M = 0.06$. Then, we first searched for nonreciprocal wave behavior by sweeping the incidence frequency F_{in} and the modulation frequency F_m.

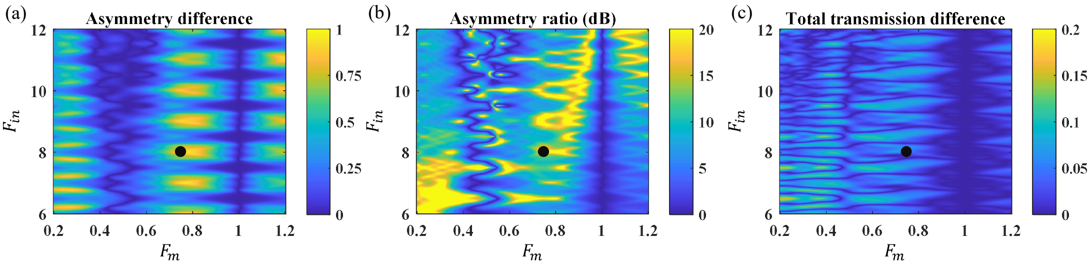

FIG. 3.7. Transmission analysis between right and left propagations as function of the normalized incident frequency F_{in} and the normalized modulation frequency F_m, for $\Delta\phi = 0.5\pi$ and $\delta = 5$. (a) Asymmetry difference of the 0th order mode transmittance, standing for $|T_0^+ - T_0^-|$. (b) Asymmetry ratio of 0th order mode transmittance, standing for $|10\, log_{10}(T_0^+/T_0^-)|$. (c) Total transmission difference, standing for $\left|(\sum_{-N}^{N} T_i^+)^{\frac{1}{2}} - (\sum_{-N}^{N} T_i^-)^{\frac{1}{2}}\right|$ where all the modes are included. The black dot in these figures marks the point where $F_{in} = 8$ and $F_m = 0.76$.

Here we are interested in the scattering properties of the fundamental mode. **Fig. 3.7(a)** and **(b)** show the quantities $|T_0^+ - T_0^-|$ and $|10\log_{10}(T_0^+/T_0^-)|$ for the fundamental mode, respectively, as function of the normalized modulation frequency F_m and incident frequency F_{in}. **Fig. 3.7(c)** plots the normalized total transmission difference for the convenience of observation. The criterions of nonreciprocity are $|T_0^+ - T_0^-| > 0.9$ and $|10\log_{10}(T_0^+/T_0^-)| > 20\text{dB}$ in a wide range of F_{in}, which correspond to yellow zones which are wide on the F_{in} axis in the plots. As shown in **Fig. 3.7(c)**, high level asymmetry of total transmission did not appear in this system, so the nonreciprocity here is mainly leaded by frequency conversion. We observe that **Fig. 3.7(a)** and **(b)** show some periodicity on the F_{in} axis. The nonreciprocity zones tend to appear at multiples of the resonance frequency of the slab, for example, the marked point where $F_{in} = 8$ corresponds to the actual frequency $8f_{\mathrm{r}}^{\delta}$. In fact, far away from resonances, the reflection is dominant and the effect of frequency conversion on the transmitted waves becomes comparably weak. Another interesting phenomenon reflected in the **Fig. 3.7** is that when $F_m = 1$ and $\alpha = 1$, all the asymmetries disappear. In this case, the actual modulation frequency is equal to the resonance frequency of the slab, $f_m = f_{\mathrm{r}}^{\delta}$, where the spatial biasing effect from phase difference is almost cancelled.

For an optimized case of nonreciprocity, we selected $F_{in} = 8$ and $F_m = 0.76$, where $|T_0^+ - T_0^-| = 0.956$ and $|10\,log_{10}(T_0^+/T_0^-)| = 25.98\text{dB}$ (Black dot indicated in **Fig. 3.7**). Under this configuration, the positive and negative transmission coefficients of the fundamental mode are $t_0^+ = 0.049$ and $t_0^- = 0.979$. While adopting the above values of F_{in} and F_m, we performed a 2nd level fine tuning where we swept for δ and $\Delta\phi$. **Fig. 3.8(a)** and **(b)** show $|T_0^+ - T_0^-|$ and $|10\,log_{10}(T_0^+/T_0^-)|$ of the fundamental mode, respectively, as function of the static density ratio δ and phase difference $\Delta\phi$, while **Fig. 3.8(c)** plots the total transmission difference. We can see that with the preselected $\delta = 5$ and $\Delta\phi = 0.5\pi$, the result is already good, so we just slightly change the value of $\Delta\phi$. The result of fine optimization is $\Delta\phi = 0.46\pi$ and $\delta = 5$, where $|T_0^+ - T_0^-| = 0.957$ and $|10\,log_{10}(T_0^+/T_0^-)| = 27.15\text{dB}$.

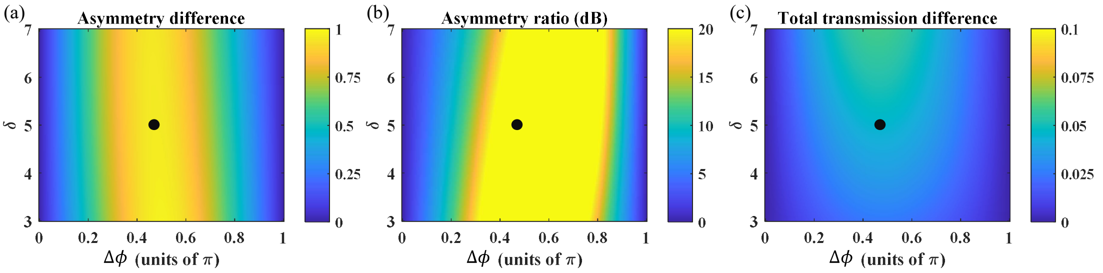

FIG. 3.8. Results of the theoretical calculation sweeping $\Delta\phi$ from 0 to π and δ from 3 to 7, with $F_{in} = 8$ and $F_m = 0.76$ inherited from the last calculation. (a) Asymmetry difference of 0th order mode transmittance. (b) Asymmetry ratio of 0th order mode transmittance. (c) Total transmission difference. The black dot in these figures marks the point where $\Delta\phi = 0.46\pi$ and $\delta = 5$.

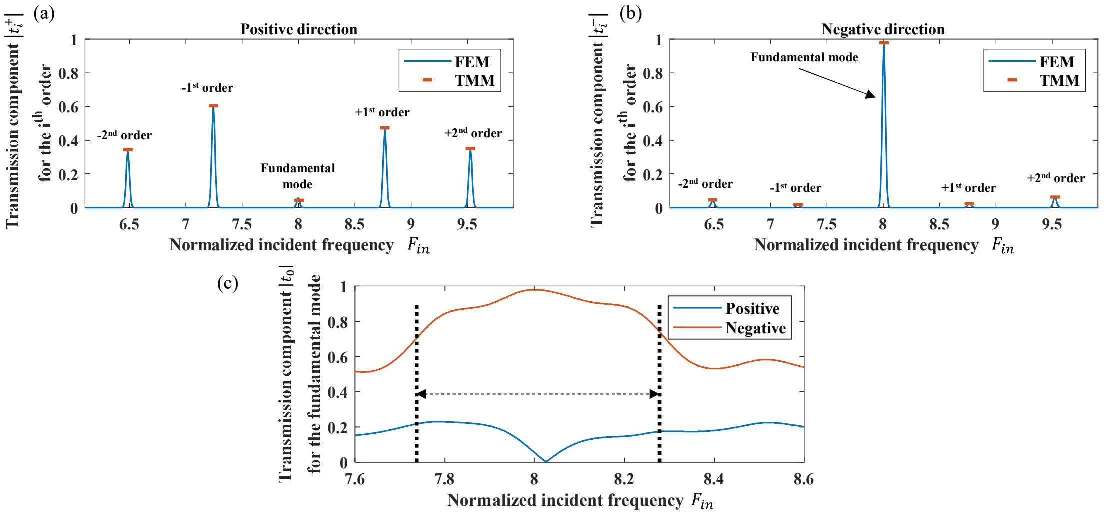

FIG. 3.6. (a) (b) Transmission coefficient for the positive direction (a) and the negative direction (b) with $F_{in} = 8$, $F_m = 0.76$, $\Delta\phi = 0.46\pi$ and $\delta = 5$. (c) Theoretically calculated transmission coefficient curve for the fundamental mode (0th order) for both directions as function of F_{in}, for $F_m = 0.76$, $\Delta\phi = 0.46\pi$ and $\delta = 5$. The black dash lines and arrow mark the bandwidth.

With this fine optimization, the transmission coefficients become $t_0^+ = 0.043$ and $t_0^- = 0.979$, so nonreciprocal transmission is slightly improved in comparison with the previous result. For this configuration, we plot in **Fig. 3.9** the transmission coefficient in both propagation directions with incident monochromatic wave at the frequency of $F_{in} = 8$ (**Fig. 3.9(a)** and **(b)**). We can clearly observe that the 0th order mode is dominant in the negative propagation direction while it is almost depleted in the positive direction with strong frequency conversion at higher order modes. We also plot the fundamental mode transmission in both propagation directions in **Fig. 3.9(c)** where we can deduce acoustic nonreciprocity around the incident frequency. The bandwidth of nonreciprocity is defined as $|T_0^+(\omega) - T_0^-(\omega)| > 0.5 \times \mathrm{Max}(|T_0^+ - T_0^-|)$. The normalized bandwidth of nonreciprocity ΔF is approximately 0.51 in this case.

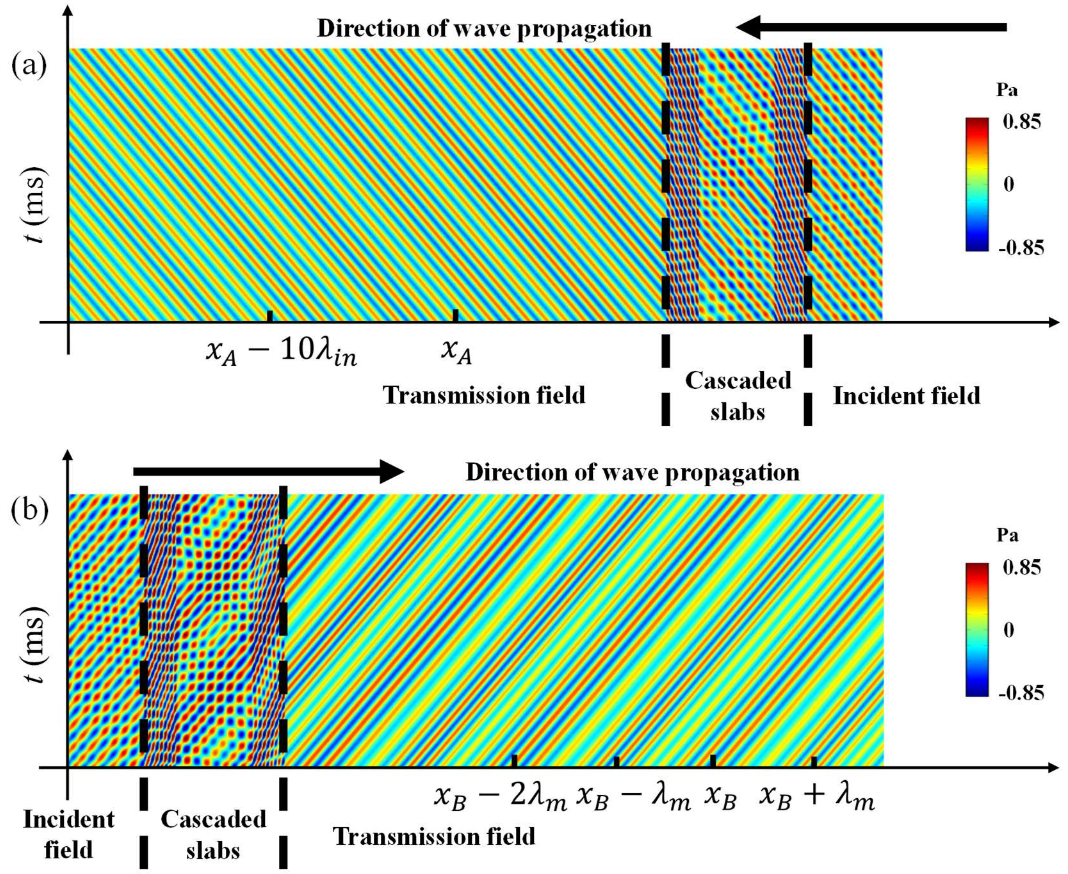

FIG. 3.7. Pressure field pattern for the case reported in **Fig. 3.9**(a) and (b), from 30ms to 31ms. $\lambda_{in} = 1/f_{in}$ is the wavelength of the incident wave and $\lambda_m = 2\pi/\Omega$ is the modulation wavelength. (a) Negative direction; (b) positive direction.

To further illustrate the nonreciprocity behavior, we plot in **Fig. 3.10** the total pressure as function of space and time based on transit FEM simulation. The figure shows the total pressure on the whole structure within a specific duration. In the negative direction (**Fig. 3.10(a)**), the incident wave can pass through our structure and the wave form is little distorted, indicating the transmission of the fundamental mode with relatively low reflection in contrast to that of the positive direction. However, in the positive direction (**Fig. 3.10(b)**), we observe a different wave propagation phenomenon where the pattern of the fundamental mode is no longer dominant, and frequency conversion to higher order modes is observed. The modulation wave behavior shown in **Fig. 3.10(b)** corresponds to the superposition of several harmonic waves (±1 order, ±2 order, etc.).

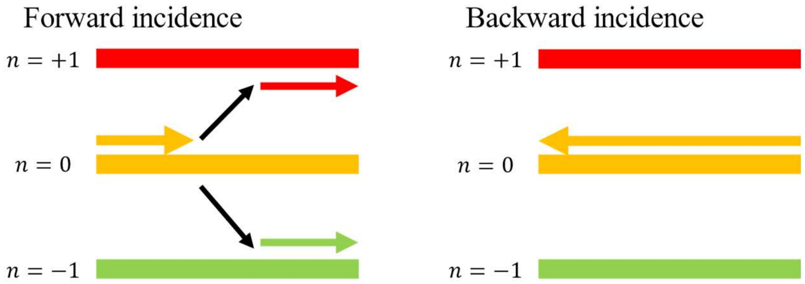

FIG. 3.8. Energy flux in bi-resonator time-modulated systems. In forward direction, the energy on the fundamental mode is transferred to the ± 1 Floquet harmonics, then transmission coefficient at the incident frequency is 0. In backward direction, almost no frequency conversion is observed, then the energy on the fundamental mode gets a full transmission.

According to the results we get in **Fig. 3.9**, we can summarize that, unlike the conventional STM in which the nonreciprocity functionalities depend on the Doppler-style directional bandgap, the nonreciprocity in bi-resonator time-modulated structures relies on the directional Floquet frequency conversion. Owing to the spatial bias existing in the bi-resonator structures, different Floquet frequency conversions occur in the two propagation directions. **Fig. 3.11** illustrates how directional Floquet frequency conversions conduct the nonreciprocal wave propagation. In one specific direction, the incident wave energy is found at the other Floquet mode-conversion frequencies, but in another direction, no mode conversion occurs to obstruct the incident wave passing through at its original frequency.

To figure out the nature of nonreciprocity in this structure, we examine the wave propagation (pressure field in space and in time) in the waveguide area between the resonators (**Fig. 3.10**). We find out that, in the case where few harmonics are found in the transmission (quasi full transmission of the fundamental mode), considerable harmonics can still be observed in the inter waveguide area, and the result of their Fourier transfer is very close to that of single resonator transmission. We associate it with the fact that, although being time-modulated, this type of system has weak reflection at all the harmonics frequencies when the incidence is at the resonance frequency, no matter in case of single resonators or bi resonators. While with the harmonics as incidence (the harmonics from the first FP resonator travel to the second one), the scattering performs differently. So, the coupling between the resonators and the inter FP resonance is the combination of reflections and phase evolution. In result, we can observe the above phenomenon in **Fig. 3.10**. In personal point of view, it is the key indication to the following inference: the harmonics in the second passing-through resonators interfere the initial harmonics from the first resonators; in the full-transmission direction, the secondary frequency conversion cancels the high-order modes in the initial harmonics and recover the energy back to the fundamental mode; in the “zero-transmission” direction, the secondary frequency conversion cancels the fundamental mode in the initial harmonics instead. The cancelation in the above assumptions is supposed to be inversed-phase superposition of waves.

III.3. Unidirectional frequency conversion

Since the nonreciprocity in our system is achieved owing to frequency conversion, we further exploited the unidirectional frequency conversion under the nonreciprocity premise. As schematically shown in **Fig. 3.12**, for a harmonic excitation, if on a tuned modulation frequency, the first order corresponds to one of the resonance frequencies of the slab, this first order mode can be highly transmitted. There are numerous possibilities for frequency conversion, so we consider for instance two of them: from 0th to -1st and from 0th to +1st which are shown by arrows vertically orienting. In the example of **Fig. 3.12**, if we choose a specific frequency of modulation so that the -1st order corresponds to one of the resonance frequencies of the slab, this order could be highly transmitted while the fundamental mode and the +1st order being weakly transmitted. Further, if high transmission exists at both fundamental mode and one of the ± 1st order modes due to large transmission bandwidth, we can reach both unidirectional frequency conversion and nonreciprocity by manipulating the modulation.

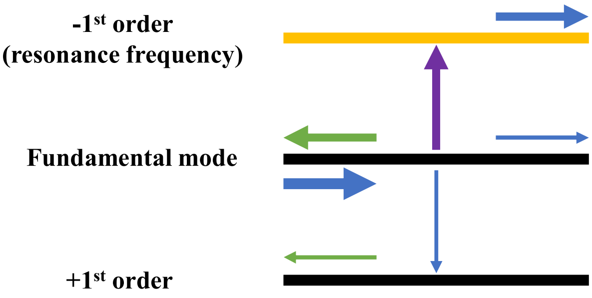

FIG. 3.9. Schematic of the frequency conversion. The -1st order mode is at the resonance frequency of the slab instead of the fundamental mode and the 1st order mode. Thus, -1st order mode may be transmitted with higher amplitude.

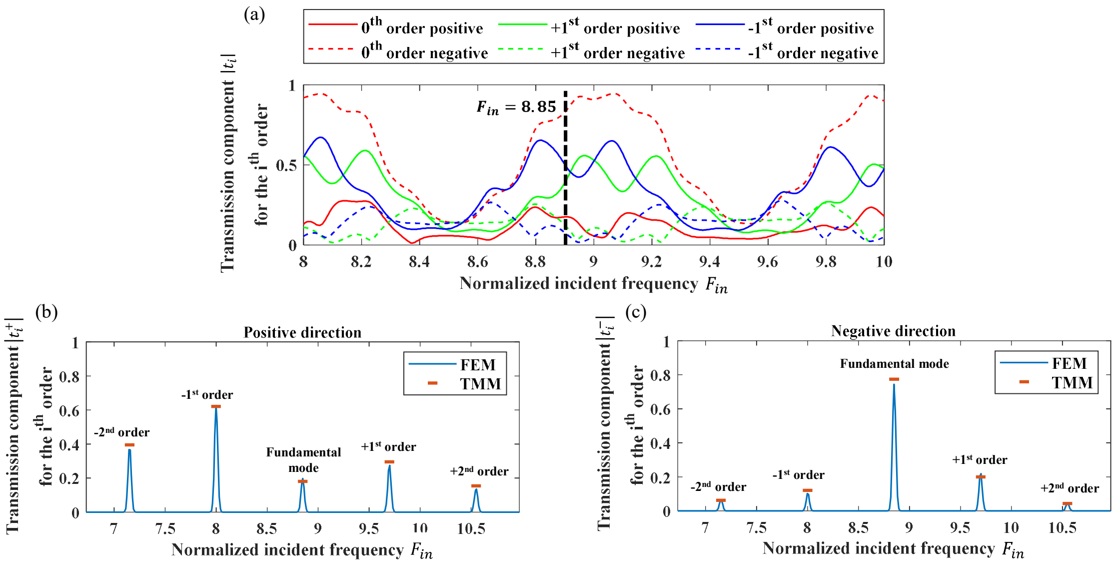

FIG. 3.10. (a) Transmission coefficient in the frequency domain for the 0th, ±1st and ±2nd orders with $F_m = 0.85$, $\Delta\phi = 0.589\pi$ and $\delta = 12$. Transmission spectrum coefficient in the positive direction (a) and the negative direction (b) at the monochromatic incident frequency $F_{in} = 8.85$, (flat marks for theory and solid blue line for FEM based simulation).

To illustrate this idea, we consider the configuration of $F_m = 0.85$, $\Delta\phi = 0.589\pi$ and $\delta = 12$ where strong asymmetries of all the ±1st and 0th order modes are achieved. We plot in **Fig. 3.13 (a)** the transmission coefficient in the frequency domain for the 0th and ±1st orders. We can observe that the ±1st orders modes are both dominant in the transmission for one of the directions of propagation. At $F_{in} = 8.85$ for instance, the -1st orders mode ($F_{in} - F_m$) is at a resonance frequency ($8f_r^\delta$). **Fig. 3.13 (b)** and **(c)** display the transmission coefficient with incident monochromatic wave at $F_{in} = 8.85$. In the positive direction, the amplitude of the -1st order reaches 0.61, becoming dominant, and the amplitude of the fundamental mode is 0.18, while in the negative direction, the fundamental mode's amplitude is 0.78 and the amplitudes of all the neighboring modes are low. In this case, unidirectional frequency conversion occurs.

Regarding the experimental implementation of the system, for instance, it can be built using successive layers of air and gas with different densities, separated by an airtight thin membrane to avoid mixture. Then, the effective density can be modulated in time using pistons that can change the volume of each cavity layer. The thickness of the layers can be tuned to operate at frequency ranges far from the flexural resonances of the membranes. The existence of the membranes will only slightly reduce the bandwidth of nonreciprocity which can still be achieved by fine tuning the parameters of the system.

IV. Conclusion

In this work, we have demonstrated nonreciprocal acoustic transmission and unidirectional frequency conversion in cascaded fluid slab resonators based on temporal modulation of their effective densities, with phase difference of the time modulations between the slabs. A theoretical TMM based on Fourier decomposition has been developed for efficient characterization of the acoustic dispersion of the system, while numerical simulations based on FEM have been conducted to assess the theoretical findings. Optimizations over the system's parameters was carried out to achieve broadband nonreciprocity and frequency conversion in the bi-slab system. An acoustic nonreciprocity behavior has been demonstrated for a monochromatic incident wave, with almost 97.9% transmission in the positive direction while only 4.3% is transmitted in the negative direction. Furthermore, unidirectional frequency conversion has been exploited. Over half of the transmitted acoustic energy has been converted into one single mode with higher static density ratio δ. The proposed design of nonreciprocal acoustic system displays promising functionalities, with a simple compact configuration to achieve unidirectional wave propagation and frequency conversion. Though the present system is purely theoretical and far from representing a realistic device for application, it is possible to imagine a solid system where we only consider longitudinal waves which are described with the same Helmholtz equation, thus behaves the same as acoustic waves in fluid. In this case, our approach could also be conducted by considering the time modulation of the effective stiffness of the materials using piezoelectric elements instead of density. Further, the time-modulation capability of the design is to be investigated especially when the frequency of modulation is comparable to the incident frequency of the system, our design offers a platform that could inspire futuristic devices for multiple applications, including biomedical ultrasound devices, improved energy harvesting and communication system.

References

[1] G. Trainiti and M. Ruzzene, New J. Phys. 18, 083047 (2016).

[2] Y. Wang, B. Yousefzadeh, H. Chen, H. Nassar, G. Huang, and C. Daraio, Phys. Rev. Lett. 121, 194301 (2018).

[3] G. Trainiti, Y. Xia, J. Marconi, G. Cazzulani, A. Erturk, and M. Ruzzene, Phys. Rev. Lett. 122, 124301 (2019).

[4] Z. Chen, C. Xue, L. Fan, S. Zhang, X. Li, H. Zhang, and J. Ding, Scientific Reports 6, 30254 (2016).

[5] C. Shen, J. Li, Z. Jia, Y. Xie, and S.A. Cummer, Phys. Rev. B 99, 134306 (2019).

[6] C. Shen, X. Zhu, J. Li, and S.A. Cummer, Phys. Rev. B 100, 054302 (2019).

[7] X. Zhu, J. Li, C. Shen, X. Peng, A. Song, L. Li, and S.A. Cummer, Appl. Phys. Lett. 116, 034101 (2020).

[8] M. Chegnizadeh, M. Memarian, and K. Mehrany, J. Opt. Soc. Am. B, JOSAB 37, 88 (2020).

[9] Q. Wang, Y. Yang, X. Ni, Y.-L. Xu, X.-C. Sun, Z.-G. Chen, L. Feng, X. Liu, M.-H. Lu, and Y.-F. Chen, Scientific Reports 5, 10880 (2015).

[10] G.J. Jeon and J.H. Oh, Phys. Rev. E 103, 012212 (2021).

[11] J.D. Schneider, T. Lu, S. Tiwari, X. Zou, A. Mal, R.N. Candler, Y.E. Wang, and G.P. Carman, Journal of Applied Physics 128, 064105 (2020).

[12] E. Riva, J. Marconi, G. Cazzulani, and F. Braghin, Journal of Sound and Vibration 449, 172 (2019).

[13] P.J. Westervelt, The Journal of the Acoustical Society of America 35, 535 (1963).

[14] A. Moussatov, B. Castagnède, and V. Gusev, Physics Letters A 301, 281 (2002).

Chapter 4

Nonreciprocal acoustic metamaterials based on cascaded time-modulated spring-mass resonators

Contents

I. Introduction

In elastodynamics, to pursuit the nonreciprocity, the spatiotemporal modulation is performed over the intrinsic properties of the material, namely the effective stiffness, using exotic physical and engineering approaches. For the achievement of non-reciprocity for elastic waves, the challenge was to come up with a realizable method that can enable dynamic modulation of the stiffness with a speed comparable to the propagating wave velocity. Wang et al.[1] was the first to experimentally perform such modulation using coupled magnet rings where the coupling can be varied in time via well placed coils to dynamically change the magnetic force. The system is equivalent to a series of mass and springs connected to the ground where the effective stiffness of the springs is modulated both in space and time. This magnet-coil based approach was proven the to be very effective to dynamically modulate the effective stiffness with high speed. In another study, Chen et al.[2] designed a tunable elastic metamaterial made of periodic resonators distributed on a plate where each resonator is constructed with a permanent magnet and a coil to control its effective stiffness, which led to a demonstration of nonreciprocal propagation of flexural waves. Another interesting yet different approach was proposed by Goldsberry et al[3]. who used nonlinear large deformations to spatiotemporally vary the effective stiffness and enables nonreciprocity. Differently, Trainiti et al.[4] proposed an efficient and fast approach to demonstrated nonreciprocal reflection and transmission of flexural waves. In their case, the modulation of the effective stiffness is performed using piezoelectric patches connected to well elaborated and controlled electrical circuits. Besides, a mechanical approach was introduced by Attarzadeh et al.[5] who used a series of local resonators in which the effective stiffness was modulated by varying the second area moment of inertia of each resonator's arm through dynamically changing its angular orientation. However, in these experimental works on spatiotemporally modulated phononic crystal and periodic metamaterials, numerous unit cells are considered to introduce a waveform variation of the effective stiffness both in space and time. This makes the design cumbersome and challenging to be considered for subwavelength applications where compact and integrated designs with high performance wave functionalities are desirable. Furthermore, in these proposed designs, programmed micro controller unit (MCU) is needed to synchronize the temporal modulation which seriously complicates the system. However, promising solutions for enabling non-reciprocity using compact devices were proposed in acoustics which are based on only two cascaded local resonators. These include slab resonators[6], Helmholtz resonators[7], air cavity resonators[8], and thin vibrating membranes[9]. The compactness of those structures makes them to be of great usability for miniaturizing acoustic devices.

In this chapter, we design and fabricate a compact low-frequency nonreciprocal flexural waveguide using only two time-modulable (spring-mass resonators) SMRs. Inspired by the work of Chen et al.[2] and Wang et al.[1], the resonators are physically realized by a coil-cantilever-magnet system with controllable alternating current (AC), and their mechanical behavior can be modeled as spring-mass equivalent resonators with time-dependent effective stiffnesses. By introducing a phase shift between the ACs of these two resonators, their stiffnesses are harmonically modulated in time with a controllable phase shift which leads to the realization of nonreciprocal flexural wave transmission. A simplified analytic approach based on Fourier decomposition is developed to analyze the flexural wave propagation in the system and support the observed experiment results around the designed operating frequency. The dimension of the cascaded resonator structure is less than 1/3 of the operating wavelength.

II. Theoretical modeling and analysis

II.1. Transfer matrix method (TMM) for P-waves

We started the theoretical modeling of the SMR-based nonreciprocal device designed for elastic P-wave due to its similarity with the acoustic wave. In this model, a cylindrical waveguide was considered as shown in Fig 4.1.

Denoting the axial displacement in the cylindrical waveguide as u, we began with the equation of motion for longitudinal waves[10] in one dimension,

$$\frac{\partial}{\partial x}\left[E\frac{\partial u(x,t)}{\partial x}\right]-\frac{\partial}{\partial t}\left[\rho\frac{\partial u(x,t)}{\partial t}\right]=0 \tag{4.1}$$

where E is the Young's modulus and ρ is the density. While the time modulation exists in such system, the solution to Eq (4.1) can be written in the generalized Floquet form[11],

$$u(x,t) = \sum_{n=-\infty}^{+\infty} (A_n e^{-ikx} + B_n e^{ikx}) e^{i(\omega+n\Omega)t} \tag{4.2}$$

where ω is the operating angular frequency, Ω is the modulation angular frequency, and k is the wave number. Acknowledging the generalized solution, we first study the case with only one SMR at the position $x = 0$, whose stiffness is time-modulated as $\kappa(t) = \kappa_0 + \kappa_M \cos(\Omega t + \phi)$ in which ϕ is the initial phase. At $x = 0$, the following conditions of continuity about the axial displacement and the axial force must be satisfied[11],

$$\begin{cases} u^-(0) - u^+(0) = 0 \\ F^-(0) - F^+(0) = F^e(0) \end{cases} \tag{4.3}$$

in which the signs – and + represent the left and right sides of the dedicated position, F^e is the external force from the SMR, and the axial force F could be expressed as,

$$F = ES\left.\frac{\partial u}{\partial x}\right|_{x=0} \tag{4.4}$$

where S is the section area of the cylindrical waveguide.

In the SMR, the mass has a displacement that can be described as,

$$u^m(x,t) = \sum_{n=-\infty}^{+\infty} u_n^m e^{i(\omega+n\Omega)t} \tag{4.5}$$

The external force F^e on the mass from the spring is,

$$F^e = -\big(u^m - u^-(0)\big)\kappa(t) \tag{4.6}$$

which leads to the equation of movement of the mass m,

$$\big(u^m - u^-(0)\big)\kappa(t) = m\frac{\partial^2 u^m}{\partial t^2} \tag{4.7}$$

The spring stiffness $\kappa(t)$ can be decomposed in the generalized Floquet form,

$$\kappa(t) = \sum_{p=-1}^{1} \kappa_p e^{ip\Omega t+\quad p} \tag{4.8}$$

where $\kappa_{\pm 1}$ equals to $0.5\kappa_m$. We insert Eqs (4.2) and $(4.4-4.6)$ into Eqs (4.3) and (4.7), and consider finite numbers N and N' of waves,

$$\begin{cases} \displaystyle\sum_{n=-N}^{+N}(A_n^- + B_n^-)e^{i(\omega+n\Omega)t} - \sum_{n=-N}^{+N}(A_n^+ + B_n^+)e^{i(\omega+n\Omega)t} = 0 \\ \displaystyle iES\left\{\left[\sum_{n'=-N'}^{+N'} k_{n'}\left(-A_{n'}^- + B_{n'}^-\right)e^{i(\omega+n'\Omega)t}\right] - \left[\sum_{n'=-N'}^{+N'} k_{n'}\left(-A_{n'}^+ + B_{n'}^+\right)e^{i(\omega+n'\Omega)t}\right]\right\} \\ \displaystyle = -\left[\sum_{n=-N}^{+N} u_n^m e^{i(\omega+n\Omega)t} - \sum_{n=-N}^{+N}(A_n^- + B_n^-)e^{i(\omega+n\Omega)t}\right]\sum_{p=-1}^{1}\kappa_p e^{j\Omega t+\ \ _p} \\ \displaystyle \left[\sum_{n=-N}^{+N} u_n^m e^{i(\omega+n\Omega)t} - \sum_{n=-N}^{+N}(A_n^- + B_n^-)e^{i(\omega+n\Omega)t}\right]\sum_{p=-1}^{1}\kappa_p e^{j\Omega t+\phi_p} = \\ \displaystyle -m\sum_{n=-N'}^{+N'}(\omega+n'\Omega)^2 u_{n'}^m e^{i(\omega+n'\Omega)t} \end{cases} \tag{4.9}$$

The above equations can be simplified,

$$\begin{cases} \displaystyle\sum_{n=-N}^{+N}(A_n^- + B_n^- - A_n^+ - B_n^+)e^{i(\omega+n\ \ )t} = 0 \\ \displaystyle iES\sum_{n'=-N'}^{+N'} k_{n'}\left(-A_{n'}^- + B_{n'}^- + A_{n'}^+ - B_{n'}^+\right)e^{i(\omega+n'\Omega)t} \\ \displaystyle = \sum_{N,1}(A_n^- + B_n^- - u_n^m)\kappa_p e^{i\phi_p}e^{i[\omega+(n+p)\Omega]t} \\ \displaystyle \sum_{N,1}(A_n^- + B_n^- - u_n^m)\kappa_p e^{i\phi_p}e^{i[\omega+(n+p)\Omega]t} = \\ \displaystyle -m\sum_{n=-N'}^{+N'}(\omega+n'\Omega)^2 u_{n'}^m e^{i(\omega+n'\Omega)t} \end{cases} \tag{4.10}$$

Then by replacing $n+p$ by n' and p by $n'-n$, the second equation in Eqs (4.10) can be developed,

$$iES\sum_{N'} k_{n'}\left(-A_{n'}^- + B_{n'}^- + A_{n'}^+ - B_{n'}^+\right)e^{i(\omega+n'\Omega)t}$$

$$= \sum_{N',N}(A_n^- + B_n^- - u_n^m)\kappa_{n'-n}e^{i\phi_{n'-n}}e^{i(\omega+n'\Omega)t} \tag{4.11}$$

We perform similar algebraic manipulation on the third equation in Eqs (4.10),

$$\sum_{N',N}(A_n^- + B_n^- - u_n^m)\kappa_{n'-n}e^{i\phi_{n'-n}}e^{i(\omega+n'\Omega)t} = \\ -m\sum_{N'}(\omega+n'\Omega)^2 u_{n'}^m e^{i(\omega+n'\Omega)t} \tag{4.12}$$

To be followed, we can eliminate the sign of sum and the time-related term by applying the orthogonality relationship,

$$\begin{cases} A_n^- + B_n^- - A_n^+ - B_n^+ = 0 \\ ik_nES(-A_n^- + B_n^- + A_n^+ - B_n^+) \\ \quad = \sum_{N'}\left(A_{n'}^- + B_{n'}^- - u_{n'}^m\right)\kappa_{n-n'}e^{i\phi_{n-n'}} \\ -\sum_{N'}\left(A_{n'}^- + B_{n'}^- - u_{n'}^m\right)\kappa_{n-n'}e^{i\phi_{n-n'}} = m(\omega+n\Omega)^2 u_n^m \end{cases} \tag{4.13}$$

where we swap n' and n. Eq (4.13) can be reformed into vector equations under some approximations,

$$\begin{bmatrix} \boldsymbol{I} & \boldsymbol{I} & \boldsymbol{O} \\ -\boldsymbol{\Lambda}-\boldsymbol{K} & \boldsymbol{\Lambda}-\boldsymbol{K} & \boldsymbol{O} \\ -\boldsymbol{K} & -\boldsymbol{K} & \boldsymbol{O} \end{bmatrix} \begin{bmatrix} \boldsymbol{A}^{-,N} \\ \boldsymbol{B}^{-,N} \\ \boldsymbol{O} \end{bmatrix} = \begin{bmatrix} \boldsymbol{I} & \boldsymbol{I} & \boldsymbol{O} \\ -\boldsymbol{\Lambda} & \boldsymbol{\Lambda} & -\boldsymbol{K} \\ \boldsymbol{O} & \boldsymbol{O} & \boldsymbol{T}-\boldsymbol{K} \end{bmatrix} \begin{bmatrix} \boldsymbol{A}^{+,N} \\ \boldsymbol{B}^{+,N} \\ \boldsymbol{u}^{m,N} \end{bmatrix} \tag{4.14}$$

where χ_j is ik_jES, ψ_j is $\kappa_z e^{i\phi_z}$ ($z = -1, 0$ or 1), and ξ_j is $m(\omega + j\Omega)^2$. The wavenumber k_j in this longitudinal waveguide system respects the dispersion relationship $(\omega + j\Omega)/\sqrt{E/\rho}$. The above equations are decomposed from $N-1$ to $N+1$ orders. $\boldsymbol{A}^{+,N}$, $\boldsymbol{B}^{+,N}$, $\boldsymbol{A}^{-,N}$ and $\boldsymbol{B}^{-,N}$ are of the form $\boldsymbol{X}^{s,N} = \langle X_{-N}^s, \dots, X_0^s, \dots, X_{+N}^s\rangle^T$, $\boldsymbol{X}$ can be either $\boldsymbol{A}$ or $\boldsymbol{B}$ and s takes either the sign "−" or "+", $\boldsymbol{u}^{m,N} = \langle u_{-N}^m, \dots, u_0^m, \dots, u_{+N}^m\rangle^T$, $\boldsymbol{I}$ is unitary matrix, $\Lambda_{n,m} = \chi_n\delta_{n,m}$, $K_{n,m} = \psi_0\delta_{n,m} + \psi_{-1}\delta_{n,m+1} + \psi_1\delta_{n,m-1}$, $T_{n,m} = \xi_n\delta_{n,m}$, and $\boldsymbol{O}$ is zero matrix. δ is the Kronecker function.

The total dimension of each matrix is $3(2N+1)$. We denote the matrix at the left side by $\boldsymbol{M}^-$ and that at the right side by $\boldsymbol{M}^+$, finally we have the transfer matrix $\boldsymbol{M}$,

$$\boldsymbol{M} = (\boldsymbol{M}^+)^{-1}\boldsymbol{M}^- \tag{4.15}$$

The u^m terms are not needed in the transfer matrix because they are not input terms nor output terms, so we eliminate them by delete the last $2N+1$ rows and the last $2N+1$ lines in $\boldsymbol{M}$. Thus, the definition of $\boldsymbol{M}$ is now,

$$\begin{bmatrix} \boldsymbol{A}^{+,N} \\ \boldsymbol{B}^{+,N} \end{bmatrix} = \boldsymbol{M} \begin{bmatrix} \boldsymbol{A}^{-,N} \\ \boldsymbol{B}^{-,N} \end{bmatrix} \tag{4.16}$$

In the bi-resonator system where we denote the distance between two resonators l, the global transfer matrix $\boldsymbol{M}^g$ is composed of 3 parts,

$$\boldsymbol{M}^g = \boldsymbol{M}^2 \boldsymbol{M}^w \boldsymbol{M}^1 \tag{4.17}$$

where $\boldsymbol{M}^1$ and $\boldsymbol{M}^2$ are the transfer matrix for the two resonators with different initial time modulation phase, and $\boldsymbol{M}^w$ is the transfer matrix for the bare waveguide between the two resonators. According to the generalized solution in Eq (3.2),

$$\boldsymbol{M}^w = \begin{bmatrix} \boldsymbol{\Gamma} & \boldsymbol{O} \\ \boldsymbol{O} & \boldsymbol{\Gamma}^{-1} \end{bmatrix} \tag{4.18}$$

where $\boldsymbol{\Gamma} = \mathrm{diag}(e^{-ik_{-N}l}, \dots, e^{-ik_j l}, \dots e^{-ik_N l})$.

By applying the same matrix manipulation as we did in the Chapter 3, the global transfer matrix $\boldsymbol{M}^g$ can be converted to the global scattering matrix $\boldsymbol{S}$,

$$\begin{bmatrix} \boldsymbol{u}^{t,N} \\ \boldsymbol{u}^{r,N} \end{bmatrix} = \boldsymbol{S} \begin{bmatrix} \boldsymbol{u}^{i,N} \\ \boldsymbol{O} \end{bmatrix} \tag{4.19}$$

where $\boldsymbol{u}^{t,N} = \boldsymbol{A}^{+,N}$, $\boldsymbol{u}^{r,N} = \boldsymbol{B}^{-,N}$and $\boldsymbol{u}^{i,N} = \boldsymbol{A}^{-,N}$ refer to the transmitted, reflected and incident waves (**Fig. 4.1**).

The schematic of this longitudinal waveguide system is shown in **Fig. 4.1**. The ring masses are attached to the springs, which in turn are attached to the waveguide via rigid supports.

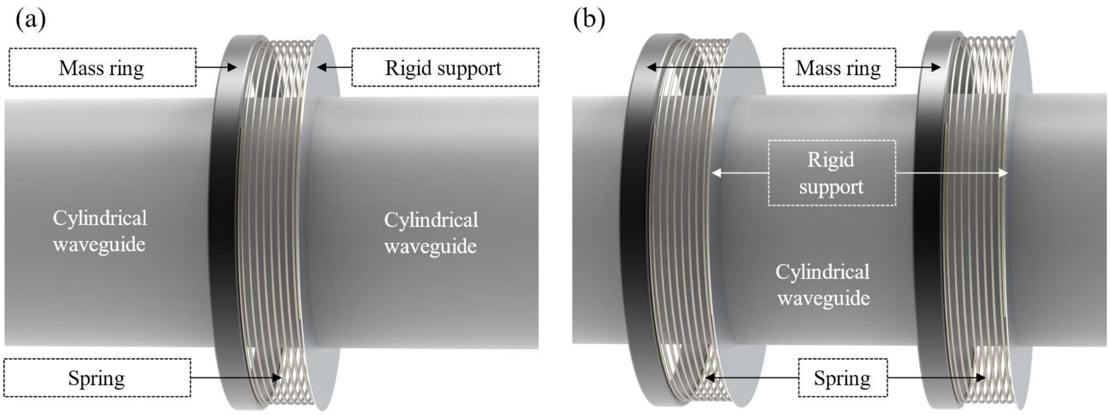

FIG. 4.1. Schematic representation of the longitudinal waveguide system with (a) single resonator and (b) two resonators. The stiffness of the spring is time-modulated. The rigid support is clamped into the section of the waveguide.

We also conducted finite element (FE) simulations by utilizing the commercial software COMSOL Multiphysics 5.5. The parameters of the system κ_0, κ_M, S, l, ω and Ω are determined via a genetic algorithm (see Part III.1) to optimize the nonreciprocal wave propagation performance.

We analyzed the spectrum of the transmitted waves with a series of parameters optimized at 1007Hz, and the results are shown in **Fig. 4.2**. The corresponding parameters are $m = 0.8529\text{kg}$, $\Omega/2\pi = 80\text{Hz}$, $\kappa_0 = 30\text{MPa}$, $\kappa_M = 3\text{MPa}$, $S = 0.0258\text{m}^2$ and $l = 1.772\text{m}$; the material's properties of the waveguide are $E = 2\text{GPa}$, $\rho = 910\,\text{kg/m}^3$ and $v = 0.319$. Numerous harmonic mode amplitudes A_n^+ are calculated, but only those from $-$2nd to $+$2nd orders are plotted. Good agreement was found between the numerical results and the theoretical wave amplitudes from TMMs.

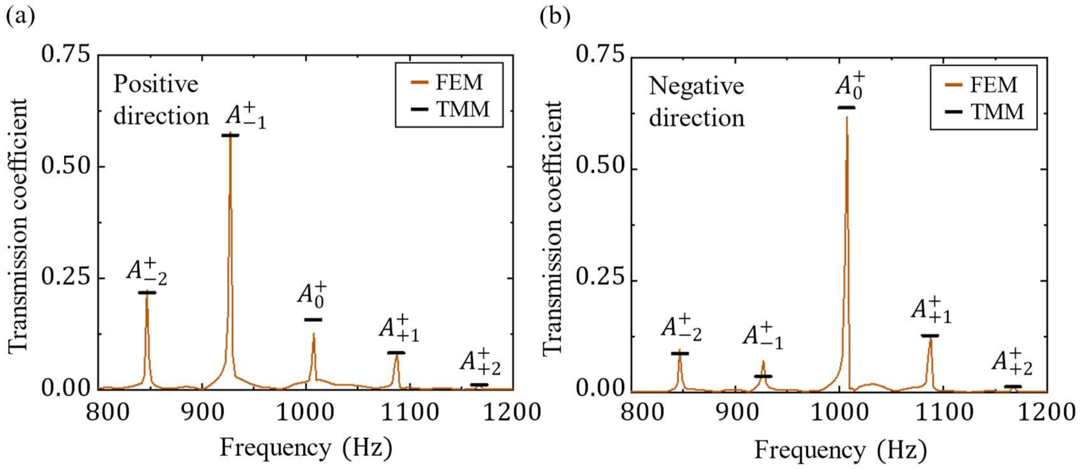

FIG. 4.2. Analytical and numerical harmonic analysis of transmission coefficient A_{n}^{+} (a) in the positive direction and (b) in the negative direction. The operational frequency is 1007Hz.

Bringing this device design into a physical realization presents many technical challenges. Consequently, we decided to conduct a more feasible design by considering a system for flexural waves.

II.2. TMM for flexural waves

Following the same theoretical methodology for P-waves, we developed a TMM based model for flexural waves. **Figure 4.3** displays the corresponding schematic model with two cascaded mass-spring resonators. The incident transmitted and reflected fields of out-of-plane displacement are denoted by w_i, w_t and w_r.

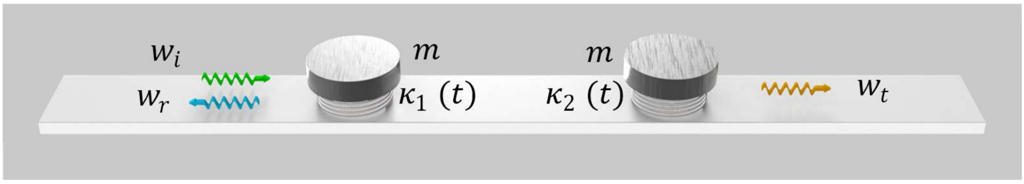

FIG. 4.3. The schematic model for the cascaded mass-spring resonator system where m is mass of the resonator, κ is its stiffness, w_i is the incident wave, w_r is reflected wave, and w_t is transmitted wave.

We first consider the case where only one resonator is located at $x = 0$, whose stiffness is time-modulated as $\kappa(t) = \kappa_0 + \kappa_M \cos(\Omega t + \phi)$. The governing equations for flexural waves in the host plate can be expressed in the following forms, respectively,

$$I \frac{\partial^2}{\partial x^2}\left[E \frac{\partial^2 w(x,t)}{\partial x^2}\right] + h \frac{\partial}{\partial t}\left[\rho \frac{\partial w(x,t)}{\partial t}\right] = 0 \tag{4.20}$$

where E, ρ, h and I are Young's modulus, density, thickness and section moment of inertia of the plate. $I = h^3/12(1-\upsilon^2)$, where υ is the Poisson's ratio. w is the out-of-plane displacement of the plate. At low frequencies with time modulation, the general solution of the displacement field for Eq (4.20) yield in the following Floquet form as the sum of harmonic propagating and evanescent modes,

$$w = \sum_{n=-\infty}^{+\infty} \left(A_n e^{-jk} + B_n e^{jkx} + a_n e^{-kx} + b_n e^{kx}\right) e^{j(\omega+n\Omega)t} \tag{4.21}$$

The dispersion relation in such case is known as $k = (EI/\rho h\omega^2)^{-\frac{1}{4}}$. Similarly, the displacement of the mass in the resonator should be accounted,

$$w^m(t) = \sum_{n=-N}^{N} w_n^m e^{j(\omega+n\Omega)t} \tag{4.22}$$

At $x = 0$, the following conditions of continuity[11] are applied for the out-of-plane displacement w, the slope φ, the moment M and the shear force V,

$$\begin{cases} w^+ - w^- = 0 \\ \varphi^+ - \varphi^- = 0 \\ M^+ - M^- = 0 \\ V^+ - V^- = F \end{cases} \tag{4.23}$$

The positive and negative signs mean right and left of the position $x = 0$ on the beam. The slope, the moment and shear force are,

$$\begin{cases} \varphi = \dfrac{\partial w}{\partial x} \\ M = EI\dfrac{\partial^2 w}{\partial x^2} \\ V = -EI\dfrac{\partial^3 w}{\partial x^3} \end{cases} \tag{4.24}$$

where $I = h^3/12(1-\upsilon^2)$ is the section moment of inertia, and E and υ are the Young's modulus and Poisson's ratio of the waveguide, respectively.

At $x = 0$, $F(0) = (w^+(0) - w^m)\kappa(t)$, similarly, the spring stiffness $\kappa(t)$ can be decomposed in the generalized Floquet form,

$$\kappa(t) = \sum_{p=-1}^{1} \kappa_p e^{ip\Omega t+\ \ p} \tag{4.25}$$

We also have the equation of motion of the mass,

$$m\frac{\partial^2 w^m}{\partial t^2} = F(0) \tag{4.26}$$

The dispersion relation in this study is known as $k_j = [EI/\rho h(\omega + j\Omega)^2]^{-\frac{1}{4}}$, where ρ is the density of the waveguide.

By inserting Eqs (4.21) and (4.25) to Eqs (4.23-24) and (4.26), and performing the similar math manipulation as the last section to eliminate the sign of sum and the time-related term,

$$\begin{cases} A_n^- + B_n^- + a_n^- + b_n^- - A_n^+ - B_n^+ - a_n^+ - b_n^+ = 0 \\ -iA_n^- + iB_n^- - a_n^- + b_n^- + iA_n^+ - iB_n^+ + a_n^+ - b_n^+ = 0 \\ -A_n^- - B_n^- + a_n^- + b_n^- + A_n^+ + B_n^+ - a_n^+ - b_n^+ = 0 \\ -EIk_n^3(iA_n^- - iB_n^- - a_n^- + b_n^- - iA_n^+ + iB_n^+ + a_n^+ - b_n^+) \\ \quad = \sum_{N'} \left(A_{n'}^- + B_{n'}^- + a_{n'}^- + b_{n'}^- - w_{n'}^m\right)\kappa_{n-n'} e^{i\phi_{n-n'}} \\ -\sum_{N'} \left(A_{n'}^- + B_{n'}^- + a_{n'}^- + b_{n'}^- - w_{n'}^m\right)\kappa_{n-n'} e^{i\phi_{n-n'}} = m(\omega + n\Omega)^2 w_n^m \end{cases} \tag{4.27}$$

Similarly, Eqs (4.27) can be reformed to matrixes,

$$\begin{bmatrix} \boldsymbol{I} & \boldsymbol{I} & \boldsymbol{I} & \boldsymbol{I} & \boldsymbol{O} \\ -i\boldsymbol{I} & i\boldsymbol{I} & -\boldsymbol{I} & \boldsymbol{I} & \boldsymbol{O} \\ -\boldsymbol{I} & -\boldsymbol{I} & \boldsymbol{I} & \boldsymbol{I} & \boldsymbol{O} \\ -i\boldsymbol{\Lambda} - \boldsymbol{K} & i\boldsymbol{\Lambda} - \boldsymbol{K} & \boldsymbol{\Lambda} - \boldsymbol{K} & -\boldsymbol{\Lambda} - \boldsymbol{K} & \boldsymbol{O} \\ -\boldsymbol{K} & -\boldsymbol{K} & -\boldsymbol{K} & -\boldsymbol{K} & \boldsymbol{O} \end{bmatrix} \begin{bmatrix} \boldsymbol{A}^{-,N} \\ \boldsymbol{a}^{-,N} \\ \boldsymbol{B}^{-,N} \\ \boldsymbol{b}^{-,N} \\ \boldsymbol{O} \end{bmatrix} = \begin{bmatrix} \boldsymbol{I} & \boldsymbol{I} & \boldsymbol{I} & \boldsymbol{I} & \boldsymbol{O} \\ -i\boldsymbol{I} & i\boldsymbol{I} & -\boldsymbol{I} & \boldsymbol{I} & \boldsymbol{O} \\ -\boldsymbol{I} & -\boldsymbol{I} & \boldsymbol{I} & \boldsymbol{I} & \boldsymbol{O} \\ -i\boldsymbol{\Lambda} & i\boldsymbol{\Lambda} & \boldsymbol{\Lambda} & -\boldsymbol{\Lambda} & -\boldsymbol{K} \\ \boldsymbol{O} & \boldsymbol{O} & \boldsymbol{O} & \boldsymbol{O} & \boldsymbol{T} - \boldsymbol{K} \end{bmatrix} \begin{bmatrix} \boldsymbol{A}^{+,N} \\ \boldsymbol{a}^{+,N} \\ \boldsymbol{B}^{+,N} \\ \boldsymbol{b}^{+,N} \\ \boldsymbol{w}^{m,N} \end{bmatrix} \tag{4.28}$$

where $\Lambda_{n,m} = \chi_n \delta_{n,m}$, $K_{n,m} = \psi_0 \delta_{n,m} + \psi_{-1} \delta_{n,m+1} + \psi_1 \delta_{n,m-1}$, $T_{n,m} = \xi_n \delta_{n,m}$, in which χ_j is EIk_j^3, ψ_z is $\kappa_z e^{i\phi_z}$ ($z = -1, 0$ or 1), and ξ_j is $m(\omega + j\Omega)^2$. $\boldsymbol{O}$ is the zero matrix or vector, $\boldsymbol{A}^{+,N}$, $\boldsymbol{a}^{+,N}$, $\boldsymbol{B}^{+,N}$, $\boldsymbol{b}^{+,N}$, $\boldsymbol{A}^{-,N}$, $\boldsymbol{a}^{-,N}$, $\boldsymbol{B}^{-,N}$ and $\boldsymbol{b}^{-,N}$ are of the form $\boldsymbol{X}^{s,N} = \langle X_{-N}^s, \dots, X_0^s, \dots, X_{+N}^s \rangle^T$, $\boldsymbol{X}$ can be either $\boldsymbol{A}$, $\boldsymbol{a}$, $\boldsymbol{B}$ or $\boldsymbol{b}$ and s takes either the sign "−" or "+", $\boldsymbol{w}^{m,N} = \langle w_{-N}^m, \dots, w_0^m, \dots, w_{+N}^m \rangle^T$, $\boldsymbol{I}$ is unitary matrix. δ is the Kronecker function.

The total dimension is $5(2N + 1)$. We denote the matrix at the left side by $\boldsymbol{M}^-$ and that at the right side by $\boldsymbol{M}^+$, finally we have the transfer matrix $\boldsymbol{M}$ as we do in Eq (4.15). The w^m terms are not needed in the transfer matrix, so we eliminate them by delete the last $2N + 1$ rows and the last $2N + 1$ lines in $\boldsymbol{M}$. Thus, the definition of $\boldsymbol{M}$ is now,

$$\begin{bmatrix} \boldsymbol{A}^{+,N} \\ \boldsymbol{a}^{+,N} \\ \boldsymbol{B}^{+,N} \\ \boldsymbol{b}^{+,N} \end{bmatrix} = \boldsymbol{M} \begin{bmatrix} \boldsymbol{A}^{-,N} \\ \boldsymbol{a}^{-,N} \\ \boldsymbol{B}^{-,N} \\ \boldsymbol{b}^{-,N} \end{bmatrix} \tag{4.29}$$

With manipulation similar to Eq (4.18), we get the transfer matrix $\boldsymbol{M}^g$ in the bi-resonator system with the distance l between two resonators. According to the generalized solution in Eq (4.21), the transfer matrix for the bare waveguide between the two resonators $\boldsymbol{M}^w$ is,

$$\boldsymbol{M}^w = \begin{bmatrix} \boldsymbol{\Gamma} & \boldsymbol{O} & \boldsymbol{O} & \boldsymbol{O} \\ \boldsymbol{O} & \boldsymbol{H} & \boldsymbol{O} & \boldsymbol{O} \\ \boldsymbol{O} & \boldsymbol{O} & \boldsymbol{\Gamma}^{-1} & \boldsymbol{O} \\ \boldsymbol{O} & \boldsymbol{O} & \boldsymbol{O} & \boldsymbol{H}^{-1} \end{bmatrix} \tag{4.30}$$

where $\boldsymbol{\Gamma} = \mathrm{diag}(e^{-ik_{-N}l}, \dots, e^{-ik_j l}, \dots e^{-ik_N l})$ and $\boldsymbol{H} = \mathrm{diag}(e^{-k_{-N}l}, \dots, e^{-k_j l}, \dots e^{-k_N l})$.

Finally, by applying the same matrix manipulation as we did in the Chapter 3, the global transfer matrix $\boldsymbol{M}^g$ can be converted into the global scattering matrix $\boldsymbol{S}$, $\begin{bmatrix} \boldsymbol{w}^{t,N} \\ \boldsymbol{w}^{r,N} \end{bmatrix} = \boldsymbol{S} \begin{bmatrix} \boldsymbol{w}^{i,N} \\ \boldsymbol{O} \end{bmatrix}$, where $\boldsymbol{w}^{t,N} = \begin{bmatrix} \boldsymbol{A}^{+,N} \\ \boldsymbol{a}^{+,N} \end{bmatrix}$, $\boldsymbol{w}^{r,N} = \begin{bmatrix} \boldsymbol{B}^{-,N} \\ \boldsymbol{b}^{-,N} \end{bmatrix}$ and $\boldsymbol{w}^{i,N} = \begin{bmatrix} \boldsymbol{A}^{+,N} \\ \boldsymbol{O} \end{bmatrix}$ refer to the transmitted, reflected and incident waves (**Fig. 4.3**).

In this theoretical model, several important approximations are made: the dimension of the resonators are not taken into account; we use the plate model instead of beam model; and the material intrinsic damping is neglected.

II.3. FE modeling and low-reflecting boundary (LRB) in COMSOL Multiphysics

Regularly, we had to check the validity of the TMM model for flexural wave via FE simulation in COMSOL. However, the existing options in structural module of COMSOL are not adapted to our situation. First, the perfectly match layer (PML) does not work in transit calculations; secondly, the existing low-reflecting boundary only works efficiently for longitudinal waves. Without effective solution to suppress the reflection at the boundaries of our simulation domain, the only approach to consider in order to avoid the effect of reflection was to extend the geometric model according to the calculation duration. Under the known wave propagation speed, the reflected wave should not pass through the operational structure before the end of the calculation. Without doubt, this method is time and memory consuming.

Shen et al.[12] proposes a non-reflective boundary for Lamb waves, which is realized in another commercial software ANSYS using COMBIN14 spring–damper element. Since at low frequency, the flexural waves are highly similar to the non-symmetrical mode of Lamb waves, we decided to implement this approach in COMSOL Multiphysics.

The core of this approach is to connect the reflection-suppressing part of the waveguide to hard wall via damper element. In the original approach, the viscous boundary reaction stresses should satisfy the following conditions,

$$\begin{cases} \sigma_{xx} = -a\rho c_p \dfrac{\partial u_x}{\partial t} \\ \tau_{xy} = -b\rho c_s \dfrac{\partial u_y}{\partial t} \end{cases} \tag{4.31}$$

where the coefficients a and b are the damping parameters; they are equal to 1 at the vertical boundary (corresponding to the extremity of the beam) and follow a function f(x) along the upper and lower boundaries (corresponding to the upper and lower surfaces of the beam) u_x is the particle velocity of P-waves and u_y is that of S-waves. In line with the definition of damping, we derived the damping per unit area, which is compatible with the spring foundation function,

$$\begin{cases} da_p = a\rho c_p \\ da_s = b\rho c_s \end{cases} \tag{4.32}$$

The $f(x)$ function represents a half Hanning window,

$$f(x) = \frac{\delta}{2}\left[1 - \cos\left(\frac{\pi x}{n\lambda}\right)\right], x\epsilon(0, n\lambda) \tag{4.33}$$

where λ is the wavelength at the operational frequency, n is a positive integer. Normally, it is recommended to let $n \geq 2$. δ is the coefficient to be tuned. In **Fig 4.4**, we tested the performance of this non-reflective boundary on the bare waveguide in the frequency domain calculation. The red curve represents the transmission coefficient on the waveguide equipped with these boundaries, and the black curve represents that on the waveguide with PML for comparison. The results show that the performance of our

LRB is very similar with that of PML, which means that the reflection with these boundaries is very weak.

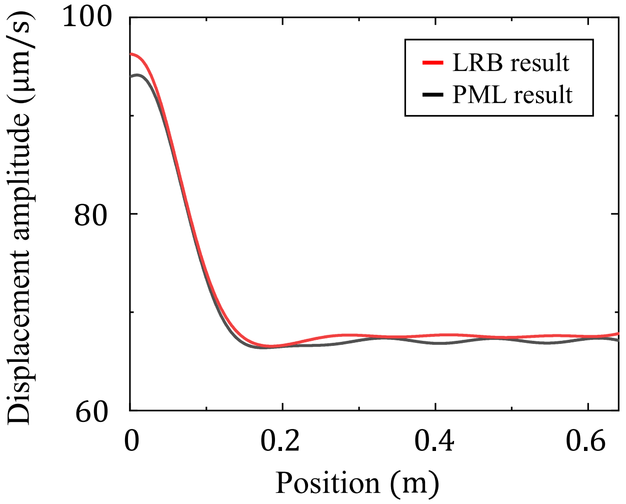

FIG. 4.4. Performance comparison between the LRB and PML at 126Hz with flexural wave propagation. The excitation is located at $x = 0$. The layer length for LRB and PML both is 8 wavelengths.

Further, we launched a time-domain calculation with the time-modulated structure on the waveguide. We adopted the parameters from the initial result of genetic algorithm (GA) optimization: $\Omega/2\pi = 30$ Hz, $m = 2.5$g, $k_0 = 1000$ N/m, $k_m = 480$ N/m, and $l = 50$ mm. The time modulation of the effective stiffnesses causes frequency conversions that can be characterized by analyzing the wave spectrum. For the incident harmonic wave at 132 Hz, we analyzed the spectrum of transmitted waves, and the results are shown in **Fig 4.5 (b)** and **(c)**. It is observed that our theory agrees well with the numerical model.

III. Experimental realization

III.1. Genetic-algorithm-based parameters tuning

The optimized parameters were adopted in the experimental realization. The parameters optimization was based on considering the host beam made of (polylactic acid) PLA where its mechanical properties are Young's modulus $E = 3.44$GPa, the density $\rho = 1086.3\ \mathrm{kg/m^3}$ and Poisson's ratio $\nu = 0.35$ and the phase shift between the time modulations of two resonators: $\phi = \pi/2$. The parameters to be tuned are the beam thickness h, the beam width d, the distance between the centers of two resonators l, the effective mass m, the static effective stiffness k_0, the additional stiffness k_m, the operational frequency ω and the modulation frequency Ω.

Also, the following constraints are to be considered:

- First, the beam thickness h should be inferior to 4mm to consider flexural waves at the operating wavelength.
- Second, the additional stiffness $\mathrm{k_m}$ should be smaller than half of the static effective stiffness $\mathrm{k_0}$ to make the time modulation realizable.
- Last, the operational frequency $\omega/2\pi$ should be lower than 200Hz. The principle of the nonreciprocity in this structure determines that ω should be near the resonance angular frequency ω_c. Then, according to the known expression $\omega_c = \sqrt{k_0/m}$, a high ω_c would affects its feasibility. Briefly, the SMR is designed for low frequencies.

Considering that there are numerous parameters, we used the GA to perform the optimization. A genetic algorithm (GA) is a meta-heuristic inspired by the process of natural selection that belongs to the larger class of evolutionary algorithms. A fitness function which outputs the optimization index with the parameters above as inputs is necessary for the GA. In our fitness function, the bandwidth of nonreciprocity and the maximal amplitude differences between the transmission coefficients in two propagation directions were considered. The fundamental modes of the transmission coefficients are denoted as $\mathrm{A}_{0,p}^{+}(\omega)$ in the positive direction and $\mathrm{A}_{0,n}^{+}(\omega)$ in the negative direction. Then, the definition of the bandwidth of nonreciprocity $\Delta \mathrm{f_A}$ is shown in **Fig 4.6**. The asymmetry curve is denoted $\Delta\mathrm{A}_0^{+}(\omega) = \mathrm{abs}[\mathrm{A}_{0,p}^{+}(\omega)\text{-}\mathrm{A}_{0,n}^{+}(\omega)]$, thus our fitness function is,

$$F = -\Delta f_A * \max(\Delta A_0^{+}) \tag{4.34}$$

The GA function in MATLAB generates a specific quantity of first-generation samples with random parameters, then selects those of specific quantity (population size) with better fitness and give birth to the next generation. The process of generation can be understood as switch one or several parameters. There is a mutation function in this algorithm, which leads to the appearance of non-existing parameters during the birth of samples under specific probability (mutation rate). When the average fitness of the latest generation is close enough to the best fitness in this generation, the GA function is ended and returns the parameters in which the best fitness is achieved.

To some extent, the GA is function of contingency. Also, the result got from GA can be logically demonstrated to be the real best result. So, to strengthen the stability of the MATLAB GA function, we enlarge the default population size and mutation rate, so that the function gets less chance to be trapped in a local minimum.

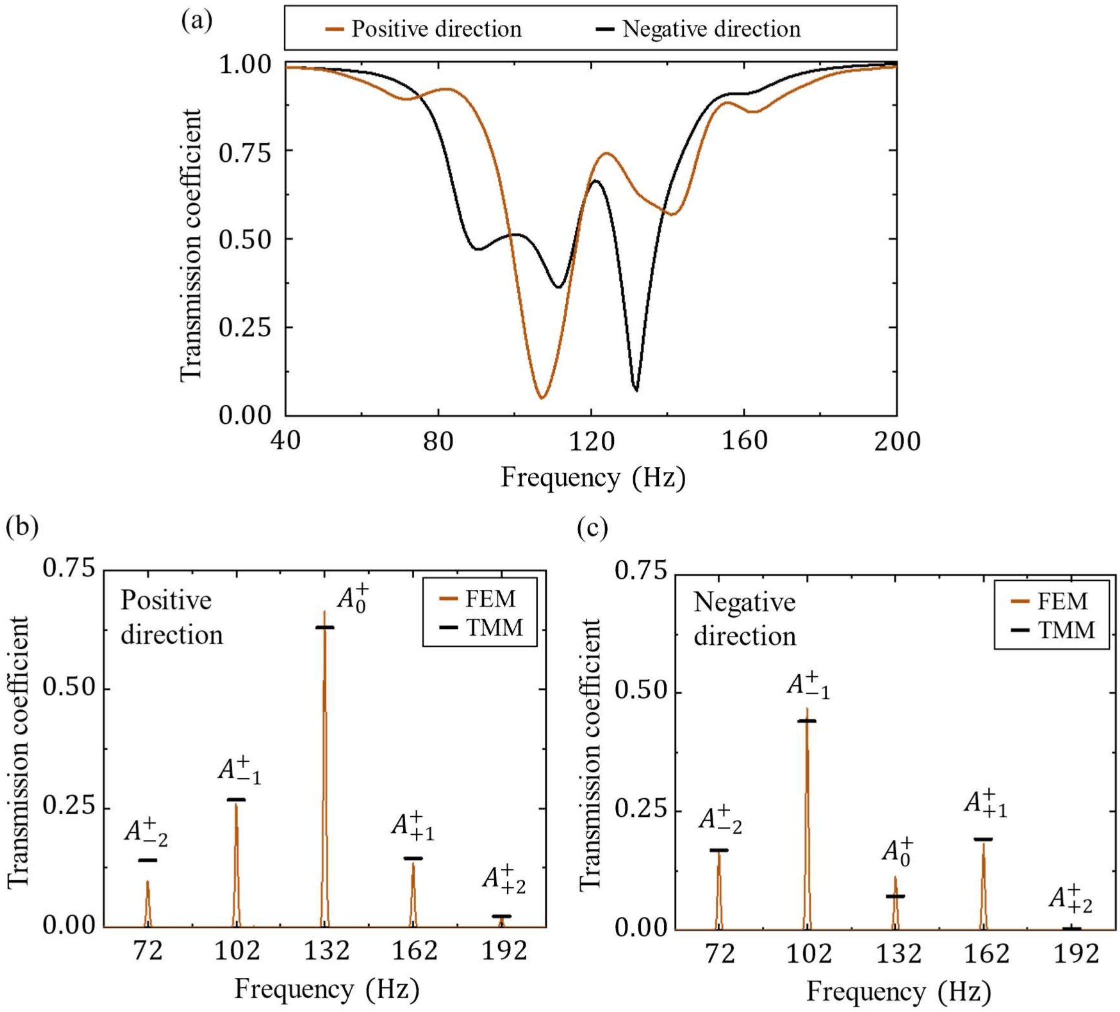

FIG. 4.5. (a) The transmission coefficient in the frequency domain in two propagation directions with the initial tuned parameters via GA. (b) and (c) Analytic (TMM) and numerical results of spectrum of the transmitted waves at for an incident wave at an operational frequency of 132Hz.

We round the parameters returned from the GA function because the precision of these parameters is not reachable in fabrication and experiment. These initially tuned parameters are $\Omega/2\pi = 30\ \mathrm{Hz}$, $m = 2.5\mathrm{g}$, $k_0 = 1000\ \mathrm{N/m}$, $k_m = 500\ \mathrm{N/m}$, $l =$

50 mm, $h = 3$ mm and $d = 20$ mm. **Fig 4.5(a)** displays the transmission coefficient in the frequency domain in opposite propagation directions with the above parameters. **Fig 4.5(b)** and **(c)** represents the spectra of the transmitted waves. Numerous harmonic mode amplitudes $\mathrm{A}_{\mathrm{n}}^{+}$ are calculated, but only those from -2nd to $+2$nd orders are plotted. The result from the FE simulations (Part II.4) is also plotted in **fig 4.5(b)** after being post-processed with fast Fourier transform (FFT).

III.2. SMR structure conception

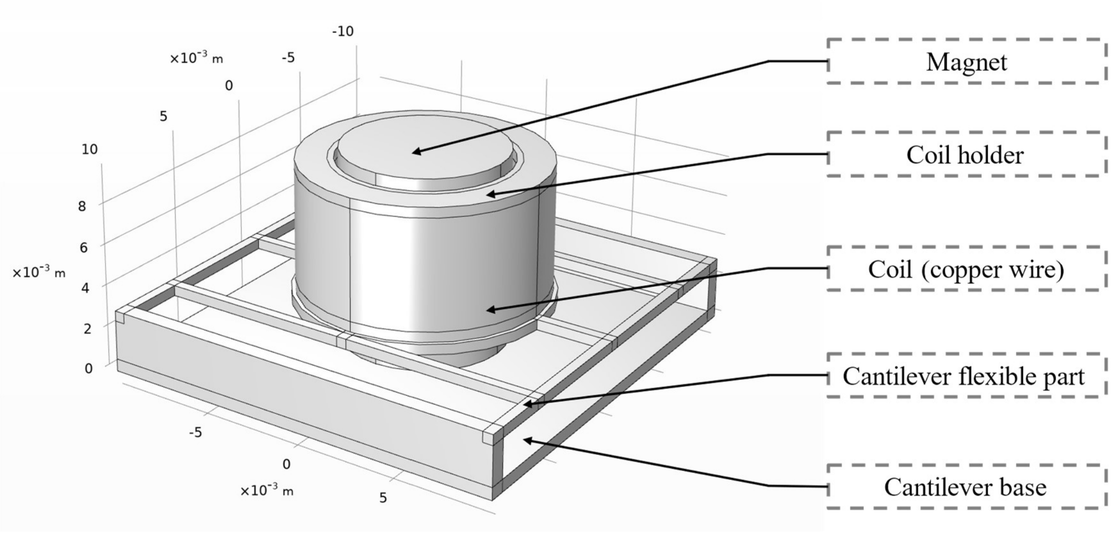

FIG. 4.6. A modified MSER design with reticulated cantilever.

Inspired by the work of Chen et al.[2] and Wang et al.[1], we decide to adopt the coil-cantilever-magnet system as our SMR. **Fig. 4.6(a)** displays the original design of Chen et al.[2] In their design, cantilevers are installed along the host beam, and the bases of cantilever, with which the SMR is bonded to the host beam, are far away from the magnet and coil, so the dimension of the cantilever is much larger than that of coil. Lengthening the cantilever is a good way to lower the effective stiffness to a desired level, but it also enlarges the dimension of the resonators, which falsely correlate with our theoretical model. Meanwhile, lengthening the cantilever reduces its torsional stiffness, thus, an undesired torsion resonating mode is likely to be found near the operating frequency. **Fig. 4.6(b)** displays a modified SMR design, where a reticular cantilever is considered. However, this design requires the section of the cantilever to be fabricated at the micro-scale which could be challenging by our 3D printer.

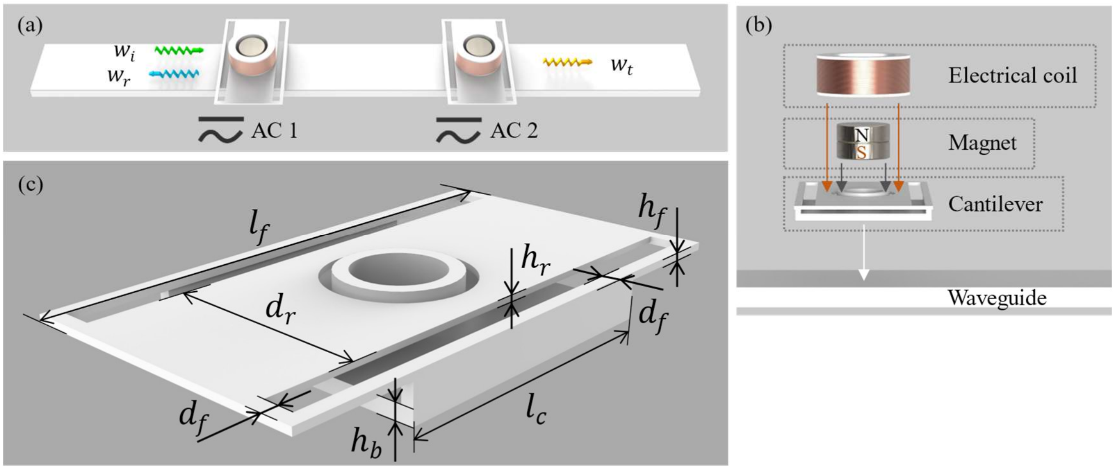

FIG. 4.7. (a) Experimental realization of the cantilever-magnet-coil system. (b) Schematic design of the coil-cantilever-magnet resonator system. (c) The detailed structure of the cantilever and the dimensions.

Fig. 4.7(a) shows the physical realization of this system where the resonator is made of a flexible cantilever in which a permanent magnet is fixed to the base of cantilever, and a coil is fixed to the flexible part of cantilever (**Fig. 4.7 (b)**). The structure (except the coil wiring and the magnet) is made of PLA material, same as the host beam, thus sharing the same mechanical properties. The detailed structure of the cantilever is shown in **Fig. 4.7(c)**. The base of the cantilever ensures the mechanical force transmission between the MSER and the host beam, and its length l_c is actually equivalent to the structure dimension mentioned in our 2D theoretical model. This force is expected to be evenly distributed on the junction area with the host beam. Therefore, the base thickness h_b is determined to be 1mm; the l_c is 20mm, the same as the host beam width d, so that the projection of the cantilever base is of square shape which allows a large electrical circle coil being tangent with the square size. Unlike the solution of Chen et al.[2], we proposed an innovative conception of the flexible part, which is to plant thin rib plate with thickness h_r and width d_r in the frame with section height h_r, section width d_r and frame length l_f. In this way, the profile of the flexible part is extended to be wider than the host beam to get producible dimensions of the structure pursuing the desired effective stiffness, while the force can still be quasi-uniformly conducted to the host beam via the cantilever base. The advantage of this design is that, first, the first resonance mode of the structure (the out-of-plane mode) is well separated from the second one that is undesired in the frequency spectra; second, under the 0.1mm fabrication precision limitation, the precise adjustment of the effective stiffness by tuning h_r, d_r, h_f, d_f and l_f is still realizable; last, the cantilever base supports the flexible part and the magnet at the same time in a tiny area, so the force distribution on the host beam is of mild homogeneity. The coil frame was designed to be as thin as possible to leave room for the copper coil wiring, and the magnet is Neodymium-based and it is coaxial and concentric with the coil. The magnetic pole of the magnet is on top-and-bottom disposition.

When no temporal modulation is applied, the coil-cantilever-magnet resonator behaves as a simple MSR with constant mechanical properties. Due to the complicated design of our cantilever resonator, the equivalent effective spring stiffness and mass can be evaluated via eigenfrequency study by numerical simulation using FE method. We used COMSOL Multiphysics 5.6 to perform such simulation. An eigenfrequency analysis is conducted on the cantilever resonator, from which the effective mass and stiffness were extracted. A late-stage example is shown in **Fig 4.8**, which presents the two first resonance modes of the cantilever where the first mode has an out-of-plane vibrational motion at 115Hz while the second mode has a flexural vibration in the lateral direction at 150Hz. Table 3.1 summarizes the properties of these two resonance modes. The detailed dimensions of the structure are as follows.

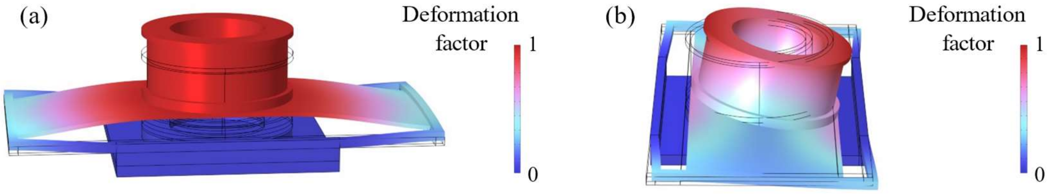

FIG. 4.8. (a) The shape and displacement field of the resonance modes of the cantilever: out-of-plane mode (1st mode) (a), and the flexural lateral mode (the 2nd mode) (b).

Mode index	Eigenfrequency (Hz)	Effective modal mass (g)	Effective modal stiffness (F/m)
1	115.26	3.04	1593.01
2	149.77	1.57	1393.40

TABLE. 4.1. Frequency, and effective mass and stiffness of the two first resonance modes of the resonator.

It is well observed that on the first resonance mode of the coil-cantilever-magnet structure, the displacement of the coil is mainly out-of-plane, the cantilever and the coil can be considered as the spring and the mass respectively. When the displacement of coil is relatively small, the out-of-plane force on the coil has a linear relationship with the displacement, respecting the Hooke's law. Also, the undesired 2nd resonance mode is well separated from the 1st one with an interval of over 30 Hz.

As for the temporal modulation, it is realized via the electromagnetic force between the coil and the magnet. When applying an AC to the coil, an attraction or repulsion force, depending on the current direction and magnetic pole orientation of magnet, appears between the magnet and the coil. We evaluated the necessary electrical current and the properties of magnet and coil for the desired κ_m via FE simulation using COMSOL Multiphysics (magnetic field study in AC/DC modules). In a 2D axisymmetric model, we varied the relative axial position between the coil and the magnet (the distance between their centers) and calculated the axial electromagnetic force with defined effective current in the coil. We show here a late-stage numerical evaluation for example. The number of copper wire windings of the coil is 320. The axial remanence of the magnet is 1.25 T. The magnet and the wiring parts of the coil have the same height 5.1mm. The diameter of the magnet is 8mm and the inner diameter of the coil wiring is 10mm while the outer one is 13mm. Figure **4.9(a)** displays the equivalent stiffness κ_m under various effective currents and figure 4.9(b) displays the electromagnetic force with various relative position (coil displacement) under 0.32 A. In this test, the κ_m reached is about $200\ \mathrm{N/m}$.

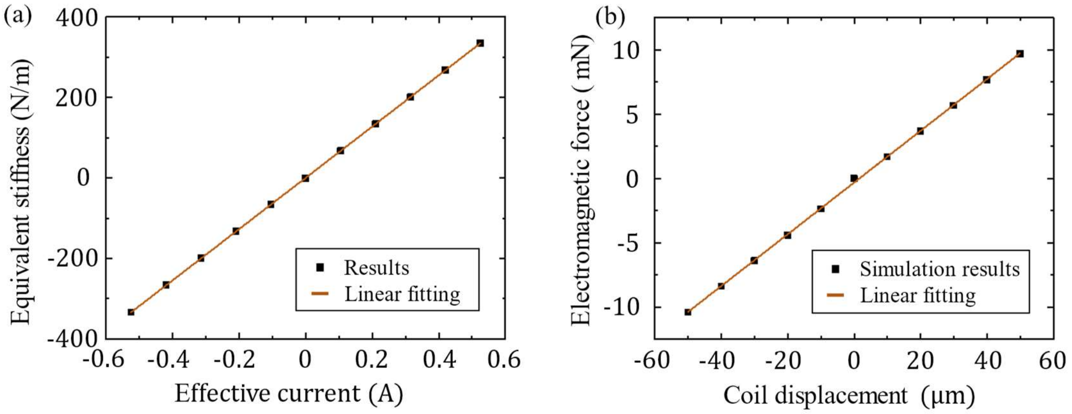

FIG. 4.9. (a) Linearly fitted equivalent stiffness based on FE simulation results under various effective current. The negative sign of effective current means the direction of current is reversed. The slop of the linear fitting on the results is $637\ \mathrm{N/(m \cdot A)}$. (b) FE simulation result of the axial electromagnetic force between the coil and the magnet as function of the displacement. When the coil displacement equals to 0, the centers of coil and magnet coincide. The effective current in the coil is $0.315\ \mathrm{A}$. The slop of the linear fitting on the results is $201\ \mathrm{N/m}$.

It is well observed that the electromagnetic force has a linear correlation with the relative displacement between the magnet and the coil when the displacement amplitude is relatively small. Also, the equivalent stiffness has a linear correlation with the effective current. So, an additional stiffness, which could be positive or negative, is provided by the magnet-coil design and can be linearly superposed with the static stiffness of the coil-cantilever structure. Consequently, we can dynamically change the total stiffness by varying the AC applied to the coil.

In the initial conception of the MSER, the objective effective mechanical properties of the structure (κ_0, κ_m and m) are from the results of the GA optimization. Several huge modifications are adopted due to the complicated situations during the fabrications.

III.3. Host beam construction

The construction of the host beam is the first tough challenge we encounter. As it is stated above, due to the features of SMR, its operational frequency tends to be lower than 200 Hz, and here we target an operating frequency of 100 Hz. In the PLA beam whose width and thickness are 20mm and 3mm, respectively, the wavelength is about

0.3m. A large wavelength leads to considering a long waveguide. First, the operational part of the beam will be long, because of the distance between the excitation, the structure and the measurement point should be at least half of wavelength, and one wavelength is recommended. Then, the reflection suppressing part will also be long. In the above part, we have introduced a low-reflecting damping layer in the FE model to suppress the wave reflections. In the experiment, the reflection suppressing part (with the Blue Tack damping adhesive) will be longer than that in the FE model to attend similar performance (2 wavelengths necessary in the FE model).

To be brief, the waveguide will be uncommonly long, which is extremely inconvenient for its transportation and handling. So, we decided to construct it on site with a 3D printer. However, the maximal dimension permitted by this 3D printer is only 180mm. Our solution was to glue numerous 180mm-long beam together by cyanoacrylate. We presumed that the cyanoacrylate layer among the beams would not lead to considerable reflection, because when getting concreted, the mechanical properties of cyanoacrylate are not that far from those of PLA since both are polymeric substance. For the propose of solid conjunctions, we designed a stairs shape beam unit. With such design, the total bonding area between the beam units is well enlarged for a strong hard junction.

We fabricated and bonded 18 beam units of 180mm (effective length 170mm), and the final length of the host beam is about 3m, in which the waveguide part is 0.8m and all the rest is reflection suppressing parts with attached damping adhesive (Blu Tack). The final host beam was placed on a damping table and padded with sponge on the two damping ends.

Since the host beam is uncommonly long, its torsional stiffness is weak. Additionally, the boundary is free on the upper side, so it is very easy to excite the torsion mode in this host beam. Our solution was using circular piezoelectric chip of 28mm diameter (STEMINC SMD28T21F1000R) and make the center of circle coincide the midline of the host beam. As is known, the diameter of piezoelectric chip here is large than the width of host beam, so the displacement of the beam could be less affected by the modal shape of the piezoelectric chip at low frequency.

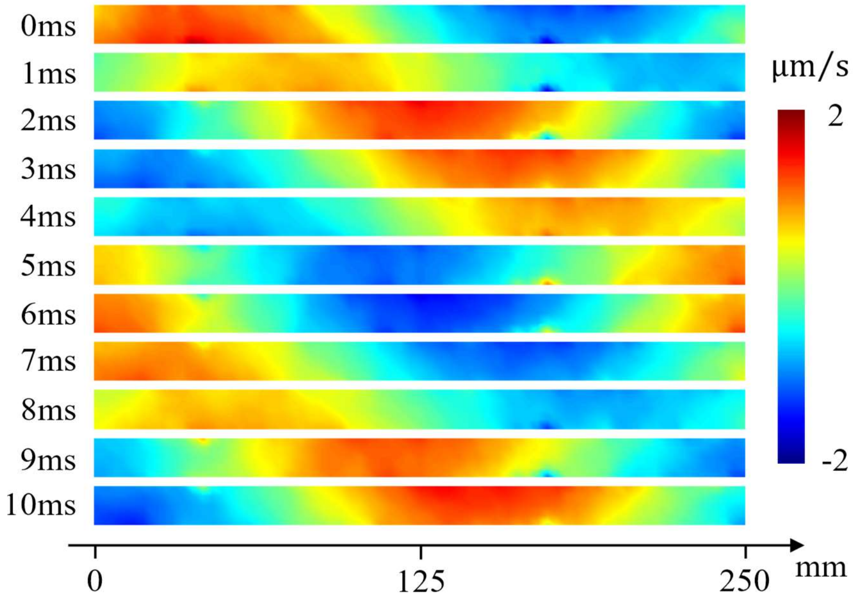

FIG. 4.10. The measurement results of amplitudes on bare beam from 0 ms to 10 ms using the laser vibrometer at 134Hz. The sampling covers 250mm length of the waveguide.

To verify the functionality of the reflection suppression, we tested the waveshape by scanning an area covering over a half of the wavelength. **Fig 4.10** displays the measurement velocities of bare beam via laser vibrometer at 134Hz from 0ms to 10ms, where the traveling wave can be well observed. The low frequency at which no standing wave is observed is 120Hz. Since we could no longer extend the host beam due to the limitations of the dimension of the damping table, we decided to modify the experiment model to let the nonreciprocity work over 120Hz.

III.4. Fabrication and characterization

Since we were able to complete the setting of the host beam for the low-frequency measurement, we were at the stage of sample fabrication of the resonators. In the early design, we planned to use electromagnets instead of permanent magnet. Fortunately, we find N38 neodymium disc magnet of 8mm diameter online. N38 is the magnet grade, which indicates that the remanence of the magnet is 1.25 T. And the actual thickness of the disc magnet is 2.55mm. A single magnet is too thin, so we used 2 of them to have a thickness of 5.1mm. Then we adjusted the size of the coil to be in line with the magnets.

Our 3D printer is not capable of printing dangling structures, so the cantilever cannot be directly 3D-printed. We divided the cantilever into two parts: the flexible part and the cantilever base. They would be 3D-printed separately then bonded together via cyanoacrylate glue. **Fig 4.11(a)** and **(b)** show the geometric model of these two parts. We can clearly observe two additional notches on the boards of the base and two additional bulges at the corresponding positions of the flexible part. This design was adopted for the convenience of positioning during the bonding. The positioning of the coil was done manually. With precise positioning, the magnet and the coil should be strictly coaxial and concentric. As for the coil, we had to fabricate a coil holder at first, then perform the copper wire winding manually. Due to the same reason as above, the coil holder had to be divided into two parts then bonded together manually too as shown in **Fig 4.11(c)**.

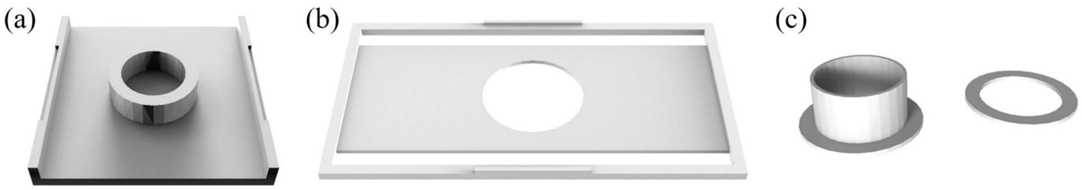

FIG. 4.11. (a) The geometric model of cantilever base with additional bulges on the bords. (b) The geometric model of cantilever base with additional notches on the bords. (c) The geometric model of coil holder before being bonded together.

In the copper wire mass, the winding number, the copper wire winding volume (outer profile) and the desired effective current strictly correlate with each other under the ideal winding condition, where the outer profile of the copper wire winding is flat and in line with that of coil holder, as shown in **Fig 4.7(b)**. However, this condition cannot be reached with manual winding. Disorder of winding could not be eliminated, which generates unexpected space and disturbs the outer profile of the coil. Hence, the electromagnetic field profile could be changed, then a different effective current would be needed to be applied on the coil. Since the only flexible parameter here was the effective current, we revised the strategy of fabrication: the specific coil mass would be the criterion of winding. We performed the winding till the objective coil mass is reached and we only adjusted the effective current to achieve the desired κ_m at the manipulating stage.

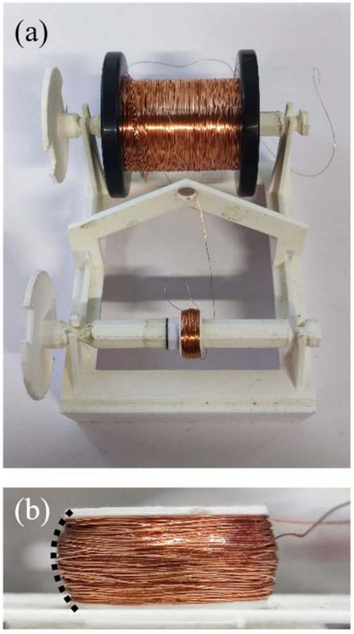

FIG. 4.12. (a) The winding tools. (b) The arc-like coil sample.

The manual winding without a tool made the copper wire strongly disordered, then the finished samples get irregular profiles, which could lead to a non-axisymmetric electromagnetic field, and lead to a non-out-of-plane electromagnetic force. To improve this, we designed and fabricated a winding tool, as shown in **Fig 4.12(a)**. This tool was composed of a base, a copper wire holder, a coil supporting axis and a copper wire limiter. The disorder in the coil winding was significantly reduced, and the coil shape got well regulated. The actual coil outer profile is arc-like, as shown in **Fig 4.12(b)**.

At the final stage of copper wire winding, we needed to scribble the cyanoacrylate glue on the winding surface to assist the fixing of the copper wire because there is no support from the coil holder since the copper wire winding surpasses the profile of the supporter. In fact, the glue leaded to discontinuous mass growing of the coil winding. So, at certain stage where the objective mass is surpassed, we removed the copper wire and weigh the coil at the same time to control its total mass. For each coil, about 10cm long is reserved at both two ends of copper wire. Extra cuts of thick wire had to be soldered to the two ends as connector because the copper wire is enameled.

Another significant parameter to be considered in the early fabrication stage is the coil impedance. During the early fabrication, we used the copper wire of 0.1mm diameter, and the designed winding number was 750. When we tested a finalized coil with a multimeter, we found that the coil resistance was over 60 Ohm. With this value, we did not have the power source and the amplifier that could drive a 60ohm coil with over 0.4 A effective current, which requires over 76 Vpp (peak-to-peak Voltage). So, we have to reconfigure the coil winding. As it is known, the electromagnetic field of the coil is largely related to the winding number and the current, and strongly related to the section area of copper wire. Enlarging this area is an efficient way to lower the effective resistance. So, we used the copper wire of 0.15mm diameter instead. With the thicker copper wire, the winding number is reduced to about 320 to maintain the designed mass of coil. The resistance of this coil is now approximately 15 Ohm. To reach the same electromagnetic field as the above case, we raised the effective current to 0.9A. Now, the necessary voltage to drive this coil is reduced to 44Vpp. In the actual measurement step, the effective current was lowered to 0.46A, because under 0.9A, the coil was rapidly overheated without any cooling measurement and the PLA coil holder could be melted down in seconds. Another reason is related to the temperature excursion effect, which will be discussed in the next section.

Afterwards, we also estimated the coil reactance X_L with the following equation,

$$X_L = \Omega L \tag{4.35}$$

where L is the inductance and Ω is the AC angular frequency (modulation angular frequency). The inductance L can be estimated with the following empirical formula,

$$L = \frac{f_k\left(\frac{2r_{coil}}{l_{coil}}\right) * \mu_0 * N_w^2 * S_{coil}}{l_{coil}} \tag{4.36}$$

where $f_k\left(\frac{2r_{coil}}{l_{coil}}\right) = -0.179\ln(x) + 0.647$, $\mu_0 = 4\pi \times 10^{-7}$ is the vacuum permeability, N_w is the winding number, S_{coil} is the section area of coil, l_{coil} is the length of coil and r_{coil} is the radius of coil.

With the above equations, the coil reactance X_L was estimated to be inferior to 5 Ohm under $\Omega/2\pi = 20$Hz, which is much smaller than the coil resistance.

Once a sample is fabricated, we had to test its resonance eigenfrequency. The objective was to keep its eigenfrequency between 110Hz and 120Hz so that the actual on-beam resonance frequency is over 130Hz, then the operational frequency can be higher than the reflection limitation of 120Hz (Fig 4.5). However, numerous factors brought in errors over the properties of samples, including the temperature during the 3D-printing process, the bonding quality and the positioning accuracy. It was challenging to fabricate a sample with the desired mechanical properties.

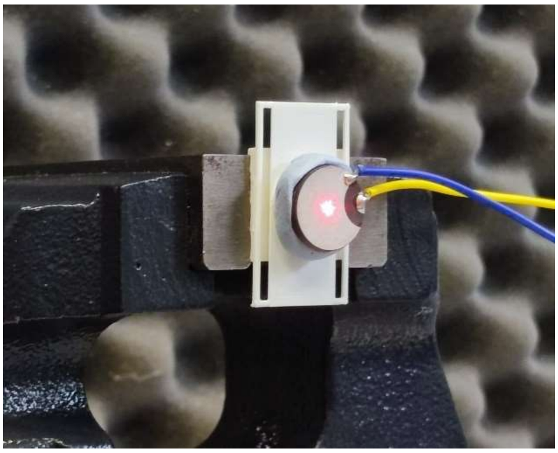

FIG. 4.13. Initial characterization setup. The piezoelectric chip is attached to a base coil holder then bonded to the cantilever. The damping adhesive is applied to adjust the effective mass. The red dot is the laser beam.

Initially, to perform the characterization, we imposed the excitation on the flexible part of cantilever by sticking a piezoelectric chip and a bare coil holder, as shown in **Fig 4.13**. We attached extra adhesive on the piezoelectric chip to make up the mass to be that of an actual coil. Then, we fixed the cantilever base, and use the laser vibrometer to measure its frequency response. However, this method requires for un-bonding and re-bonding parts on the flexible part of cantilever, which leads to fabrication errors for 2 extra times after the characterization (errors from the extra stiffness provided by cyano adhesive in un-bonding and second time bonding). Also, we risked destroying the sample when peeling off the piezoelectric chip from the cantilever. Thus, we moved to another method where we bond the complete sample onto the host beam and take advantage of the excitation on the beam. Considering the need of repeated installation, we used adhesive tapes between the samples and the host beam to protect the host beam.

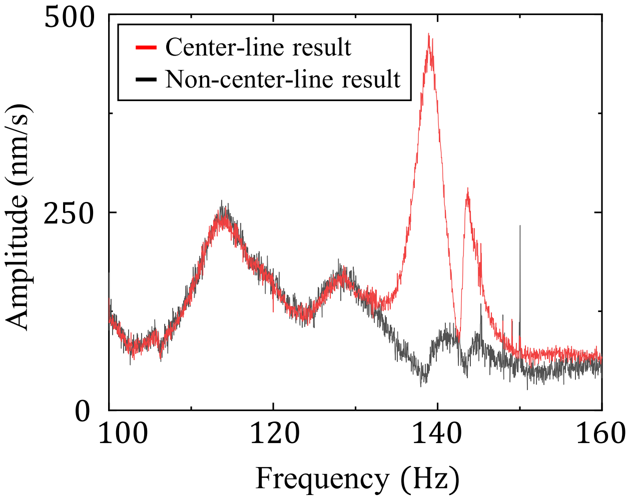

FIG. 4.14. Characterization results of one of the well-fabricated samples. “Center-line” means the measurement point is on the center line (the same orientation as the frame length l_f, refer to Fig 4.7(c)) of the resonator.

An example of characterization is displayed in Fig 4.15. The black curve shows the case where we put the measurement point on the center line of the resonator sample, by which the peak of first eigenfrequency (114Hz) of the resonator is displayed in the frequential response curve. As to the red curve, we put the measurement point away from the center line of the resonator sample, by which the peak of second eigenfrequency (139Hz) of the resonator is displayed in the frequential response curve. Once this sample is qualified by the characterization, another similar sample must be found to pair with it. But once the sample is not qualified due to large error of first eigenfrequency, we mainly adjust the frame length l_f (Fig 4.7(c)) in the next fabrication process to make it close to the targeted frequency (first eigenfrequency should be between 110Hz the 120Hz).

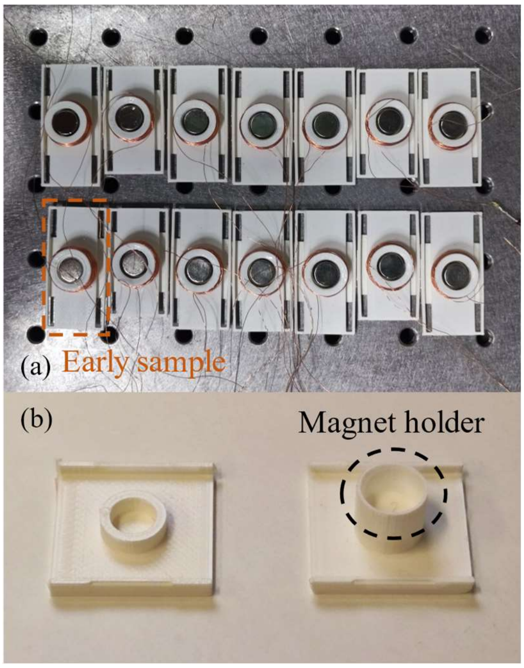

FIG. 4.15. (a) All the fabricated samples. The orange mark indicates an early sample with magnet holder and $d_f = 0.8\mathrm{mm}$. In all other samples, there is no magnet holder and $d_f = 1\mathrm{mm}$. (b) The evolution of the cantilever base.

We exhibit all the samples we have managed to fabricate in **Fig 4.15(a)**, which displays the evolutions of the geometric model of the sample. The most important adjustment is that we raised the section width d_f (**Fig 4.7(c)**) from 0.8mm to 1mm. This adjustment substantially improves the yield of 3D printing from 20% to 60%. Another important adjustment is that the magnet holder is removed. The magnet holder was designed in the early stage for positioning auxiliary purpose, but the outer diameter of the holder was very close to the inside diameter of the coil, which required harsh tolerance. Further, in the stage of bonding using glue, the glue could be easily spilled over from the junction area then stick the coil and the magnet holder together. Thus, we removed the magnet holder in the late batch of fabrication to leave some room for the positioning tolerance and cleaning the spilling cyanoacrylate glue. Finally, we managed to fabricate 2 similar samples whose first resonant eigenfrequency is between 114Hz and 115Hz.

III.5. Measurements

During the mid-stage of fabrication, we begun the measurement. The first challenge we encountered was to properly drive the coils. To drive the coil of 16 Ohm impedance (15

Ohm resistance and 5 Ohm reactance) with 0.4A effective current, we need a power source which provides 20Vpp output voltage and 2.6W output power. All our existing power sources adapt only high-impedance device like piezoelectric chip then cannot reach the 2.6W output power with low-impedance load, so an amplifier is indispensable. After a quick search, we chose the appropriate amplifier for the passive speakers. First, the impedance of passive speakers is usually 4 Ohm or 8 Ohm, which is very close to that of our coils, and this type of amplifier can output over 25W power with 8 Ohm load, so we presumed that it could output over 2.6W power with 16Ohm load. Secondly, the operational frequency range of this type of amplifier is at least from 20 Hz to 20 000 Hz, which fits our requirement. Last, this type of amplifier must have at least 2 independent channels, so one single amplifier is enough to drive two coils. It was discovered afterwards that this amplifier outputs different voltage levels with the same input levels in the two channels, so an offset had to be applied on the input of one of the channels.

Due to the performance limitation of the amplifier, when the output voltage level is much higher than the input voltage level, a strong distortion appears. To prevent this situation, we made the input voltage level (from the signal generator) as high as possible (10Vpp maximum) and used an oscilloscope to inspect the output wave. First, we connected the amplifier to the coil via an AC ammeter and adjusted the output of amplifier till the desired current was reached. Then, we reconnected the amplifier to the oscilloscope, maintaining the above output level, and inspected the output wave. **Fig 4.16** shows the output waves of two channels in the oscilloscope with $\pi/2$ phase shift while the inputs levels are both 1Vpp.

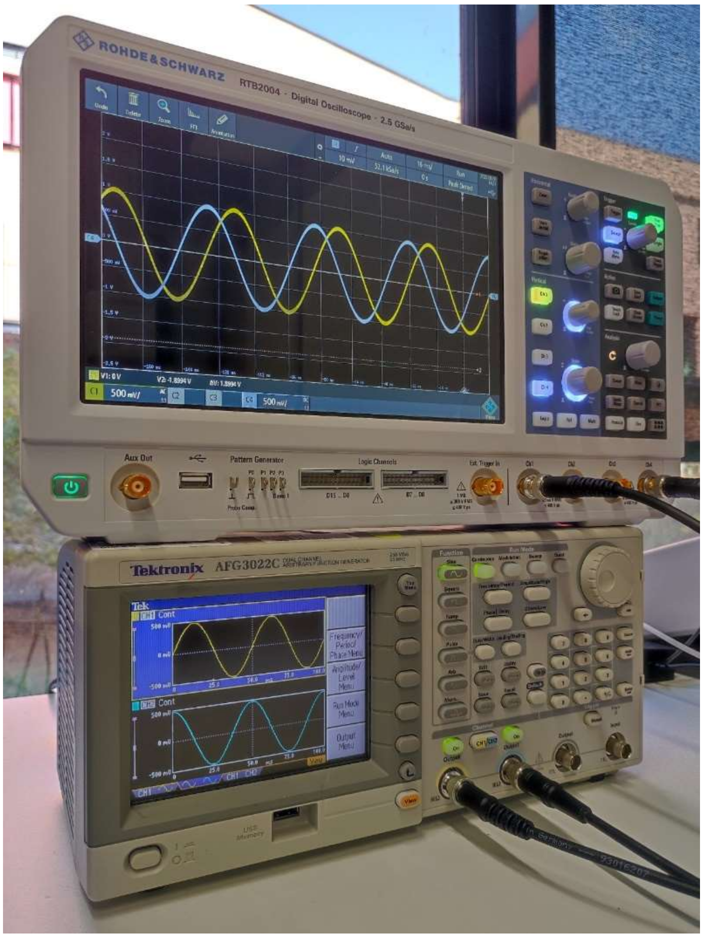

FIG. 4.16. The output waves of two channels in the oscilloscope. The two modulation signals are generated by the Tektronix AFG3022C generator (downwards) with 90° phase shift. The phase shift is verified in the Rohde & Schwarz RTB2004 oscilloscope (upwards).

At this stage, the experiment plafond was finally complete, as shown in **Fig 4.17**. The two coils were connected to the external signal generator passing through a modulation amplifier. The excitation piezoelectric chip was connected to the Polytech measurement machine and passing through another single-channel high-impedance-adapted amplifier. The laser measurement point was also marked in **Fig 4.17(a)**.

With the two fabricated samples whose first eigenfrequency is characterized to be 115Hz, we redid a GA-based parameter tuning. With the known first eigenfrequency 115Hz and the known coil mass of 2.5g, the effective stiffness and effective mass were estimated via FE calculations (mentioned in 4.II.2): $\kappa_0 = 1600\text{N/m}$ and $m = 3\text{g}$. The following parameters concerning the host beam were fixed: $h = 3$ mm and $d =$

20 mm. The remaining parameters were tuned as follows: $\Omega/2\pi = 20$ Hz, $l = 70$ mm and k_m was expected to be $208\,\mathrm{N/m}$. According to the theoretical model, the nonreciprocity strength is largely related to modulation strength k_m which related to the effective current in the coils. At this stage, the relationship between k_m and the effective current is unknown in the actual experiment because of the fabrication errors, but it was foreseen that higher effective current would be necessary than that expected in the FE calculations (mentioned in Part II.2). So, we just chose the effective current as high as possible.

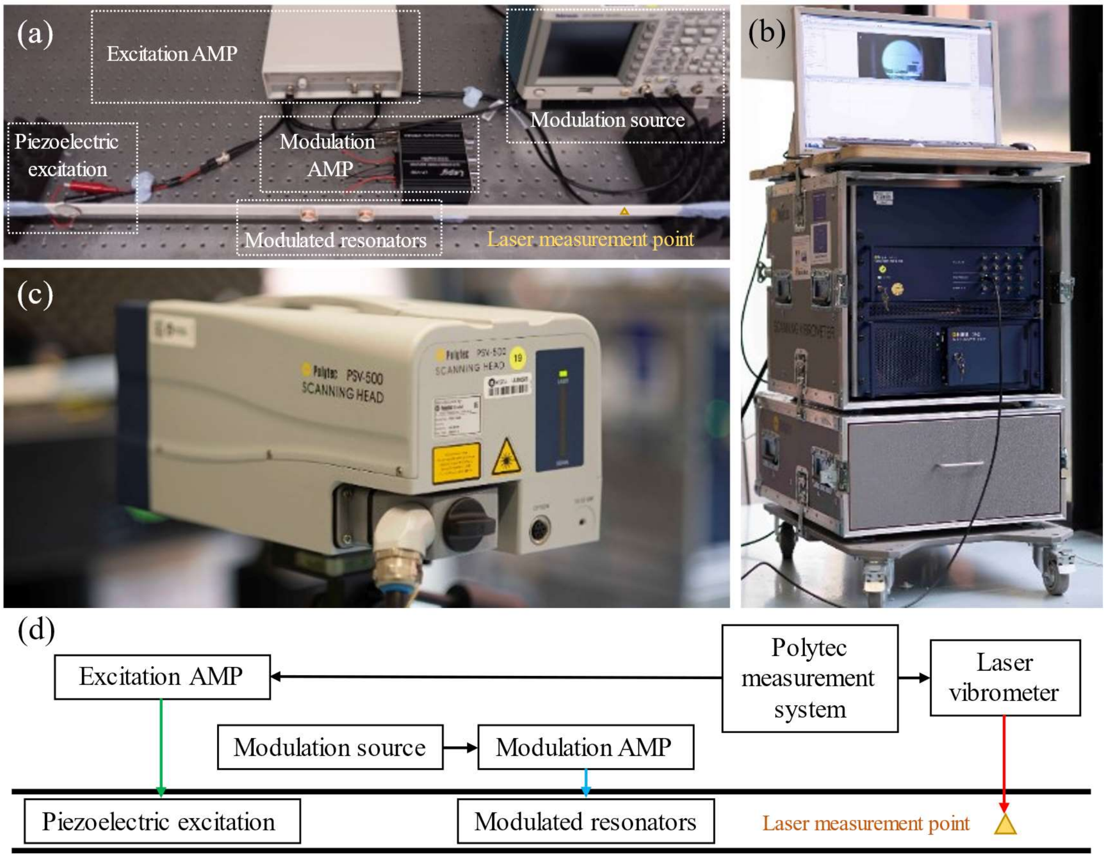

FIG. 4.17. (a) Experimental platform for flexural wave transmission. (b) The Polytec measurement system. (c) The PSV-500 laser vibrometer. (d) The schema of the experimental platform. AMP: amplifier.

The level of effective current we could reach was determined not only by the performance limitation of our amplifier and signal generator, but also by the level of the heating effect that could be sustained. According to the known power equation $P = I^2\mathrm{R}$, when we double the current, we get four times the heat. We have thought of using fan as cooling means during the measurement, but it was denied since huge noise was found to be introduced into the system by the air flow. Therefore, to get the highest possible effective current, we let the coil power-on duration as short as possible, so that we could reduce the temperature rising during the measurement. The coil power-on duration is directed related to measurement time, which is determined by the FFT resolution of the laser vibrometer. Because FFT resolution is limited by sampling quantity, low resolution means a small number of samples then a short sampling (measurement) time. When the FFT resolution is 1Hz which is the least acceptable level, the sampling (measurement) time is 1s. With 1s measurement time, the highest effective current we could apply was 0.46A, which leads to about 30°C temperature rising on the surface of coil after 1s powering on (measured via an infrared thermometer). Due to the poor heat transfer efficiency of PLA material, the temperature rising of the cantilever structure was expected to be much lesser than 30°C. In such situation, the stiffness shift of the structure would be acceptable. Before every next measurement, we had to wait till the surface temperature of the coil is lowered to room temperature. In this step, the fan was utilized to accelerate the heat dissipation, while the cost was that we had to redo the focusing of laser vibrometer before every measurement.

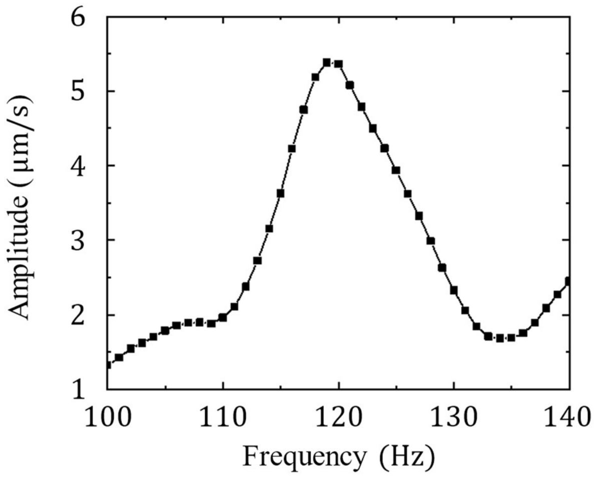

FIG. 4.18. Measurement result of bare beam frequential response without MSER from 100Hz to 140Hz.

With the above measurement strategy, we were able to perform the measurement on one single point at one single frequency for one time. To avoid the influence of torsion mode of host beam (**Fig 4.8**), we let the measurement point on the center line of the host beam. Before bonding the resonators on the host beam, we performed a measurement of transmission on the bare beam at the desired frequencies. This series of data would be used for the normalization of experiment results, displayed in **Fig 4.18**. The unevenness in the curve of frequential response of the bare beam was thought to be caused by the reflection (before 120Hz) and the uneven frequency response function (FRF) of the excitation piezoelectric chip at low frequencies.

In the initial attempt of measurement, we let the external signal generator output-on all the time and controlled the power-up of coils by turning on and turning off the modulation amplifier. However, the figures we got were very unstable and abnormally huge, which had order-of-magnitude difference with the results on bare beam. The reason was found to be the sonic boom of modulation amplifier when turned on. As we would like to shorten the power-on duration of coils, we did not wait for the stable states of amplifier after it was turned on to begin the measurement. Fortunately, it seems that there is no sonic boom for the signal generator. So, we decided to let the modulation amplifier power-on all the time, then controlled the power-up of coils by activating and disactivating off the output modulation amplifier. Further, we also let the excitation piezoelectric chip power-on all the time. With this strategy, the results we got were well reasonable.

Concerning switching the wave propagation direction, we switched the initial phase of time modulation on the two coils instead of switching the positions of excitation and measurement, considering that the two resonators were highly similar. Under such a setting, the positive direction means the initial phase of current of the coil close to the piezoelectric excitation is 90°, while that close to the laser measurement point is 0°. The negative direction means the former is $-90°$, while the latter is 0°.

Finally, we selected the typical frequency range, from 121Hz to 130Hz (1Hz step size), then performed five measurements for each propagation direction at each frequency.

IV. Result discussion and outlook

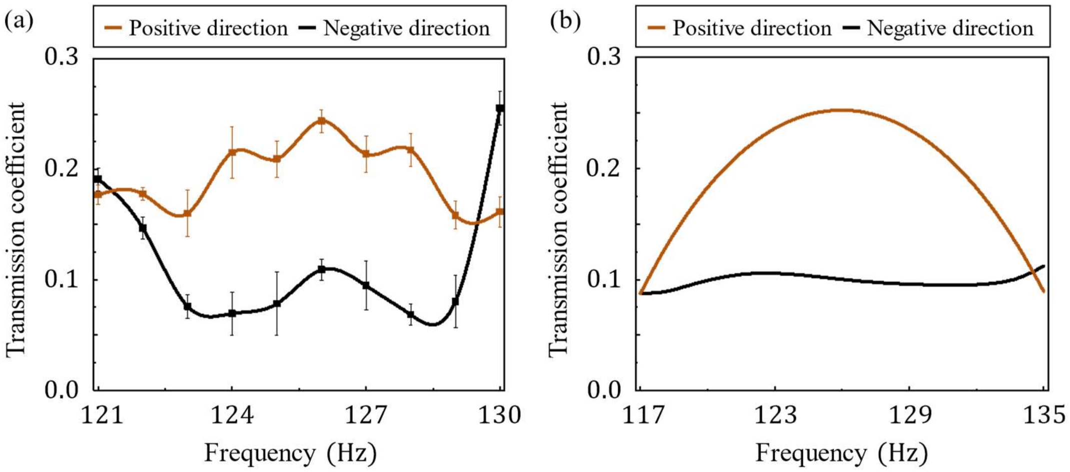

FIG. 4.19. (a) Results of the transmission measurements from 121Hz to 130Hz with error bars, normalized by the results of the bare beam (without resonators). (b) Analytical transmission coefficient A_0^+ in the frequency domain.

Fig. 4.19(a) shows the postprocessed results of the measured transmission with error bars, which is normalized by the frequential response of the bare beam. The curve is obtained by an interpolation function over the points of measurement. **Fig. 4.19(b)** shows the corresponding theoretical results with the re-estimated parameters: $\kappa_0 = 1500\mathrm{N/m}$, $m = 3\mathrm{g}$, $\Omega/2\pi = 20\ \mathrm{Hz}$, $l = 70\ \mathrm{mm}$ and $k_m = 200\ \mathrm{N/m}$, where the equivalent first eigenfrequency of the resonator was adjusted to 113 Hz from 115 Hz due to heating effect. The actual effective current 0.46A which realized $200\ \mathrm{N/m}$ of k_m is approximately 50% higher than that from FE simulation estimation (Fig 3.9, 0.3A for $200\ \mathrm{N/m}$ of k_m). We can clearly evidence the nonreciprocal wave transmission for flexural waves with an acceptable agreement observed between theory and experiment, where the center frequencies and the amplitudes of both are consistent. The error bars indicate the stability and reproducibility of the measured nonreciprocal transmission in our system.

The bandwidth of the measurement result is however relatively different from that of the theory because of the approximations made in modeling the resonators, including neglecting the dimensions of resonators and the material damping. The other errors are leaded by the remaining boundary reflections around 120Hz and the second eigenfrequency of the resonators. We also avoided the integer multiple frequencies of $\Omega/2\pi$ (20Hz, 40Hz, 60Hz, etc.) because of huge noise at these frequencies. The noise was caused by the fabrication errors of the resonators, such as the magnet and the coil being not coaxial and concentric. In this case, the AC itself could become an excitation source at the AC frequency Ω, while the time modulation of the same frequency Ω on structure stiffness remains. Then, high noise at the harmonics of the AC frequency (20Hz, 40Hz, 60Hz, etc.) would be generated.

To figure out the mechanism of nonreciprocity in our structure, we have analyzed the mechanical energy of the transmitted and reflected waves, as well as in the resonators using numerical approaches for the case with time modulated effective stiffness. The mechanical energy took advantage of the results of FE simulation which adopted the re-estimated parameters. Frequency conversion is depicted with the appearance of high order waves at frequencies $126\text{ Hz} + n\Omega$ where $n = \pm 2,\ \pm 1$.

The mechanical energy in the flexural wave on the plate can be calculated[13],

$$E_b = \omega EIk^3|\bar{X}|^2 \tag{4.37}$$

where $|\bar{X}|$ is the amplitude of the flexural wave. The mechanical energy in the resonator can also be calculated using the formula,

$$E_k = \frac{1}{2}m(\omega|w^m|)^2 \tag{4.38}$$

$$E_p = \int_0^{T_M} \frac{1}{2}[k_0 + k_m\cos(\Omega t)]|w^m|^2 dt \tag{4.39}$$

where E_k is the kinetic energy of the mass, E_p is the potential energy of the spring, and $T_M = 2\pi/\Omega$ is the cycle of the temporal modulation. **Fig. 4.20** exhibits the stacked area charts of the mechanical energy of the system in both propagation directions for incident harmonic waves with frequencies between 117 and 135 Hz. The chart represents the calculated energy for the transmission (green) and reflection (pink) waves in the plate, the energy stored in the resonators (yellow), and the sum of the energies carried by the high order waves at frequencies $\omega + n\Omega$ where $n = \pm 2, \pm 1$ for the transmitted (orange) and reflected waves (blue), as well as in the resonators (purple), all normalized by incident wave energy. Considerable frequency conversions appear in this time-modulated system, which is the principal incentive for the nonreciprocity in our structure. We observe that the low transmitted energy (green) of the fundamental mode (0th order) in the negative direction is attributed to frequency conversion in the transmitted (orange) and reflected waves (blue). Another observation is that the total energy in our structure surpasses the input energy from incident wave due to the input energy from active time modulation.

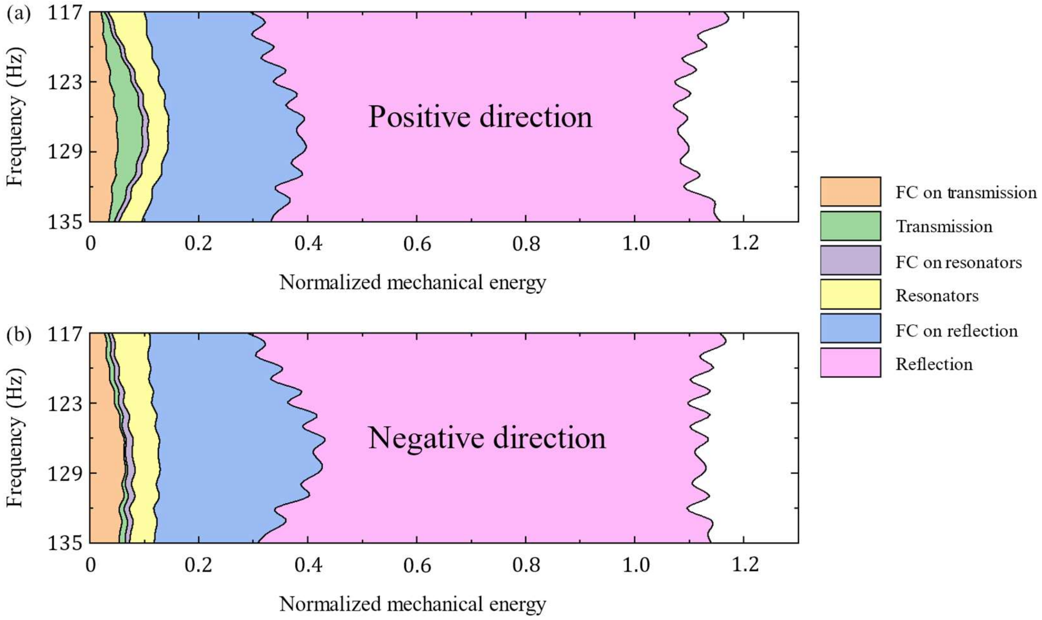

FIG. 4.20. Stacked area chart of global mechanical energy distribution for positive (a) and negative (b) directions calculated using FE simulation at various incident frequencies. FC: frequency conversion. Here we represent the mechanical energy for the transmitted (green) and reflected (pink) fundamental modes (0th order) in the plate, the energy stored in the resonators (yellow), and the sum of the energies carried by the high order waves at frequencies $\omega + n\Omega$ where $n = \pm 2; \pm 1$ for the transmitted (orange) and reflected waves (blue), as well as in the resonators (purple), all normalized by incident wave energy.

Concerning the nature of nonreciprocity, we propose some hypothesis explanations from personal point of view. When the resonators are coupled with the inter FP resonance, some energy can be trapped between the two resonators. As is known, if the confined energy generates a high-Q (high quality factor) resonance with a considerable radiation, it is designated as Fabry-Perot quasi bound states in the continuum (quasi-BIC)[14]. Surely, what we observe in the existing work[8,15] is definitely not quasi-BIC phenomenon, but for the ease of comprehension, we can consider the coupling between the resonators and the inter FP resonance as a near-BIC state. With the spatially biasing modulation, the coupling in the forward and backward propagation is biased. In consequence, in the specific propagation direction, the coupling state is closer to quasi-BIC than that in another direction, which finally leads to different wave propagations. It is worth being mentioned that the veritable directional BIC in bi-resonator structure is a potential path to obtain nonreciprocity. If the error in analytical model caused by approximations can be corrected in some way, it is feasible by fine tuning the modulation parameters and model geometry.

V. Discussion

To pursuit a further improvement on the performance of nonreciprocity, we need to apply the stronger AC on the coils than that we have done. We can deploy heatsink on the coil to cool it down; the material whose properties are not sensitive to temperature can replace PLA as the structure material; and the temperature excursion can be estimated and pre-considered in the structure designing; even optimizing the fabrication precision of the coils can lead to a giant improvement.

In conclusion, we have introduced in this work a compact time-modulated mechanical bi-resonators system to achieve nonreciprocal flexural wave transmission at low frequency. The resonators were designed with a vibrating cantilever with magnetically coupled coils and magnets. The temporal modulation of the effective stiffness of each resonator was realized by an AC applied to the coil which couples to the fixed magnets via the varying magnetic field. The dimension of this device is less than $1/3$ wavelength. A physical realization of such a system based on coil-cantilever-magnet resonators has been experimentally conducted. The obtained measurements have evidenced high nonreciprocal flexural waves propagation with results that agree well with our simplified analytical predictions. Our concept provides a promising perspective on the design of compact nonreciprocal metamaterials that can integrate flexural waveguiding systems for smart wave control in phononic communication devices.

References

[1] Y. Wang, B. Yousefzadeh, H. Chen, H. Nassar, G. Huang, and C. Daraio, Phys. Rev. Lett. **121**, 194301 (2018).

[2] Y. Chen, X. Li, H. Nassar, A.N. Norris, C. Daraio, and G. Huang, Phys. Rev. Applied **11**, 064052 (2019).

[3] B.M. Goldsberry, S.P. Wallen, and M.R. Haberman, The Journal of the Acoustical Society of America **146**, 782 (2019).

[4] J. Marconi, E. Riva, M. Di Ronco, G. Cazzulani, F. Braghin, and M. Ruzzene, Phys. Rev. Applied **13**, 031001 (2020).

[5] M.A. Attarzadeh, J. Callanan, and M. Nouh, Phys. Rev. Applied **13**, 021001 (2020).

[6] S. Wan, L. Cao, Y. Zhu, M. Oudich, and B. Assouar, Phys. Rev. Applied **16**, 064061 (2021).

[7] C. Shen, J. Li, Z. Jia, Y. Xie, and S.A. Cummer, Phys. Rev. B **99**, 134306 (2019).

[8] C. Shen, X. Zhu, J. Li, and S.A. Cummer, Phys. Rev. B **100**, 054302 (2019).

[9] X. Zhu, J. Li, C. Shen, X. Peng, A. Song, L. Li, and S.A. Cummer, Appl. Phys. Lett. **116**, 034101 (2020).

[10] G. Trainiti and M. Ruzzene, New J. Phys. **18**, 083047 (2016).

[11] L. Cao, Z. Yang, Y. Xu, Z. Chen, Y. Zhu, S.-W. Fan, K. Donda, B. Vincent, and B. Assouar, Mechanical Systems and Signal Processing **146**, 107035 (2021).

[12] Y. Shen and V. Giurgiutiu, Wave Motion **58**, 22 (2015).

[13] L. Cao, Y. Zhu, Y. Xu, S.-W. Fan, Z. Yang, and B. Assouar, Journal of the Mechanics and Physics of Solids **154**, 104502 (2021).

[14] C.W. Hsu, B. Zhen, A.D. Stone, J.D. Joannopoulos, and M. Soljačić, Nat Rev Mater **1**, 1 (2016).

[15] S. Wan, L. Cao, Y. Zeng, T. Guo, M. Oudich, and B. Assouar, Appl. Phys. Lett. **120**, 231701 (2022).

Chapter 5

Nonreciprocal acoustic meta-lens

Contents

I. Introduction

In pursuit for the practicality of nonreciprocal devices, time-modulated bi-resonator structures have gained high interest in recent years[1–3]. Despite the advantage that the time-modulated bi-resonator system overcomes the large-dimension drawback of space-time periodic structures, some critical limitations still remain. First, all of the contemporary time-modulated bi-resonator structures are designed to work only in one dimension (1D), and have limited potential to be used for two or three dimensional wave manipulations. Second, their operational frequency band are narrow and locked around the resonance frequency of the resonators. Third, as we have seen in the previous chapters, precise and complicated techniques are needed in order to modulate the mechanical properties for the realization of nonreciprocity, such as using large shaker and electromagnetic coupling. Last, a more critical drawback is that time modulation generates multiple harmonic waves, turning a monochromatic excitation into a multichromatic wave where, in many cases, these harmonics are seen as undesirable. This frequency conversion is a common constraint in nonreciprocal devices using time modulation techniques. To overcome all these limitations, we have considered another approach for breaking reciprocity which is based on the introduction of airflow to interact with acoustic waves. We have also pushed our project toward the design of a non-reciprocal device that can be adaptable to 2D or 3D wave manipulation to achieve multiple acoustic functionalities.

It is well know that fluid flow is one of the approaches to realize nonreciprocity for sound[4]. As we have described in chapter 1, such device involving air flow that breaks reciprocity in acoustics[5] is first introduced in 2014 by Fleury et al. who constructed an acoustic circulator [6]. This device splits a single resonant mode into two which correlates the clockwise and the counterclockwise directions of propagation, and by exploiting the directional interference between the two propagation directions, a unidirectional sound isolator is then achieved. This design was afterwards expanded to a periodic structure[7], forming an acoustic Chern insulator to demonstrate a nonreciprocal chiral edge states with robust topological protection. From another perspective of wave manipulation, Zhu et al.[8] used multiple two-level acoustic circulator which forms a Janus nonreciprocal acoustic metasurface, realizing multi-functional wave manipulations. Then based on the original structure, Wiederhold et al.[9] simplified the design and demonstrated a nonreciprocal leaky-wave radiation. Inspired by this work, we designed a structure with moving fluid with a simple design for unidirectional wave manipulation. In our structure, we manipulate the phase evolutions of the forward and backward sound waves. The structure design is based on a cylindrical waveguide in which we introduce steady airs flow for momentum biasing, leading to two different phase velocities of sound waves in opposite propagation directions depending on the flow direction. Consequently, the wave travelling time in the two propagation directions differs which results in nonreciprocal phase evolutions. Then we divide the cylindric waveguide into multiple channels in a coaxial manner and dispose different air flow (with different velocity) in each channel, resulting in independent nonreciprocal phase evolutions at each channel. By tuning the air flow in each channel, we can realize multiple nonreciprocal functions. One may consider that our idea shares some similarities with Wiederhold et al.[9], however in our design, we emphasize on the feasibility of the model. The way in which we acquire different air flows is to use blade rotor (similar to a fan), as the fan blades are mostly used to produce velocity gradient. Further, we explore multiple functionalities that can be achieved by our structure for unidirectional acoustic wave steering.

II. Breaking reciprocity with air flow

Let us assume a time-invariant air flow velocity field vector $\vec{v}$ with small Mach number $|\vec{v}|/c$ ($|\vec{v}|/c < 0.3$), and consider it in the sound wave equation in the time harmonic regime with the $e^{j\omega t}$ convention[10],

$$\Delta p + \left(\frac{\omega}{c}\right)^2 \left(1 + \frac{j}{\omega}\vec{v} \cdot \nabla\right)^2 p = 0 \tag{5.1}$$

where p is the acoustic pressure field, ω is the angular frequency, and c is the speed of sound. Then, we consider two time-harmonic pressure fields, p_1 and p_2, which satisfy the above equation (5.1). Multiplying the wave equation for p_1 by p_2, and that for p_2 by p_1, then subtracting them leads to the following equation,

$$\nabla \cdot (p_2 \nabla p_1 - p_1 \nabla p_2) = -\left(\frac{\omega}{c}\right)^2 \left[p_2 \left(1 + \frac{j}{\omega}\vec{v} \cdot \nabla\right)^2 p_1 - p_1 \left(1 + \frac{j}{\omega}\vec{v} \cdot \nabla\right)^2 p_2\right] \tag{5.2}$$

In fact, the left side of Eq (5.2) equaling 0, $\nabla \cdot (p_2 \nabla p_1 - p_1 \nabla p_2) = 0$, is one of the mathematic expressions of the reciprocity in acoustics[11]. With no presence of air flow ($\vec{v} = 0$), all the terms in the right side of the Eq (5.2) are eliminated, which satisfies the reciprocity. However, in the case of $\vec{v} \neq 0$, the reciprocity relationship is not guaranteed.

In fluid dynamics, the time-reversal symmetry is key to reciprocity. The propagation of sound waves is consolidated by classical time-symmetric equations. When all the relevant field quantities properly evolve in time either in time-reversal condition ($e^{j\omega t}$) or in broken time-reversal condition ($e^{-j\omega}$), the propagation of sound waves should be reciprocal. However, the existence of time-invariant air flow velocity field vector $\vec{v}$ brings in a bias. When the time reversing operation is performed (from $e^{j\omega t}$ to $e^{-j\omega t}$), the odd vector $\vec{v}$ does not correspondingly flip its sign. It is something similar to the loss in a system (if considered) that, the loss cannot flip its sign then become a gain, although the time reversing operation is considered. Consequently, the time-reversal symmetry is broken by the presence of air flow.

Now, consider a hard-walled sound waveguide with transverse air flow v_x and only plane wave mode, so we can ignore the y and z component in Eq (5.1). Then we can solve the corresponding dispersion relation along the x axis,

$$k_x^2 = \left(\frac{\omega}{c} \mp \frac{v_x}{c} k_x\right)^2 \tag{5.3}$$

From the above equation, we can get the group velocity for the plane wave : $\partial\omega/\partial k_x = \pm c + v_x$. On the band structure, the biasing quantity v results in the global biasing of the slope of the dispersion curve, and a positive offset of wavenumber $v_x \omega / c^2$ is observed on both forward and backward propagations (**Fig. 5.1**).

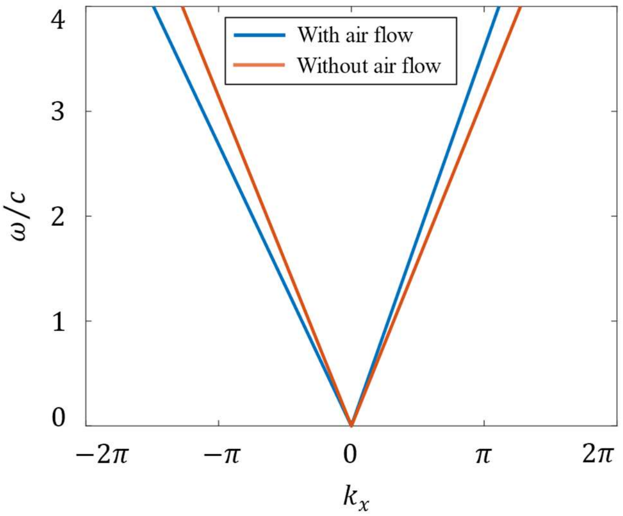

FIG. 5.1. The band structure for the first order mode of acoustic waves with and without air flow. $v_x = 50\text{m/s}$ in this calculation.

In the following part, we first explore the engineering of an acoustic isolator which enables high transmission in one direction while blocks the backscattered waves.

III. Nonreciprocal mode convertor

The phononic mode convertor turns a fundamental mode into a high-order mode. The Mach-Zehnder interferometer is a typical mode convertor in optics, which splits a monochromatic light beam in two and reunites the split beams after they travel through two individual paths[12,13]. On the base of Mach-Zehnder interferometer, we add the nonreciprocity features to let it work asymmetrically. The nonreciprocity feature here is concretized as nonreciprocal phase modulator. In our design, we split a cylindric air waveguide into two channels. As displayed in **Fig. 5.2**, blades with specific inclination are featured in part of these two channels, forming sloped WG (sloped waveguiding channels) with extended path for wave propagation. A rotor with similar structure as the slope WG is implanted as shown in **Fig. 5.2**, which is the spinning part also the source of air flows in our structure. This rotor generates two different air flows (with different velocities v_1 and v_2) in two channels. Here, the sloped WGs play the role of reciprocal phase modulators. In our nonreciprocal mode convertor, the phase modulator is indispensable. Because under small Mach number, the only phase difference brought by the air flow in the two propagation directions is the sign ($\Delta\phi_{\text{forward}} + \Delta\phi_{\text{backward}} \approx 0$). In order to directionally change the propagation mode, this relationship must be broken. So, an offset of phase shift should be introduced, which is the propre role of reciprocal phase modulators.

The channels with air flow work, in fact, as nonreciprocal phase modulators. Owing to the difference of the phase velocity in two directions, the wave phase advances more in one direction than in another; and owing to the difference of the phase velocity in the two channels, the wave phase advances more in one channel than in another. By adjusting the blade inclination and the spinning speed of the rotor, we intend to achieve a phase difference of $\pi + 2n\pi$ $(n = \cdots, -1, 0, +1, \dots)$ between two channels in one direction, saying the phases of waves in two channels are inversed; we intend to achieve a phase different of $2n\pi$ $(n = \cdots, -1, 0, +1, \dots)$ in the opposite direction, in which case the phases of waves in two channels are the same. When two split waves reunite with opposite phase, they are combined into an antisymmetric mode. Due to the heat dissipation effect at the combination interface, a small amount of energy is lost in this process.

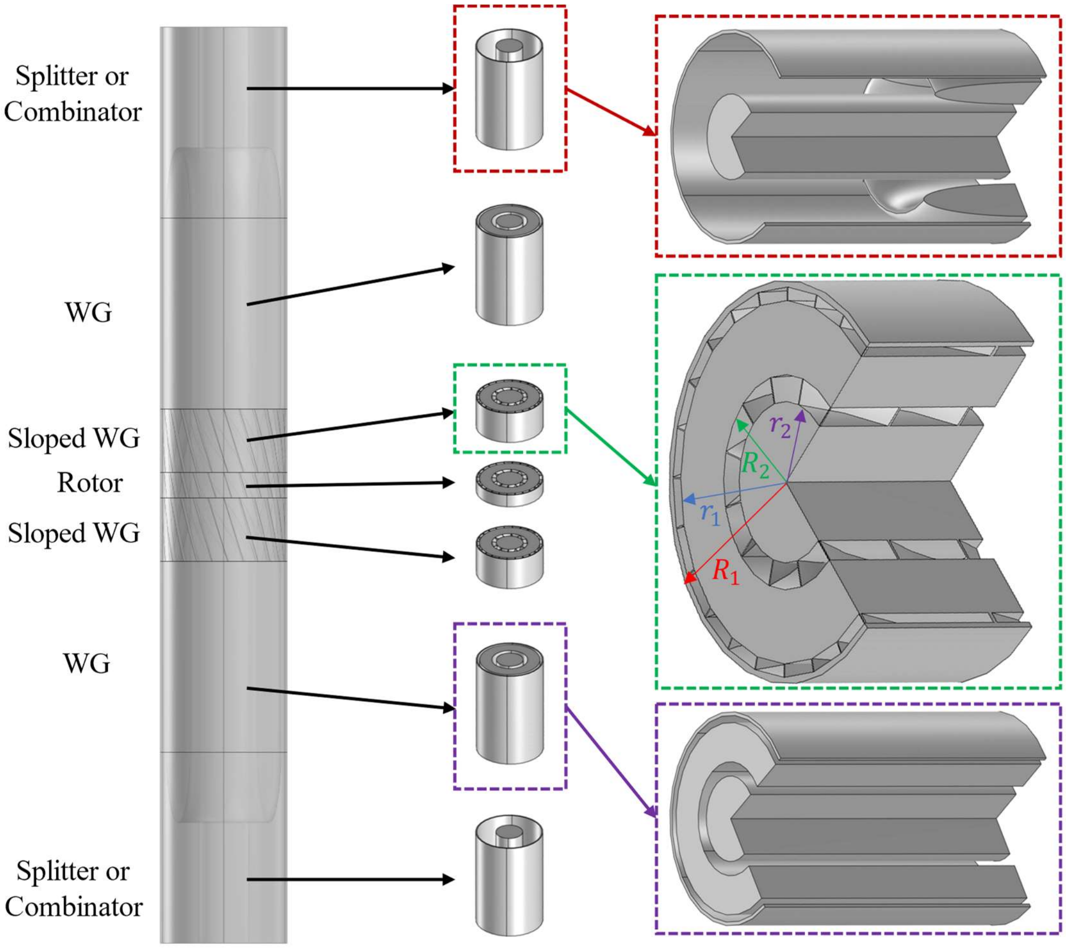

FIG. 5.2. The geometric design of our nonreciprocal mode convertor. In the left, a semi-transparent view is displayed; in the middle, all partitions are displayed separately; in the right, the inner profiles of the bi-channel waveguide, the splitter or combinator and the sloped bi-channel waveguide are displayed. WG stands for waveguide.

In **Fig. 5.2**, an entity of our design is displayed, which is composed of two partitions of direct bi-channel waveguides, two partitions of sloped bi-channel waveguides, two combinators or splitters, and a rotor with bi-layer blades. In order to maintain the uniformity of the air flow velocity in the annular channel, the channel width (the difference between the inner diameter r_i and the outer diameter R_i) are designed to be relatively small ($(R_i - r_i)/R_i \ll 1$), so that when the air flow is being generated by the spinning rotor, the linear velocity at the polar position R_i is very close to that at the polar position r_i. Now, the entrance interface to the bi-channel phase modulator is shaped as two slim coaxial rings, where the inlet port of the global system is still a complete circle. The semi-oval sound hard walls (the splitters or combiner in **Fig. 5.2**) are implanted at the interface which smoothens the shape of the wave transition. When working as wave splitter, the semi-oval sound hard walls can reduce the potential reflection at the entrance interface to the bi-channel phase modulator; when working as wave combinator, they can improve the output wavefront.

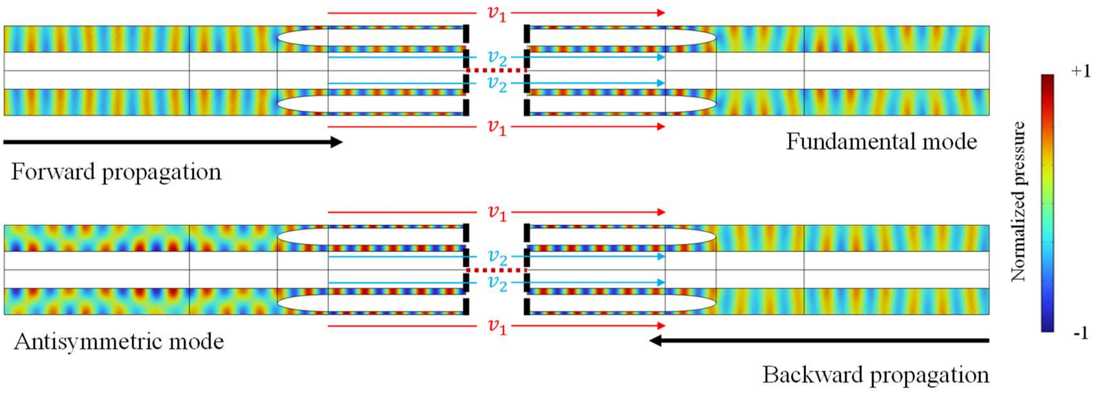

FIG. 5.3. Numerical result of a nonreciprocal mode conversion at 3700Hz. The slices of pressure field along the air cylinder are displayed, while the partitions of rotors and sloped bi-channel waveguides are omitted. The pressure field is normalized with local extreme value. v_1 and v_2 are the air flow velocities in the outer channel and in the inner channel. The phase difference between two channels in the forward direction is 2π, and that in the backward direction is $-\pi$.

In **Fig. 5.3**, we show a numerical example of nonreciprocal mode conversion at 3700Hz, which is calculated via FEM using the commercial software COMSOL Multiphysics 6.0. In this model, the average radiuses of the outer and inner channels are 14cm and 7cm. Due to the complexity of the geometry, the partitions of sloped waveguide and rotor are not displayed in the figure. The inclinations of the outer and inner sloped channels are 17° and 30°. The acquired air flow velocities in the outer channel and inner channel are, respectively, 28.6m/s and 7.6m/s, which is easily achieved by rotor with corresponding dimension spinning at 3000r/min. These values are calculated via solving a binary system of equations which establishes the relationship between the slop degrees, the air flow velocities, and the directional phase shift. An antisymmetric mode transmission can be observed at the output port in the backward propagation direction, while the wavefront in the forward direction is a little affected.

IV. Multifunctional nonreciprocal acoustic meta-lens

Since the nonreciprocal phase modulator can form an sound isolator as we implant two of it in Mach-Zehnder interferometer, it is then possible to implant multiple nonreciprocal phase modulators in a multi-channel structure to realize nonreciprocal metasurface function, like what was introduced by Zhu et al.[8]. knowing that sound wave is a scalar wave, if we can manipulate the wave phase on a surface, we can produce various wavefronts as desired, which is featured as the basic concept of acoustic metasurface. Integrating nonreciprocal phase modulator with metasurface is a fresh idea in the acoustic area. Zhu et al.[8] conducted they study in a 2D plane. Differently, owing to the ring-shaped geometric structure of our design, all the nonreciprocal functions we realize are rotationally symmetric in 3D space. So, we consider it as an acoustic meta-lens.

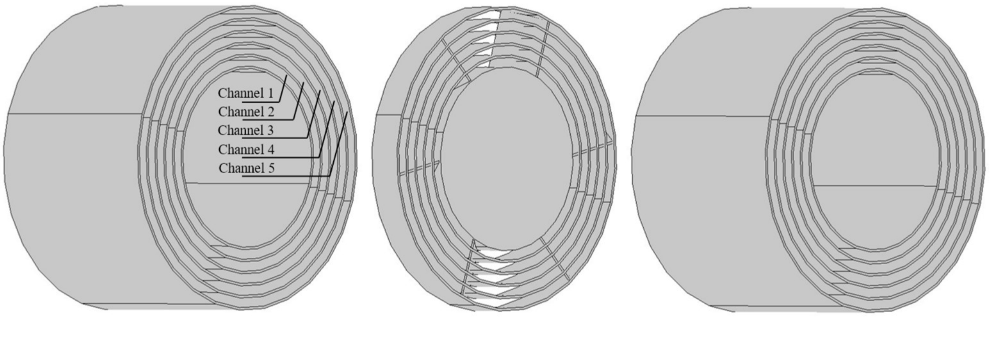

Multi-channel waveguide Rotor Multi-channel waveguide

FIG. 5.4. Conceptional schematic design of the nonreciprocal acoustic meta-lens.

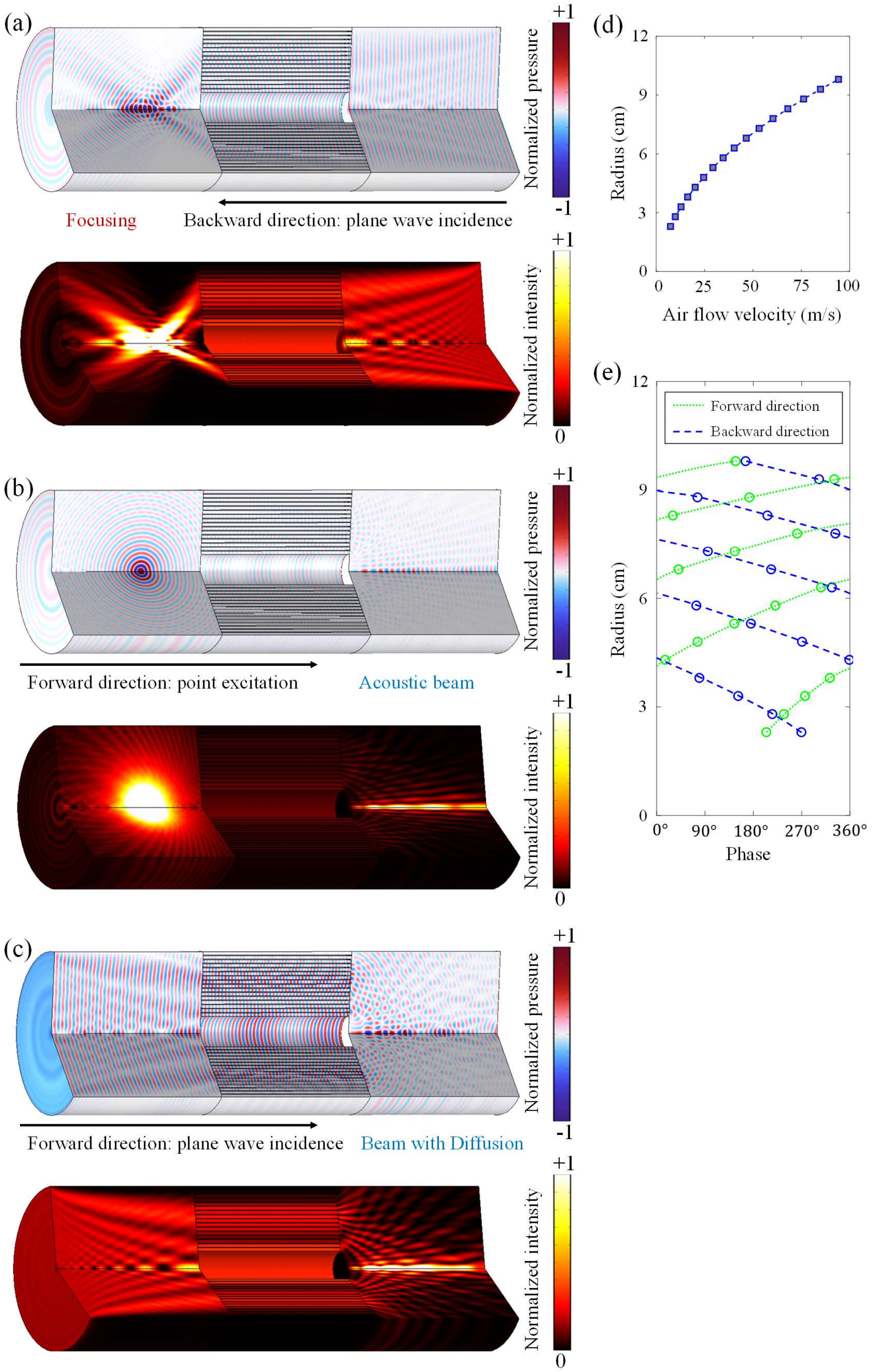
(a)
Normalized pressure
+1
-1
Focusing
Backward direction: plane wave incidence
Normalized intensity
+1
0
(b)
Normalized pressure
+1
-1
Forward direction: point excitation
Acoustic beam
Normalized intensity
+1
0
(c)
Normalized pressure
+1
-1
Forward direction: plane wave incidence
Beam with Diffusion
Normalized intensity
+1
0
(d)
Radius (cm)
0
3
6
9
12
0
25
50
75
100
Air flow velocity (m/s)
(e)
Forward direction
Backward direction
Radius (cm)
0
3
6
9
12
0°
90°
180°
270°
360°
Phase

FIG. 5.5. Nonreciprocal acoustic wavefront manipulation for focusing at 34000Hz. (a) In the backward direction, an incident plane wave is focused on transmission (8cm away from the structure). (b) At the destinated focusing position, if we put a point source for a time-reversal forward propagation, then a beam wavefront is generated in opposite direction. Both pressure field and intensity field are shown in (a) and (b). (c) In the forward direction, a plane wave incidence results in a beam wavefront with some diffusion, instead of being focused. (d) The air flow velocity profile as the function of channel's position (average radius of channels). (e) The phase shift profiles as function of the channel position in both propagation directions (green curves for the forward direction and blue curves for the backward direction).

To perform an acoustic meta-lens, we split the annular waveguide into multiple ring-shaped channels, and encode each channel with different phase shift via air flow. A conceptional design is shown in **Fig. 5.4**, composed of simple multi-channel waveguides and a rotor. The rotor can have blades with different inclinations in different channels for the sake of the gradient air flow velocity. There are no more sloped waveguides because the reciprocal phase modulator is not necessary in the usage here.

We show two functions as example of the nonreciprocal meta-lens in **Fig. 5.5** and **Fig. 5.6** at 34000Hz, numerically calculated via COMSOL Multiphysics 6.0. For the simplification purpose, the rotors were excluded of the geometry, and instead, the air flow velocities were configured directly in the channels. We used 16 channels for a high-resolution wavefront manipulation.

In **Fig. 5.5**, an example of nonreciprocal wavefront manipulation for focusing is displayed. We configured the air flow in the structure according to the velocity profile shown in **Fig. 5.5(d)**, which leads to a directional phase shift shown in **Fig. 5.5€**. We first performed plane wave incidence in the backward direction, and got a focusing on the left side of the structure at the designed position (a point on the axis 8cm away to the structure) (**Fig. 5.5(a)**). Then we performed a time-reversal propagation by positioning a point source at the focusing position. As a result, a sound beam occurs on the right side of the structure instead of plane wave radiation (**Fig. 5.5(b)**), clearly displayed in the intensity field. Furthermore, we performed plane wave incidence in the forward direction (**Fig. 5.5(c)**), the counter case to the **Fig. 5.5(a)**. As expected, it was not focused but rather forms a beam with diffusion, which proves the asymmetry of our structure. A weak focusing also appeared at the far end, due to the absence of channels on the cylinder axis (position $r = 0$).

Another example of nonreciprocal wavefront manipulation for plane wave generation is displayed in **Fig. 5.6**. With the air flow configured as descried in **Fig. 5.6(d)**, we managed to get a plane wavefront with a point source on the left side of structure in a time-reversal-asymmetric way. In the forward direction, we managed to perform a wave plane generation with a point source on the left side (**Fig. 5.6(a)**), while in the backward direction, in case of plane wave incidence, diffusion occurs on the left side instead of focusing (**Fig. 5.6(b)**). I the n case of point source, an acoustic beam was produced on the other side (**Fig. 5.6(c)**).

When tuning the acoustic meta-lens, one must avoid configuring large air flow velocity in the structure, because complex situations could occur when the Mach number is relatively high (greater than 0.3).

V. Conclusion

In this chapter, we have introduced the design concept of a nonreciprocal acoustic structure using air flow, including the nonreciprocal mode convertor and the nonreciprocal meta-lens. With the meta-lens, nonreciprocal wavefront manipulations from two opposite incidences are achieved. Our finding exploits a simple way of using air flow to produce nonreciprocal systems using controlled rotating elements for phase modulation via variable air-flow velocities.

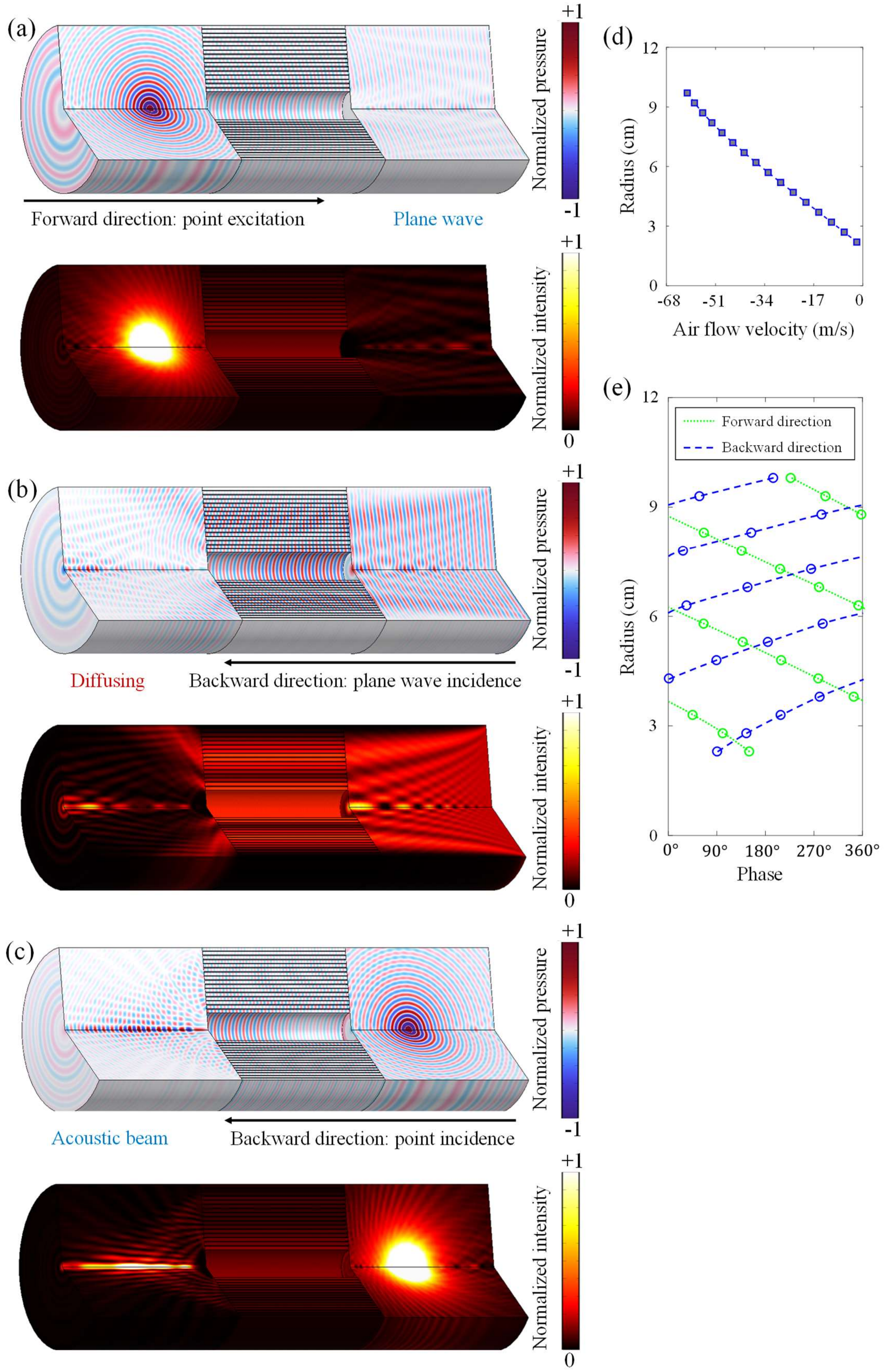
(a)
Forward direction: point excitation
Plane wave
Normalized pressure
+1
-1
Normalized intensity
+1
0
(b)
Diffusing
Backward direction: plane wave incidence
Normalized pressure
+1
-1
Normalized intensity
+1
0
(c)
Acoustic beam
Backward direction: point incidence
Normalized pressure
+1
-1
Normalized intensity
+1
0
(d)
Radius (cm)
12
9
6
3
0
-68
-51
-34
-17
0
Air flow velocity (m/s)
(e)
Forward direction
Backward direction
Radius (cm)
12
9
6
3
0
0°
90°
180°
270°
360°
Phase

FIG. 5.6. Nonreciprocal acoustic wavefront manipulation for plane wave generation at 34000Hz. (a) In the forward direction, a plane wavefront is generated with a point incidence on the left destinated position (8cm away from the structure). (b) In the backward direction, we incident a plane wave for a time-reversal propagation, then get a diffused wavefront. (c) In the backward direction, we place a point source on the right destinated position (8cm away from the structure), then get an acoustic beam on the left side of the structure. Both pressure field and intensity field are shown. (d) The air flow velocity profile as the function of channel position (average radius of channels). (e) The phase shift profiles as the function of channel position in both propagation directions (green curves for the forward direction and blue curves for the backward direction).

References

[1] X. Zhu, J. Li, C. Shen, X. Peng, A. Song, L. Li, and S.A. Cummer, Appl. Phys. Lett. **116**, 034101 (2020).

[2] C. Shen, J. Li, Z. Jia, Y. Xie, and S.A. Cummer, Phys. Rev. B **99**, 134306 (2019).

[3] C. Shen, X. Zhu, J. Li, and S.A. Cummer, Phys. Rev. B **100**, 054302 (2019).

[4] O.A. Godin, Wave Motion **25**, 143 (1997).

[5] R. Fleury, D.L. Sounas, C.F. Sieck, M.R. Haberman, and A. Alù, Science **343**, 516 (2014).

[6] P. Zeeman, Lond. Edinb. Dublin Philos. Mag. J. Sci. **43**, 226 (1897).

[7] Y. Ding, Y. Peng, Y. Zhu, X. Fan, J. Yang, B. Liang, X. Zhu, X. Wan, and J. Cheng, Phys. Rev. Lett. **122**, 014302 (2019).

[8] Y. Zhu, L. Cao, A. Merkel, S.-W. Fan, B. Vincent, and B. Assouar, Nat. Commun. **12**, 7089 (2021).

[9] C.P. Wiederhold, D.L. Sounas, and A. Alù, J. Acoust. Soc. Am. **146**, 802 (2019).

[10] *Theoretical Acoustics* (1987).

[11] H. Nassar, B. Yousefzadeh, R. Fleury, M. Ruzzene, A. Alù, C. Daraio, A.N. Norris, G. Huang, and M.R. Haberman, Nat. Rev. Mater. **5**, 667 (2020).

[12] P. Hariharan, *Optical Interferometry, 2e* (Academic Press, 2003).

[13] S.V. Gaponenko, *Introduction to Nanophotonics* (Cambridge University Press, Cambridge, 2010).

General conclusion and perspective

In this doctoral project, we have theoretically and numerically proposed two kinds of nonreciprocal acoustic metamaterials using time-varying media. One is based on the bi-resonator time-modulated structure taking advantage of asymmetric frequency conversion, and the other is based on the moving media forming asymmetric phase velocity of wave propagation. An experimental demonstration of nonreciprocal cascaded time-modulated spring-mass resonator system using the coupling between magnets and the electromagnetic field of coils with alternating currents was carried out.

Most relevant and up-to-date literatures on nonreciprocal acoustic device have been sufficiently reviewed in Chapter 1, state of the art, including nonlinear media, circulating air, spatiotemporally modulated media, and moving media. More specifically, the concepts and principles of reciprocity and nonreciprocity are introduced at first, and then the various methods for the realization of nonreciprocity in acoustics and elastodynamics are elucidated with representative references.

The numerical and analytical approaches utilized to solve the nonreciprocal acoustic system using time-varying media is discussed in Chapter 2. We briefly introduce the finite element and the finite-difference time-domain methods, then explain in detailed expressions the temporal coupled-mode theory (TCMT), the transfer matrix method (TMM) and the quadratic eigenvalue problem (QEP) solving with Fourier decomposition. Simple scenarios of application are provided for these analytical approaches.

We have introduced two bi-resonator systems with time-modulated properties in Chapter 3 and 4, in which one is based on coupled Fabry-Perot (FP) slabs for sound waves, and the other is based on coupled spring-mass resonator (SMR) for elastic flexural waves. In Chapter 3, we have demonstrated nonreciprocal acoustic transmission and unidirectional frequency conversion in cascaded FP slab resonators based on temporally modulating their effective densities, with phase difference in the time modulations between the FP slabs. TMM based on Fourier decomposition has been developed for efficient characterization of the wave transmission in the system, while numerical simulations based on FEM have been conducted to assess the theoretical findings. Optimizations over the system's parameters were carried out to achieve broadband nonreciprocity and frequency conversion. An acoustic nonreciprocity behavior has been observed with a monochromatic incident wave, with almost 97.9% transmission in the positive direction while only 4.3% is transmitted in the negative direction. Furthermore, unidirectional frequency conversion has been exploited. Over half of the transmitted acoustic energy has been converted into one single mode with higher static density ratio. The proposed design of nonreciprocal acoustic system displays promising functionalities, with a simple compact configuration to achieve unidirectional wave propagation and frequency conversion. Though the present system is purely theoretical and far from representing a realistic device for application, it is possible to imagine a solid system where we only consider longitudinal waves which are described with the same Helmholtz equation, thus behaves the same as acoustic waves in fluid. In this case, our approach could also be conducted by considering the time modulation of the effective stiffness instead of density of the materials using piezoelectric elements

In Chapter 4, we have introduced a subwavelength time-modulated mechanical cascaded SMR system to achieve nonreciprocal flexural wave transmission at low frequency. The SMRs were designed with a vibrating cantilever with magnetically coupled coils and magnets. We first establish a semi-analytic TMM approach involving Fourier decomposition to perform the parameter tuning via genetic algorithm (GA). The temporal modulation of the effective stiffness of each resonator was physically realized by an alternating current (AC) applied to the coil which couples to the fixed magnets via the varying electromagnetic field. The dimension of this device is less than 1/3 wavelength. A physical realization of such a system based on coil-cantilever-magnet resonators has been experimentally conducted. The measurements have evidenced high nonreciprocity over flexural waves propagation which agree well with our simplified analytical predictions via TMM. An energy flux analysis based on the FEM numerical results has been conducted, in which we find out that the nonreciprocity in this device roots in the asymmetric frequency conversion.

The design concept of a nonreciprocal acoustic structure using air flow is introduce in Chapter 5, including the nonreciprocal mode converter and the nonreciprocal meta-lens. We first divide a cylindric waveguide into multiple coaxial ring channels. By adding different air flows in different channels, we can get different directional phase velocity in each waveguide channel, which results in different directional phase shift in each channel. The air flow is reachable implanting spinning rotors in the structures. When we have two waveguide channels, we can have inversed phase in one direction and nonchanged phase in another direction, which forms a nonreciprocal mode convertor. When we have multiple channels, we can encode desired directional phases in each channel and achieve multiple nonreciprocal metasurface functions, saying a nonreciprocal acoustic meta-lens. With the meta-lens, nonreciprocal wavefront manipulations from two opposite incidences are achieved. For example, in one direction, the plane wave radiation is focused, but when we perform time-reversal propagation, with a point source at the previous focusing position, we get a near-field acoustic beam instead of plane waves. Our finding exploits a simple way of using air flow to produce nonreciprocal systems using controlled rotating elements for phase modulation via variable air-flow velocities.

This doctoral project provides a promising perspective on the design of compact nonreciprocal metamaterials that can integrate acoustic and elastic waveguiding systems for smart wave control in phononic communication devices. Also, the multifunctional acoustic meta-lens which is capable to perform direction sound beam and focusing enable new possibilities of wave manipulation of metasurface, especially for biomedical ultrasound devices for instance.

My personal autobiography is attached at the end of this thesis, including all my publications.

Autobiography

WAN Sheng

August 17, 1996

🖂 sheng.wan@univ-lorraine.fr ☎ +33 (0)7 83 91 97 91

🏠 5 Avenue Jean Jaurès, 54500 Vandœuvre-lès-Nancy, France

Research contributions

Physical acoustics, Acoustic and elastic metamaterials, Acoustic metasurface for sound absorption, Seismic metamaterials, non-reciprocal acoustics and dynamics.

Current situation

PhD student, since Oct. 2019, at Jean Lamour Institute (CNRS), University of Lorraine, France.
Expected defense: December 2022. Subject: “Non-reciprocal acoustic metamaterials”.
Supervisor: Prof. Badreddine Assouar.

Education

- **Engineering degree, in Acoustics and Vibration**, Aug. 2018 – Sept. 2019, at **Université de Technologie de Compiègne, France.**
  Majors: Structural Vibration, Vibro-acoustic modelling, Acoustic measurements and experimental techniques, Signal processing.

- **Double degree**, Aug. 2016 – Jul. 2018, **Bachelor of Engineering** from **Xi'an Jiaotong University** and **Engineering degree** at **Université de Technologie de Compiègne (1st and 2nd years),**
  Majors: Vibration of continuous systems, CAE/CAD, Room acoustics design.

- **Bachelor of Engineering,** Aug. 2014 – Jun. 2016, at the **Department of Process Equipment and Control Engineering, Xi'an Jiaotong University.**

Skills

- FEM using COMSOL Multiphysics: Acoustics, Structural Mechanics, Fluid Flow (CFD), AC/DC
- Programing: MATLAB, C++, Python.
- CAE/CAD: ABAQUS, ANSYS FLUENT, PTC Creo, CATIA V5, AutoCAD.
- 3D printing and Deep learning.
- Experimental acoustics (airborne) and vibration characterizations.
- Languages: English (TOEIC: 785), French (fluent).

Internship experience

- **Acoustic engineer** (25 weeks), Mar. 2019 – Aug. 2019, at Faurecia Automobile Industry R&D, Mouzon, France.

Tasks: Characterization of automotive trim materials and database creation with the Faurecia acoustic team:

- Definition of the soundproofing cladding according to customer demand.
- Implementation and execution of various acoustic measurements.
- Correlation of sound absorption between numerical models and measurements.
- Design and creation of a database management system via PHP/MySQL.

- **Research assistant** (24 weeks), Feb. 2018 – Jul. 2018, at **Laboratoire Roberval (CNRS), Université de Technologie de Compiègne**, France.
  Task: Numerical simulation of the boat sinking in the Gironde estuary, via ANSYS FLUENT.

Publications in peer reviewed journals

1. **S. Wan**, L. Cao, Y. Zeng, T. Guo, M. Oudich, and B. Assouar, *"Low-frequency nonreciprocal flexural wave propagation via compact cascaded time-modulated resonators"*, Applied Physics Letters **120**, 231701 (2022), **Featured Article**, and **displayed on APL homepage.**
2. **S. Wan**, L. Cao, Y. Zhu, M. Oudich, and B. Assouar, *"Nonreciprocal sound propagation via cascaded time-modulated slab resonators"*, Physical Review Applied **16**, 064061 (2021)
3. L. Cao, Y. Zhu, **S. Wan**, Y. Zeng, and B. Assouar, *"On the design of non-Hermitian elastic metamaterial for broadband perfect absorbers"*, International Journal of Engineering Science **181**, 103768 (2022)
4. Y. Zeng, L. Cao, **S. Wan**, T. Guo, S. An, Y. Wang, Q. Du, B. Vincent, Y. Wang, and B. Assouar, *" Inertially amplified seismic metamaterial with an ultra-low-frequency bandgap"*, Applied Physics Letters **121**, 081701 (2022)
5. K. Donda, Y. Zhu, A. Merkel, **S. Wan**, and B. Assouar, *" Deep learning approach for designing acoustic absorbing metasurfaces with high degrees of freedom"*, Extreme Mechanics Letters **56**, 101879 (2022)
6. Y. Zeng, L. Cao, **S. Wan**, T. Guo, Y. Wang, Q. Du, B. Assouar, and, Y. Wang, *" Seismic metamaterials: Generating low-frequency bandgaps induced by inertial amplification"*, International Journal of Mechanical Sciences **221**, 107224, (2021)
7. K. Donda, Y. Zhu, A. Merkel, S. Fan, L. Cao, **S. Wan**, and B. Assouar, *" Ultrathin Acoustic Absorbing Metasurface Based on Deep Learning Approach"*, Smart Materials and Structures **30**, 085003, (2021)
8. L. Cao, Y. Zhu, **S. Wan**, Y, Zeng, Y, Li, and B. Assouar, *" Perfect absorption of flexural waves induced by bound state in the continuum"*, Extreme Mechanics Letters **47**, 101364, (2021)

Communications in international conferences

Oral communications

S. Wan, L. Cao, Y. Zhu, M. Oudich, and B. Assouar, *"Nonreciprocal flexural wave propagation via compact cascaded time-modulated resonators"*.
META 2022, the 12th International Conference on Metamaterials, Photonic Crystals and Plasmonics, 19th – 22nd July 2022, Torremolinos, Spain

Nonreciprocal Acoustic Metamaterials based on Time-Varying Media

Abstract

Nonreciprocal acoustic metamaterials are time-reversal-asymmetric devices in which the response field is different when the source and receiver are interchanged. Nonreciprocal acoustic metamaterials have significantly broadened the horizon of the whole acoustics field. As a novel category of nonreciprocal acoustic metamaterials, time-varying media are gaining research interest in recent years. In this doctoral project, we innovatively proposed several nonreciprocal devices based on time-varying media. First, a theoretical demonstration of acoustic nonreciprocity via cascaded time-modulated Fabry-Perot (FP) resonator system is introduced. Second, an experimental demonstrated of elastic flexural wave nonreciprocity via cascaded time-modulated spring-mass resonator (SMR) system is introduced, based on electromagnetic coupling. Last, we provide a new approach using air flow to bring in nonreciprocal multifunctional meta-lens. We split a sound waveguide into multiple channels, and directionally manipulate the phases of each channel to achieve unidirectional focusing and sound beam. This thesis provides new paradigms of nonreciprocal acoustic metamaterials, which would contribute to new possibilities of wave manipulation.

Keywords: Acoustic and elastic metamaterials, Nonreciprocity, Time-varying medium.

Métamatériaux Acoustiques Nonréciproques à Milieux Variables dans Le Temps

Résumé

Les métamatériaux acoustiques nonréciproques sont des dispositifs asymétriques à inversion temporelle dans lesquels le champ de réponse est différent lorsque la source et le récepteur sont interchangés. Les métamatériaux acoustiques nonréciproques ont considérablement élargi l'horizon de l'ensemble du domaine acoustique. En tant que nouvelle catégorie de métamatériaux acoustiques nonréciproques, les milieux variant dans le temps suscitent l'intérêt de la recherche ces dernières années. Dans ce projet doctoral, nous avons proposé de manière innovante plusieurs dispositifs nonréciproques basés sur des milieux variant dans le temps. Tout d'abord, une démonstration théorique de la nonréciprocité acoustique via un système de résonateur Fabry-Perot (FP) modulé dans le temps en cascade est introduite. Deuxièmement, une démonstration expérimentale de la non-réciprocité des ondes de flexion élastiques via un système de résonateur masse-ressort modulé dans le temps (SMR) en cascade est introduite, basée sur le couplage électromagnétique. Enfin, nous proposons une nouvelle approche utilisant le flux d'air pour apporter une méta-lentille multifonctionnelle nonréciproque. Nous divisons un guide d'ondes sonores en plusieurs canaux et manipulons directionnellement les phases de chaque canal pour obtenir une focalisation unidirectionnelle et un faisceau sonore. Cette thèse fournit de nouveaux paradigmes de métamatériaux acoustiques nonréciproques, qui contribueraient à de nouvelles possibilités de manipulation des ondes.

Mots clés : Métamatériaux acoustiques, Nonreciprocité, Milieu variant dans le temps.

Résumé

Métamatériaux acoustiques nonréciproques à milieux variables dans le temps

Le principe de réciprocité en acoustique et en élastodynamique établit une relation de symétrie entre l'excitation et la réponse dans les fluides et les solides. Une description complète de la réciprocité consiste à dire qu'après l'échange de positions entre la source et le point de mesure (ou le récepteur), la réponse fréquentielle entre deux points quelconques reste inchangée, malgré l'existence d'inhomogénéités et des pertes dans le milieu. Pendant plusieurs siècles, la réciprocité a toujours été considérée comme une loi fondamentale dans l'étude des phénomènes ondulatoires. Les progrès récents de la recherche théorique et l'avancée des techniques de fabrication nous ont incités à percevoir la réciprocité sous une nouvelle perspective : la réciprocité brisée pourrait ouvrir de nouvelles possibilités de manipulation des ondes. Guidés par une telle perception, les chercheurs ont conçu et fabriqué des dispositifs non-réciproques pratiques avec un contrôle sans précédent des ondes directionnelles. Par exemple, un dispositif qui laisse passer l'onde dans une direction avec un grand coefficient de transmission tout en bloquant les ondes rétrodiffusées, à savoir l'isolateur, a été conçu pour protéger les sources de la rétrodiffusion. En outre, les structures en volume qui sont des supports isolants à l'intérieur mais où les ondes peuvent se propager de manière unidirectionnelle aux frontières, ont pu être conçus en brisant la réciprocité. Ces structures sont appelées isolants topologiques.

Les milieux non linéaires, qui génèrent de manière irréversible des harmoniques, étaient autrefois un moyen populaire de rompre la réciprocité. Cependant, sachant que le mécanisme brisant la réciprocité à l'aide de matériaux non linéaires dépend en grande partie de l'intensité d’excitation, certaines limitations résident dans ces systèmes non linéaires non réciproques. En effet, une fois que l'état non linéaire dans le système est activé par une excitation, de petites ondes sont générées et se propagent dans le système dans toutes les directions, ce qui peut être indésirable pour certaines applications. Au cours de la dernière décennie, l'intérêt pour la non-réciprocité s'est porté sur les milieux variant dans le temps, y compris les milieux cinétiques et les milieux modulés spatio-temporellement (STM). Les milieux cinétiques sont des milieux à pièces mobiles ou à flux circulants, et les milieux STM ont leurs propriétés mécaniques variables à la fois dans l'espace et dans le temps. Les chercheurs ont observé que le décalage de fréquence trouvé dans l'effet Doppler est fondamentalement nonréciproque. Dans un scénario typique d'effet Doppler, une source communique avec un récepteur à travers une barrière mobile. Dans un tel scénario qui contredit la réciprocité, le décalage de fréquence Doppler change de signe lorsque la source et le récepteur sont échangés. Par conséquent, la réciprocité devrait échouer dans les guides d'ondes avec flux d'air ou les résonateurs annulaires avec flux de fluide en circulation, qui rompent toute la symétrie d'inversion temporelle. En examinant les milieux cinétiques, les chercheurs ont observé un diagramme de dispersion asymétrique dans des structures spatialement périodiques avec une vitesse de déplacement uniforme. C'est-à-dire que la relation entre la fréquence et le nombre d'onde n'est pas la même dans les directions de propagation le long ou contre le mouvement du support. Ainsi, le STM, qui partage le même comportement avec les structures spatialement périodiques en mouvement, brise la symétrie temporelle et conduire à la non-réciprocité. Cependant, étant donné que le STM est en fait stationnaire alors que les structures spatialement périodiques mobiles ne le sont pas, leurs différences s'enracinent dans les équations gouvernantes et apparaissent sur leurs diagrammes de dispersion. Le sujet principal de cette thèse est spécifiquement centré sur la non-réciprocité en acoustique en utilisant des milieux variant dans le temps.

Avec l'avancée rapide des capacités de calcul au cours des dernières années, des approches numériques ont été construites et largement adoptées dans l'analyse des systèmes nonréciproques avec des milieux variant dans le temps, à savoir la méthode des éléments finis (FEM) et la méthode du domaine temporel des différences finies (FDTD). Des approches semi-analytiques ont également été développées nécessitant un réglage rapide des paramètres et une exploitation physique, y compris la théorie des modes temporels couplés (TCMT), la méthode de la matrice de transfert (TMM) et la résolution du problème en valeurs propres quadratiques (QEP), couvrant divers scénarios d'application. Ces approches analytiques résolvent les quantités invariantes dans le temps, tandis qu'en présence de paramètres variant dans le temps dans un système nonréciproque, la décomposition de Fourier et la méthode de perturbation sont largement utilisées comme méthodes internes pour résoudre le problème avec des perturbations qui varient dans le temps.

L'objectif du présent projet doctoral est d'introduire une nouvelle famille de dispositifs compacts nonréciproques en acoustique et élastodynamique. Comme nous le montrerons tout au long des chapitres de ce manuscrit, nous avons pu concevoir et construire un système de résonateur Fabry-Perot (FP) couplés et modulés dans le temps en cascade, un système de bi-résonateurs mécaniques modulés dans le temps et une méta-lentille acoustique non-réciproque et multifonctionnelle utilisant le flux d'air, TMM et FEM sont utilisés pour fournir des démonstrations analytiques et numériques. Une réalisation expérimentale a été menée avec succès à l'aide de résonateurs actifs qui combinent aimants couplés à des bobines pour contrôler la raideur effective des résonateurs dans le temps.

Littérature sur les dispositifs acoustiques nonréciproques est présentée dans le Chapitre 1, état de l'art, y compris les milieux non linéaires, les milieux à base d’air en circulation, les milieux modulés spatio-temporellement et les milieux en mouvement. Plus précisément, les concepts et principes de réciprocité et de non-réciprocité sont introduits dans un premier temps, puis les différentes méthodes de réalisation de la non-réciprocité en acoustique et en élastodynamique sont expliquées avec des références représentatives.

Les approches numériques et analytiques utilisées pour résoudre le système acoustique nonréciproque à l'aide de milieux variant dans le temps sont discutées au Chapitre 2. Nous introduisons brièvement les méthodes des éléments finis et des différences finies dans le domaine temporel, puis expliquons dans des expressions détaillées la théorie des modes couplés temporels. (TCMT), la méthode de la matrice de transfert (TMM) et la résolution du problème quadratique aux valeurs propres (QEP) avec la décomposition de Fourier. Des scénarios simples d'application sont fournis pour ces approches analytiques.

Métamatériaux acoustiques nonréciproques basés sur une structure bi-résonateurs modulées dans le temps

Nous avons présenté deux systèmes bi-résonateurs aux propriétés modulées dans le temps dans les Chapitres 3 et 4, dans lesquels l'un est basé sur des résonateurs Fabry-Pérot (FP) couplées pour les ondes sonores, et l'autre est basé sur des résonateurs ressort-masse (SMR) couplés pour les ondes de flexion élastiques. Dans le Chapitre 3, nous avons démontré une transmission acoustique nonréciproque et une conversion de fréquence unidirectionnelle dans des résonateurs FP en cascade basés sur la modulation temporelle de leurs densités effectives, avec une différence de phase dans les modulations temporelles entre les deux FP. La méthode TMM basée sur la décomposition de Fourier a été développée pour une caractérisation efficace de la transmission des ondes dans le système, tandis que des simulations numériques basées sur la FEM ont été menées pour évaluer les résultats théoriques. Des optimisations sur les paramètres du système ont été effectuées pour obtenir la non-réciprocité à large bande et la conversion de fréquence. Un comportement de non-réciprocité acoustique a été observé avec une onde incidente monochromatique, avec près de 97,9% de transmission dans le sens positif alors que seulement 4,3% sont transmis dans le sens négatif. De plus, la conversion de fréquence unidirectionnelle a été exploitée. Plus de la moitié de l'énergie acoustique transmise a été convertie en un seul mode avec un rapport de densité statique plus élevé. La conception proposée du système acoustique nonréciproque affiche des fonctionnalités prometteuses, avec une configuration compacte simple pour réaliser la propagation unidirectionnelle des ondes et la conversion de fréquence. Bien que le système actuel soit purement théorique et loin de représenter un dispositif réaliste d'application, il est possible d'imaginer un système solide où l'on ne considère que les ondes longitudinales qui sont décrites avec la même équation de Helmholtz. Dans ce cas, notre approche pourrait également être menée en considérant la modulation temporelle de la raideur effective au lieu de la densité des matériaux à l'aide d'éléments piézoélectriques

Dans le Chapitre 4, nous avons introduit un système SMR en cascade mécanique modulé dans le temps à sous-longueur d'onde pour obtenir une transmission d'onde de flexion nonréciproque en basses fréquences. Les SMR ont été conçus avec un porte-à-faux vibrant avec des bobines et des aimants couplés magnétiquement. Nous avons d'abord établi une approche TMM semi-analytique impliquant la décomposition de Fourier pour effectuer le réglage des paramètres via un algorithme génétique (GA). La modulation temporelle de la rigidité effective de chaque résonateur est physiquement réalisée par un courant alternatif (AC) appliqué à la bobine qui se couple aux aimants fixes via le champ électromagnétique variable. La dimension de cet appareil est inférieure à 1/3 de longueur d'onde. Une réalisation physique d'un tel système basé sur des résonateurs bobine-aimant en porte-à-faux a été menée expérimentalement. Les mesures ont mis en évidence une non-réciprocité élevée sur la propagation des ondes de flexion qui concordent bien avec nos prédictions théoriques. Une analyse de flux d'énergie basée sur les résultats numériques FEM a été menée, dans laquelle nous découvrons que la non-réciprocité dans ce dispositif réside dans la conversion de fréquence asymétrique.

Métamatériaux acoustiques nonréciproques basés sur des milieux en mouvement

La conception d'une structure acoustique nonréciproque utilisant un flux d'air est présenté au Chapitre 5, y compris le convertisseur de mode nonréciproque et la méta-lentille nonréciproque. Nous divisons d'abord un guide d'ondes cylindrique en plusieurs canaux annulaires coaxiaux. En ajoutant différents flux d'air dans différents canaux, nous pouvons obtenir une vitesse de phase directionnelle différente dans chaque canal de guide d'ondes, ce qui entraîne un déphasage directionnel différent dans chaque canal. Le flux d'air est accessible en implantant des rotors tournants dans les structures. Lorsque nous avons deux canaux de guide d'ondes, nous pouvons avoir une phase inversée dans une direction et une phase non modifiée dans une autre direction, ce qui forme un convertisseur de mode nonréciproque. Lorsque nous avons plusieurs canaux, nous pouvons coder les phases directionnelles souhaitées dans chaque canal et réaliser plusieurs fonctions de métasurface nonréciproques, c'est-à-dire une méta-lentille acoustique nonréciproque. Avec la méta-lentille, des manipulations de front d'onde nonréciproques à partir de deux incidences opposées sont réalisées. Par exemple, dans une direction, le rayonnement d'onde plane est focalisé, mais lorsque nous effectuons une propagation par inversion du temps, avec une source ponctuelle à la position de focalisation, nous obtenons un faisceau acoustique en champ proche au lieu d'ondes planes. Notre découverte exploite une manière simple d'utiliser le flux d'air pour produire des systèmes nonréciproques utilisant des éléments rotatifs contrôlés pour la modulation de phase via des vitesses de flux d'air variables.

Ce projet doctoral offre une perspective prometteuse sur la conception de métamatériaux nonréciproques compacts pouvant intégrer des systèmes de guidage d'ondes acoustiques et élastiques pour le contrôle intelligent des ondes dans les dispositifs de communication phononique. De plus, la méta-lentille acoustique multifonctionnelle qui est capable d'effectuer un faisceau sonore directionnel et une focalisation offre de nouvelles possibilités de manipulation des ondes, en particulier pour les dispositifs à ultrasons biomédicaux par exemple.